Wrocław University of Technology
Centre of Advanced Materials and Nanotechnology

Materials Science-Poland

III International Conference on Advances in Processing, Testing and Application of Dielectric Materials APTADM 2007 Wrocław, 26–28 September 2007

Vol. 27 • No. 4/2 • 2009

Oficyna Wydawnicza Politechniki Wrocławskiej

Materials Science-Poland is an interdisciplinary journal devoted to experimental and theoretical research into the synthesis, structure, properties and applications of materials.

Among the materials of interest are:

- glasses and ceramics
- sol-gel materials
- photoactive materials (including materials for nonlinear optics)
- laser materials
- photonic crystals
- semiconductor micro- and nanostructures
- piezo-, pyro- and ferroelectric materials
- high-T_c superconductors
- magnetic materials
- molecular materials (including polymers) for use in electronics and photonics
- novel solid phases
- other novel and unconventional materials

The broad spectrum of the areas of interest reflects the interdisciplinary nature of materials research. Papers covering the modelling of materials, their synthesis and characterisation, physicochemical aspects of their fabrication, properties and applications are welcome. In addition to regular papers, the journal features issues containing conference papers, as well as special issues on key topics in materials science.

Materials Science-Poland is published under the auspices of the Centre of Advanced Materials and Nanotechnology of the Wrocław University of Technology, in collaboration with the Institute of Low Temperatures and Structural Research of the Polish Academy of Sciences and the Wrocław University of Economics.

All accepted manuscripts are placed on the Web page of the journal and are available at the address: http://MaterialsScience.pwr.wroc.pl

All published papers are placed on the Web page of the journal and are **freely accessible** at the address: http://MaterialsScience.pwr.wroc.pl

Materials Science-Poland is abstracted/indexed in: Chemical Abstracts, Materials Science Citation Index, Science Citation Index Expanded, Scopus.

The Journal is supported by the State Committee for Scientific Research

The texts of papers published in this issue of *Materials Science-Poland* appear with minor corrections only. The artwork has been reproduced as received.

Printed in Poland

Drukarnia Oficyny Wydawniczej Politechniki Wrocławskiej
Zam. nr 1103/2009.

Materials Science-Poland, *Vol. 27*, *No. 4/2*, *2009*

Electromagnetomechanical coupling response of plastoferrites

C. BROSSEAU*, W. NDONG

Laboratoire d Electronique et Systèmes de Télécommunications, Université de Bretagne Occidentale, CS 93837, 6 avenue Le Gorgeu, 29238 Brest Cedex 3, France

The impetus of this work was to investigate the electromagnetic and tensile properties of several commercially available plastoferrites (PFs) at ambient conditions. The approach involved selection of a set of PFs, and measuring their complex effective permittivity $\varepsilon = \varepsilon' - j\varepsilon''$ under uniaxial stress at microwave frequencies in the range 0.1–4.5 GHz at room temperature. The ε spectra have been analyzed for intensively strained PFs up to 3%. Comparing the experimental ε values against several dielectric relaxational behaviours, we find that the main physics cannot be understood with a single relaxation mechanism. More importantly we show that the ε measurements under stress can be explained in terms of a Gaussian molecular network model in the limit of low stress. The present results have important applications in magnetoactive smart composite materials, e.g. flexible circuit technology in the electronics industry (sensors, actuators and micromechanical systems), functionalized artificial skin and muscles for robotic applications.

Key words: *plastoferrite; effective permittivity; microwave spectroscopy*

1. Introduction

Plastoferrites (PFs) are thermosetting polymers filled with ferrite particles. Ferrites are widely used for components in high-frequency electronic devices, taking advantage of their high initial permeability, and high electrical resistivity. On the one hand, the ferrite (e.g., $Ba_3Co_2Fe_{24}O_{41}$) is a soft magnetic material with a planar anisotropy, having a relatively high resonant frequency and high permeability. On the other hand, the hexaferrite (e.g., $BaFe_{12}O_{19}$) has a high saturation magnetization and a strong uniaxial anisotropy leading to low permeability and very high resonant frequency. PF is a composite having constituents with highly dissimilar mechanical properties: polycrystalline ferrites have the density of about 5 g/cm^3 and a longitudinal modulus of the

*Corresponding author, e-mail: Christian.Brosseau@univ-brest.fr

order of 100 GPa, whereas a typical epoxy has a low density of about 1 g/cm^3 and a longitudinal modulus of a few GPa. These large differences can result in complex behaviour under tensile stress, particularly at higher loadings of ferrite. PFs are distinguished from other magnetic materials by their useful applications in a wide variety of fields such as microwave absorbers and flexible magnets. In addition, the mouldability of these composites into complex shapes is another advantage, and the properties of this class of filled polymers may be valuable to several related industries due to the versatile engineering and cost effectiveness.

On the experimental front, we note that there is no plethora of experimental and theoretical studies on the magnetization mechanisms and permeability behaviour in these materials. Along with technological interest in the magnetic properties of PF, there are also fundamental reasons for being excited about them. PFs are interesting partly because they are a class of composite materials that provide materials scientists an interesting opportunity for furthering our understanding of multifunctional materials. Moreover, the possibility in changing the grain size such as it matches with relevant fundamental length scales associated with exchange and dipolar coupling is one of the several issues that need to be addressed in regard to the aforementioned microwave applications. The electromagnetic wave transport properties of particulate composites are different in striking ways from those of the bulk counterparts. Tensile stress in these materials is complicated by the complex evolution of microstructure. Although there have been several attempts to develop the magneto-mechanical coupling characteristics of PFs, the progress of these methods has been impeded by the lack of precise experimental electromagnetic data, and general factors characterizing and explaining their polarization and magnetization are not well understood. One such factor is the elasticity network which strongly governs the physical/mechanical properties in the end use.

Rubber and particle-filled polymeric resins are large polymeric solid networks formed when polymers in the molten state are randomly cross-linked by permanent bonds and polymer chains are attached to the surface of particles. These materials are much more flexible than ordinary crystalline solids and, moreover, may remain in the linear viscoelastic regime even in response to deformations increasing their dimensions far beyond their original, unstrained, size. Such a behaviour is attributed to the elasticity network structure of these materials and to the fact that the elastic restoring forces are of entropic origin. Considerable scientific debate has taken place over the last decades regarding the structure and properties of the elasticity network [3, 4], and e.g. [5]. The simplest theory of rubber elasticity which captures these essential physical features is the Gaussian molecular network model (GMNM) [3, 4]. This model assumes that the configurations of the polymer chains are independent of each other, and neglects the excluded volume interactions between the monomers. With these simplifying assumptions, one can treat a polymer network as an ideal one. However, in filled polymers, the network strands are very short and do not necessarily resemble ideal Gaussian springs. Nevertheless, there is experimental evidence that the GMNM

of the elasticity network may be an appropriate model when a macroscopic large network spans the system [4, 6].

Dielectric and material properties of composite materials are routinely interpreted within the frame of EM theories. The importance of this issue manifests itself in a large area of research, the theory of composites, and a huge literature that cannot be cited here. The basic idea is to describe the system by a simple average permittivity (or magnetic permeability) and is based on a self-consistent procedure in which a grain of one of the constituents is assumed to have a convenient shape (usually taken as spherical or ellipsoidal) and to be embedded in a (homogeneous) EM whose properties are determined self-consistently [1, 2, 8–12]. This requires that the wavelength λ of the electromagnetic radiation probing the system has to be larger than a typical scale of length ξ that characterizes the inhomogeneities in the material. In the corresponding frequency region, the scattering effects from the heterogeneities are avoided. Actually, if one considers a mixed medium consisting of two constituents, each of which is characterized by a bulk (scalar) relative permittivity ε_i and relative permeability μ_i, there are at least three long wavelength (quasistatic) conditions:

$$\lambda >> 2\pi\frac{\xi}{c}\sqrt{\varepsilon_i\mu_i}, \quad i=1,\ 2 \quad \text{and} \quad \lambda >> 2\pi\frac{\xi}{c}\sqrt{\varepsilon\mu}$$

where c denotes the velocity of light in free space. For instance, the length scale of the dispersed phase in PFs is typically of the order of1 μm, whereas the smallest length scale, d, of the part manufactured from the polymer filled system is much larger, e.g. a few mm. If the above conditions were not satisfied, there would be the possibility that internal structure of the medium could diffract as well as refract radiation. In the microwave wavelength range, d and ξ are far smaller than λ. Continuing with our studies of tension-strained filled polymers [7], we recently discovered that the peak position (gyromagnetic resonance) of the spectrum of the imaginary part of the effective complex permeability of a PF at the microwave frequency is shifted towards higher frequencies in response to an external stress. Moreover, the paucity of experimental data on the electromagnetic of PFs, together with a desire to understand the physics of the frequency shift observed in this system has motivated our interest in additional experimental study.

The present work was undertaken to extend the understanding of the physical mechanisms that underlie the dielectric and magnetic behaviours of PFs. To do so, we choose models with the smallest number of parameters that allows one to study the phenomena of polarization and magnetization in PFs. Practical and predictive modelling of PFs to evaluate their magneto-mechanical coupling behaviour is a tough challenge and has still fallen behind applications and empirical description of their behaviour. There are ample motivations for developing a theory to understand, control and hence utilize the electromagnetomechanical coupling characteristics of soft composite materials. One potential interest is the development of flexible substrate. Flexible circuit technology attracts much attention in the electronics industry for portable applications

because the flexible substrate can be rolled, bent, and folded to fit a limited space where required. Two other potential applications deal with the design of functionalized artificial skin and muscles for robotics.

Guided by the results obtained in [7], the scope of the current study is to continue that work and to contribute in understanding the coupling between elasticity network of the polymer matrix and the effective dielectric and magnetic behaviors of PFs in the microwave range of frequencies. In this paper, we present a detailed investigation of the effective permittivity measured in the microwave range of frequencies. Three types of PFs were chosen to provide a reasonable comparative set of electromagnetic and magnetic parameters. We also present models describing the effective material properties and determine model parameters to fit the data. The difference in electromagnetic response between two states of PFs, i.e. magnetized vs. demagnetized, is also investigated. We hope that this characterization of PFs can provide valuable information for PF design.

2. Experimental

Epoxy-based plastoferrite composite formulations (designated samples PF1-PF3 in the present investigation) had different commercial origins and were used as received. These typical PFs (see Table 1) contain 30 vol. % of ferrite. These materials consist of micrometer size grains that are uniformly and randomly dispersed in an amorphous epoxy resin matrix.

Table 1. Specifications of the PF materials examined in the current study

Sample	Manufacturer	Type of a polymer[a]	Glass transition temperature[b] T_g [K]	Type of ferrite[a]	Fraction of ferrite [vol. %]	Average grain size diameter [μm]
PF1	Walker Braillon Magnetics	epoxy resin	271	$SrFe_{12}O_{19}$ hexaferrite	ca. 30	0.98
PF2	Euromag		279	Sr hexaferrite		0.94
PF3	Arelec		285	hexaferrite		0.97

[a]From the manufacturer product literature.

[b]Data obtained as a result of modelling from the current (SEM, XRD, and DMA) measurements.

The ferrite particles were imaged on a 100 keV Hitachi F-3200N scanning electron microscope. Cross-sectional micrographs on different regions of PF samples were taken to quantify the degree of polydispersity in size and shape. The microstructure

was digitized directly from micrographs to capture the grain morphology. As seen in the selected area SEM of Fig. 1, the ferrite grains are completely buried in an amorphous matrix.

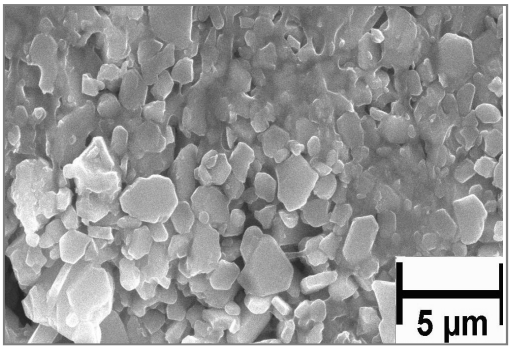

Fig. 1. Cross-sectional SEM images of a typical sample belonging to experimental series of PFs. The composite microstructure (PF3) is a three-dimensional assemblage of ferrite grains, bonded by an epoxy resin matrix

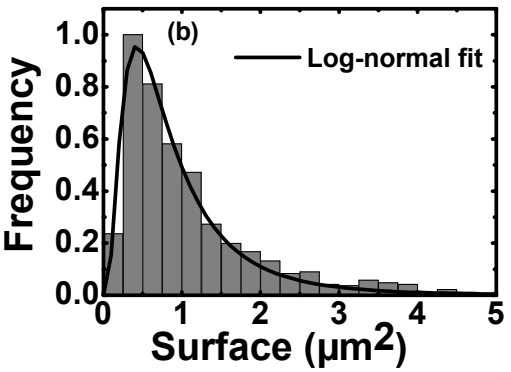

Fig. 2. Corresponding surface area distribution of ferrite grains (thousands in each characterization). The fitting results (solid line) have shown that a log-normal distribution of grain surfaces is a good approximation of the surface area profile. As a result, we obtained an average and variance of size (assuming that the grains have spherical shape) which are presented in Table 1

Most ferrite grains are approximately spherical. Each of the PFs studied was carefully characterized for ferrite grain projected surface and distribution. As illustrated by the histogram in Fig. 2, there is agreement between the (normalized) experimental surface area data and the calculated curve based on a log-normal grain surface distribution:

$$f(A)=\frac{1}{\sqrt{2\pi}\sigma A}\exp\left(-\frac{1}{2\sigma^2}\left(\log A-\log A_0\right)^2\right)$$

This distribution satisfies the properties: $\langle \log A\rangle = \log A_0$, and

$$\left\langle \left(\log A-\log A_0\right)^2\right\rangle = \sigma^2$$

Assuming a spherical grain shape, it appears that the measured ferrite average grain size is about 1 μm for the PF samples chosen for the present study (Table 1). Some intergranular pores are present in all samples.

The electromagnetic characterization of PFs was performed by *in situ*, real-time measurement of the transmission/reflection coefficients of an asymmetric microstrip transmission line containing the sample during uniaxial tensile stress. Since the details of this method have been described elsewhere [7], we shall not repeat that derivation here, but simply give a brief description of the experiment. The experimental setup used for producing tensile loading was described in [7]. The rectangular-shaped samples (approximately 50×3×1.8 mm^3) were mounted with clamped ends. The stress sequence employed in this work consisted in a series of step stress (0.5%) changes. The current method was employed to extract the effective complex (relative) permittivity $\varepsilon = \varepsilon' - j\varepsilon''$ and (relative) permeability $\mu = \mu' - j\mu''$ of a composite sample from microwave measurement, where $j = \sqrt{-1}$. The measurement of the scattering parameters (*S* parameters) is achieved using a Agilent H8753ES network analyzer with SOLT calibration. The test device is used as Thru in the transmission connection. Control of data acquisition and data storage is accomplished with Labview 6.1 (National Instruments) graphical programming software operating in a Windows 2000 environment. The method enables us to calculate simultaneously ε and μ of the material over a frequency range of 0.1 MHz – 4.5 GHz from the measurement of the S_{21} and S_{11}. It was not possible to explore the ε and μ spectra at higher frequency because of the dimensional resonance mode arising at ≅ 6.5 GHz. An error analysis indicates modest uncertainties in ε' (<5%), ε'' (<1%), μ' (< 3%), and μ'' (< 1%) for the data. One further feature of the measurement system is worth commenting on. To obtain accurate measurements of ε and μ, it is particularly important to account for the residual air-gap between the sample and the line walls. On the one hand, the air space increases as the extension is increased. On the other hand, the gap is determined by the roughness of the surfaces of the measured samples. A static magnetic field can be applied perpendicular to the rectangular-shaped sample by an electromagnet. A Hall sensor is used to measure the field near the characterized sample.

To understand the complex permittivity of these systems, the relative importance of polarization (ε'') and conduction ($\sigma_{dc}/(\varepsilon_0\omega)$) losses needs to be addressed. For this purpose, dc electrical measurements were carried out in capacitive configuration. All dc current–voltage *I–V* characteristics and contacts were Ohmic in the voltage range studied. Details of the circuit equipment and conditions for measuring the dc electrical conductivity σ_{dc} are given elsewhere [14]. Since the parameter $(\sigma_{dc}/(\varepsilon''\varepsilon_0\omega)) << 1$ in our samples under investigation $(\sigma_{dc}/(\varepsilon_0\omega) \approx 10^{-3}$ at 1 GHz, to be compared with the typical order of magnitude of ε'' of 10^{-2}), then we do not need to take into account any contribution of the static conductivity in the modelling of the imaginary part of the effective permittivity. This is consistent with recent work on the microwave absorbing properties of ferrite nanopowder dispersed in a polymer matrix [14]. The dc conductivity of the material is also important as it determines the extent of losses due to eddy currents. The skin depth being large compared to the sample size, the influence of eddy currents on the magnetic field is entirely negligible.

3. Results and discussion

The first set of results concerns the frequency dependence of the complex effective permittivity of a typical sample (PF1) in the demagnetized state. In Figure 3, we present two examples of ε' and ε'' to allow comparison at two different extension ratios ($\lambda = 1$ and $\lambda = 1.023$).

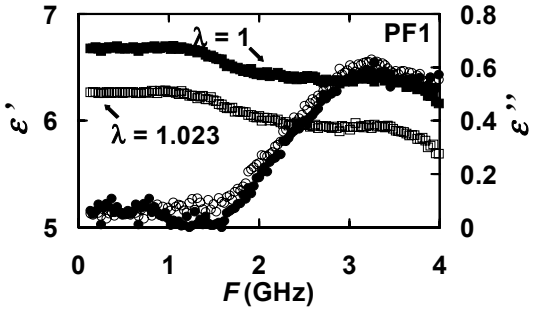

Fig. 3. Spectral dependence of the real and imaginary parts of the effective permittivity of PF1 for two values of the extension ratio λ; room temperature

Figure 3 illustrates the number of reproducible features generally found in all sets of results in this study. The observed dielectric response is complex and cannot be identified with a single relaxation mechanism. In the frequency range 0.1–4.5 GHz investigated, a single resonant peak at ≈ 3.5 GHz was observed which does not change with extension over the considered range of strain. It is attributed to Maxwell–Wagner (MW) interfacial polarization. Similar observations have been made for $Ni_{1-x}Zn_xFe_2O_4$ ferrite particles embedded in a butyl rubber matrix [15]. A decrease of ε' is observed as λ is increased, while ε'' is only slightly modified with increasing λ. The extension dependence of the change of sample dimensions relative to their respective initial value was characterized (not shown). The most striking feature of these experimental data is that the lateral dimensions cannot be adequately described as $\propto 1/\lambda^{1/2}$, that models the contraction of a volume invariant sample. This is attributed to much smaller Poisson s ratio $\nu \approx 0.3$ of the plastoferrite sample.

In keeping with our stated goal of developing an analysis for interpreting electromagnetic properties of PFs, the interpretation of the experimental data can now be tested with different relaxation models. Figure 4 shows representative plots of the imaginary (ε'') versus real (ε') part of the complex effective permittivity (Cole–Cole plot) at different frequencies. For a pure Debye-type response (see Appendix), the effect of grain and grain boundary can be modelled with parallel combinations of respective capacitance and resistance connected in series. Each resistance and capacitance combination is expected to exhibit a separate semicircle with different mean relaxation times. As shown in Fig. 4, the ε'' (ε') variations seem to deviate considerably from a perfect semicircle and appear to be stretched. This indicates a distribution in time constant characteristic of a material that exhibits a broad size distribution consistent with the SEM observations. We note that care is needed when comparing these

experimental data with models that are customarily used to determine the relaxational behaviour of dielectric materials.

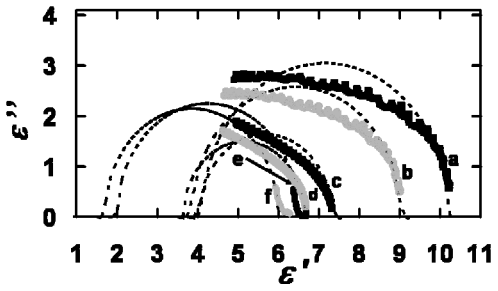

Fig. 4. Experimental and calculated effective (relative) permittivities of PFs for two values of λ: real part of the permittivity for PF1 (a), PF2 (c), and PF3 (e), imaginary part of the permittivity for PF1 (b), PF2 (d), PF3 (f). The dashed lines denote the results from the Debye model (Eq. (A1)); room temperature

It would be tempting to assign an intrinsic permittivity behaviour for each constituent of the PF based upon, e.g. the HN expression, take into account of the dilution of ferrite particles by the EM theory, e.g. Bruggeman equation, and then fitting them to the data by least-squares schemes. However, such an interpretation is arbitrary if there is no clear prescription for the proper choice of the intrinsic permittivity of various constituents of the PFs. In addition, there is little doubt that the fit parameters would be greatly affected by the manner of fitting the data considering the polydispersity of the ferrite particles and the relatively small range of frequencies explored.

The starting point of an investigation into the dielectric properties of any tension-strained material is to determine its equation of state in terms of stress, strain, and effective permittivity (or conductivity). While some work has been performed on the quantitative dc conductivity response of polymers under tensile stress [4, 7], the corresponding ac microwave response has not yet received the amount of attention it deserves. Very recently, Brosseau and Talbot [7] suggested that the GMNM functional form ($\lambda - 1/\lambda^2$) may be applicable to a variety of soft materials for calculating the tensile stress dependence of ε and μ providing that the elasticity network in the material occurs in a manner that is topologically similar to the elasticity network of a conventional rubber. We here assess the wider applicability of the model by comparing predictions (solid and dashed lines in Fig. 5.) to experimental measurements of the electromagnetic parameters of a set of PFs.

In Figure 5, we present the plots of

$$\Delta\varepsilon' = \frac{\varepsilon'(\lambda=1) - \varepsilon'(\lambda>1)}{\varepsilon'(\lambda=1)} \quad \text{and} \quad \Delta\varepsilon'' = \frac{\varepsilon''(\lambda=1) - \varepsilon''(\lambda>1)}{\varepsilon''(\lambda=1)}$$

for PF samples at 500 MHz in function of the extension ratio λ. Here it can be observed that the experimental trend is in excellent agreement with the GMNM functional form constrained to pass through the origin.

It is worth considering in some detail the processes leading to the emergence of an interpretation of the experimental data such as those represented in Figs. 3 and 6. We

are dealing with a complicated problem, in which the dominant feature is its stochastic and interactive nature. This means that no simple model involving non-interacting entities pursuing deterministic trajectories, such as orientations of dipoles, can adequately represent the true situation. The complexity may be structural in origin (ferrite grain boundaries, defects), or it may be rooted in complex electromagnetic and mechanical interactions (many different exchange couplings, perhaps competing).

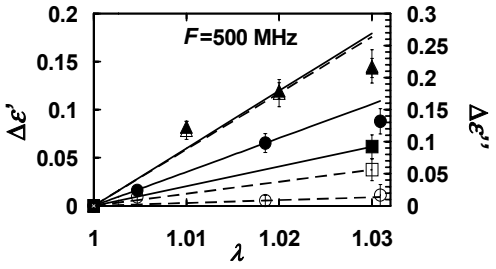

Fig. 5. Dependences of $\Delta\varepsilon'$ and $\Delta\varepsilon''$ for PF samples on the extension ratio λ; $F = 500$ MHz at room temperature; circles squares and triangles correspond to PF1, PF2 and PF3, respectively. Open (filled) symbols correspond to B (A). The best-fit solid curves (constrained to pass through the origin) to the functional form $(\lambda - 1/\lambda^2)$ are also shown

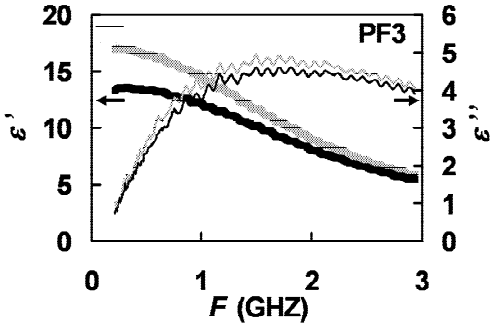

Fig. 6. Real and imaginary parts of the effective permittivities for a magnetized and demagnetized PF3 sample at room temperature. The thick (thin) solid lines represent the real (imaginary) parts of the permittivity. Magnetized (demagnetized) sample corresponds to the black (grey) curve

The above discussion has been made on a phenomenological basis irrespective of any particular mechanisms of relaxation. The generally accepted mechanisms for these features are discussed now. Two possible types of polarizing species, i.e. dipoles and MW, may contribute to the microwave behaviour. At frequencies high enough, the polarization responses of the two corresponding types can be empirically described by the same fractional power law. Thus, it is quite difficult to discriminate between the two contributions. We also observe that the permittivity spectra do not provide a full description of the dielectric relaxation spectra since we considered limited sets of data in the GHz range of frequency.

4. Conclusions

The work reported in this paper represents the most comprehensive experimental study to date of the frequency dependence of the electromagnetic parameters of tension-strained PFs. The general results collected and the trends observed have been discussed. Specific findings of the developments presented here are listed below.

We have studied a set of three commercially available PF samples with different magnetic characteristics as a result of different materials and different processing parameters. As described above, the tensile strain generated in the PFs causes significant changes of the electromagnetic parameters in the microwave range of frequencies. This is a direct manifestation of the elasticity network structure of the PFs. Another perspective on the electromagnetomechanical coupling comes from considering the GMNM model to account for the interconnected network of chains and ferrite grains which spans the entire structure. A complete description of this coupling would require involving a broad range of time and length scales, which is beyond the scope of this study. Nevertheless, as illustrated in Fig. 4, the quantitative agreement between modelling and experiment at low stress levels shows the GMNM model as viable physics to be included in studies of electromagnetomechanical coupling in PFs. This peculiar property of the response of PFs to uniaxial stress may have important implications in the design of magnetoactive smart composite materials with optimized electromagnetic properties.

The series of experiments reported here suggests that, for a given PF, deviations of ε from the archetypal dipolar Debye relaxation model occur in the range of frequencies explored. These features are tentatively associated with MW interfacial polarization. We emphasize again that accounting for the effective dielectric behaviour of these composite materials, without characterizing the intrinsic electromagnetic parameters of the individual constituents and the internal morphology, remains speculative. However, an interesting consequence of the data presented above is that the phenomenological scaling ansatz (GMNM) is also consistent with the experimentally observed permittivity change under elongation, indicating that the variations of permittivity and permeability are clearly mutually dependent. Designing magnetic materials, where parameters such as the type of ferrites or the composition can be finely tuned, allow a high degree of customization of magnetically soft materials.

References

[1] BROSSEAU C., J. Phys. D, 39 (2006), 1277.
[2] BROSSEAU C.AND BEROUAL A., Prog. Mater. Sci. 48 (2003), 373.
[3] TRELOAR L.R.G., *The Physics of Rubber Elasticity*, Oxford University Press, Oxford, 1975.
[4] MCCRUM N.G., READ B.E.,, WILLIAMS G., *Anelastic and Dielectric Effects in Polymer Solids*, Wiley, New York, 1967.
[5] *Physical Properties of Polymeric Gels*, J.P. Cohen-Addad (Ed.), Wiley, Chichester 1996; COHEN-ADDAD J.P., Prog. NMR Spectrosc. 25 (1993), 1.
[6] DE GENNES P.G., *Scaling Concepts in Polymer Physics*, Cornell University Press, Ithaca, NY, 1979.
[7] BROSSEAU C., TALBOT P., Meas. Sci. Technol. 16 (2005), 1823.
[8] *Dielectric Properties of Heterogeneous Materials*, Progress in Electromagnetics Research, A. Priou, ed., Elsevier, New York 1992.
[9] SIHVOLA A.H., *Electromagnetic Mixing Formulas and Applications*, IEE Publishing, London 1999.
[10] TORQUATO S., *Random Heterogeneous Materials: Microstructure and Macroscopic Properties*, Springer, New York, 2002.

[11] BERGMAN D.J., STROUD D., Solid State Phys., 46 (1992), 147.
[12] SAHIMI M., *Heterogeneous Materials I : Linear Transport and Optical Properties*, Springer, New York, 2003.
[13] OBRADORS X., SOLANS X., COLLOMB A., SAMARAS D., RODRIGUEZ J., PRENET M.,, FRONT-ALTABA M., J. Solid State Chem., 72 (1988), 218.
[14] BEROUAL A., BROSSEAU C., IEEE Trans. Dielectrics EI, 8 (2001), 921.
[15] KOLEV S., YANEV A.,, NEDKOV I., Phys. Stat. Sol. C (2006), 3, 1308.
[16] FRÖHLICH H., *Theory of Dielectrics: Dielectric Constant and Dielectric Loss*, Clarendon Press, Oxford, 1986.
[17] DEBYE P., *Polar Molecules*, Dover, 1945; see also COLE R.H., COLE K.S., J. Chem. Phys. 9 (1941), 341.
[18] HAVRILIAK S., NEGAMI S., Polymer 8, 101, 1967; see also Havriliak S.J., HAVRILIAK S. Jr, *Dielectric and Mechanical Relaxation in Materials*, Hanser, New York, 1997.

Appendix. Relaxational modelling of homogeneous dielectric materials

Extensive investigations have been focused on this issue and we have referenced only the papers that are the most relevant to the work carried out here. Several theoretical approaches have been developed to describe the relaxation modelling in dielectrics [16].

The simplest model has been eventually described by Debye [17]. In the Debye formulation of dielectric relaxation, the complex permittivity is written as

$$\varepsilon = \varepsilon' - i\varepsilon'' = \varepsilon_\infty + (\varepsilon_s - \varepsilon_\infty)\frac{1}{1+i\omega\tau} \tag{A1}$$

where ε_s and ε_∞ denote the static ($\omega = 0$) permittivity and the limiting permittivity at high frequencies ($\omega\tau \to \infty$) which depends on atomic and electronic polarizability, respectively. For the case of a single characteristic relaxation time τ, the points (ε', ε'') lie on a semicircle with the centre on the ε' axis and intersecting this axis at $\varepsilon' = \varepsilon_s$ and $\varepsilon' = \varepsilon_\infty$.

This approach is intuitively attractive since the one exponential modelling in the time domain, i.e. Eq. (A1) in the frequency domain gives an adequate description of the behaviour of the orientation polarization for many condensed matter systems. Despite the intuitively attractive features of this formulation, there are practical problems in implementing Eq. (A1) due to difficulties inherent to the complexity of the material, e.g. distribution of relaxation times.

For a continuous distribution of relaxation times, one can substitute the $1/(1 + i\omega\tau)$ into Eq. (A1) by $\int_0^\infty \frac{g(\tau)\,d\tau}{1+i\omega\tau}$, where it is assumed that the weighting function is normalized such that $\int_0^\infty g(\tau)\,\mathrm{d}\tau = 1$. An alternative method, described by the Havriliak–Negami (HN) expression, has been put forward [18]

$$\varepsilon = \varepsilon_\infty + (\varepsilon_s - \varepsilon_\infty)\frac{1}{\left(1+(i\omega\tau)^\alpha\right)^\beta} \tag{A2}$$

where it is assumed that the non-negative quantities α and β gauge the symmetric and asymmetric broadening of the dielectric loss spectrum, respectively. This expression reduces also to Eq. (A1) for $\alpha = \beta = 1$.

Received 7 May 2007
Revised 14 August 2007

Materials Science-Poland, *Vol. 27*, *No. 4/2*, *2009*

Charge relaxation on surfaces of polymeric insulating materials for outdoor applications

H. SJÖSTEDT*, R. MONTAÑO, Y. SERDYUK, S. M. GUBANSKI

High Voltage Valley, Fredsgatan 27, Box 832, 771 28 Ludvika, Sweden

The studies have been presented on spatial and temporal distributions of surface charge on samples of ethylene propylene diene monomer (EPDM) and silicon rubber (SIR). The charge was deposited from a positive impulse corona source located at 1 mm above the polymeric surfaces. During the experiments, the number of pulses and their voltage level were varied. It was observed that the spread of the charge over the surface of the samples as well as its magnitude were both increasing with increasing number of impulses applied. EPDM accumulated charge easier and had a longer relaxation time than SIR. A common feature frequently observed in both cases was that the resulting charge distributions had a saddle-like pattern. Performed computer simulations showed that this feature can be attributed to peculiarities of the corona charging in the considered system, which took place in a form of a burst corona, and the dynamics of the deposited charges could be related to burst corona pulses.

Key words: *outdoor insulation; composite insulators; surface charge; relaxation time*

1. Introduction

The use of polymeric materials in insulation systems of high voltage apparatuses increases steadily during the last decades [1]. It is believed that polymeric insulation will be dominant in ultra high voltage transmission systems, which are being developed presently for voltage levels up to 1000 kV ac and 800 kV dc for overhead lines and up to 500 kV ac and 300 kV dc for underground/submarine cables. Apparatuses and components, normally operating under system voltages, should also remain functional when exposed to overvoltages appearing in the network due to external causes, e.g., nearby or direct lightning strikes, or internal ones like switching operations, polarity reversal in HV dc systems, etc. Under these circumstances, the reliability and performance of the entire system and its components is influenced by the quality and proper design of HV electrical insulation.

*Corresponding author, e-mail: hans.sjostedt@highvoltagevalley.org

Two materials that have been extensively tested during the last decades and have been proved to be the most suitable for applications in outdoor insulation systems are ethylene propylene diene monomer (EPDM) and silicon rubber (SIR). At ultra high voltage levels insulation materials behave differently, giving rise to new phenomena that needs to be better understood if the design and construction of high voltage equipment is to be successful. This especially refers to accumulation and relaxation of electric charges at insulator surfaces and interfaces, which in turn may trigger unexpected flashovers during testing and operation [2].

In this paper, we focus on the analysis of experimental data on the dynamics of surface charges deposited on material samples (EPDM and SIR). The samples were exposed to positive corona produced from a needle electrode by applying lightning impulse voltages and resulting spatial distribution of the surface charges and their variations with time were detected. The charging process was analysed also by means of computer simulations of a positive corona in the electrode arrangement used in the experiments. The results indicated that the measured surface charge patterns can be attributed to burst corona mode in the considered system.

2. Experimental

Experimental set-up. The material samples examined were plane quadratic plates (147×147 mm^2) and 2 mm thick. The both types contained alumina trihydrate (ATH) as a filler. The samples were placed on a grounded copper sheet. Over the midpoint of the samples, a high voltage corona electrode was placed. It was a steel needle with a tip radius of 50 μm fixed vertically on another copper sheet of the same size as the grounded one. The high voltage set (needle and copper plate) was placed at a distance of 32 mm from the grounded plate and the resulting distance between the needle tip and the polymeric sample surface was 1 mm as shown in Fig. 1. Before voltage application, the surface of a sample was cleaned with a cloth soaked with isopropyl alcohol and then the sample was left to rest during approximately one hour.

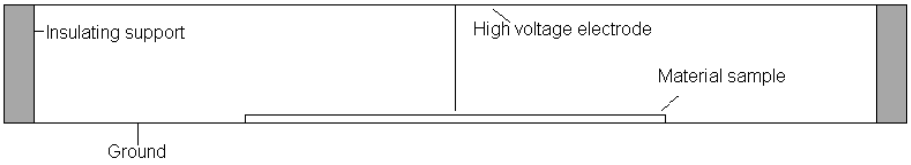

Fig. 1. Schematic view of the experimental set-up

A number (1, 3 or 5) of standard positive lightning impulses (1.2/50 μs) were applied to the corona electrode using an impulse tester HAEFELY PU12. The amplitude of the impulses was 6 or 11 kV. The time interval between the impulses was approximately 20 s. Thereafter, variations of the surface potential were measured with a vi-

brating capacitive probe (9 mm in diameter) connected to an electrostatic voltmeter, Trek 347, along the midlines of both perpendicular directions of the surface, as illustrated in Fig. 2. The probe was mounted onto a step motor driven robot that moved the probe along the lines. The distance between the aperture of the probe and of the scanned sample surface was 2 mm. The time lapsed from the last applied impulse until the measurements were commenced was equal to ca. 60 s.

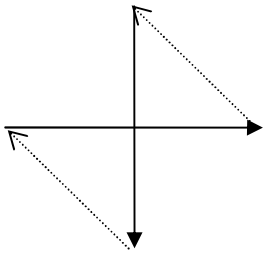

Fig. 2. Scanning procedure, the thick lines with arrows show how the measurements were performed

The measurements were performed at constant ambient conditions in open air atmosphere at 18–20 °C and the relative humidity 21–24%.

Characterisation of the material. Both the volume and surface resistivities were measured for the investigated material samples using a three-electrode system. The voltage of 400 V was applied for 60 min during these measurements. The results are presented in Table 1.

Table 1. Results of resistivity measurements

Material	Volume resistivity [Ω·cm]	Surface resistivity [Ω /sq]
EPDM	$2.50 \cdot 10^{16}$	$5.0 \cdot 10^{15}$
SIR	$2.12 \cdot 10^{15}$	$6.9 \cdot 10^{14}$

One can see that EPDM samples exhibited much higher bulk and surface resistivities than SIR samples and, hence, one can expect different conditions for charge leakage through the volume of the materials as well as for its relaxation on the sample surfaces leading to different characteristic relaxation times for the studied materials.

3. Experimental results

3.1. Surface potential distribution

The surface potential distributions recorded on EPDM and SIR samples for the two different charging voltages are shown in Fig. 3. It is important to mention that the

distributions in both the scanned directions (Fig. 2) were similar to each other and, thus, they are shown below for one direction only. One can also notice from Fig. 3 that the measuring system was saturated at the initial stages after charging with the highest voltages and several impulses in series, meaning that the charge densities under these conditions were actually higher than the ones indicated on the graphs.

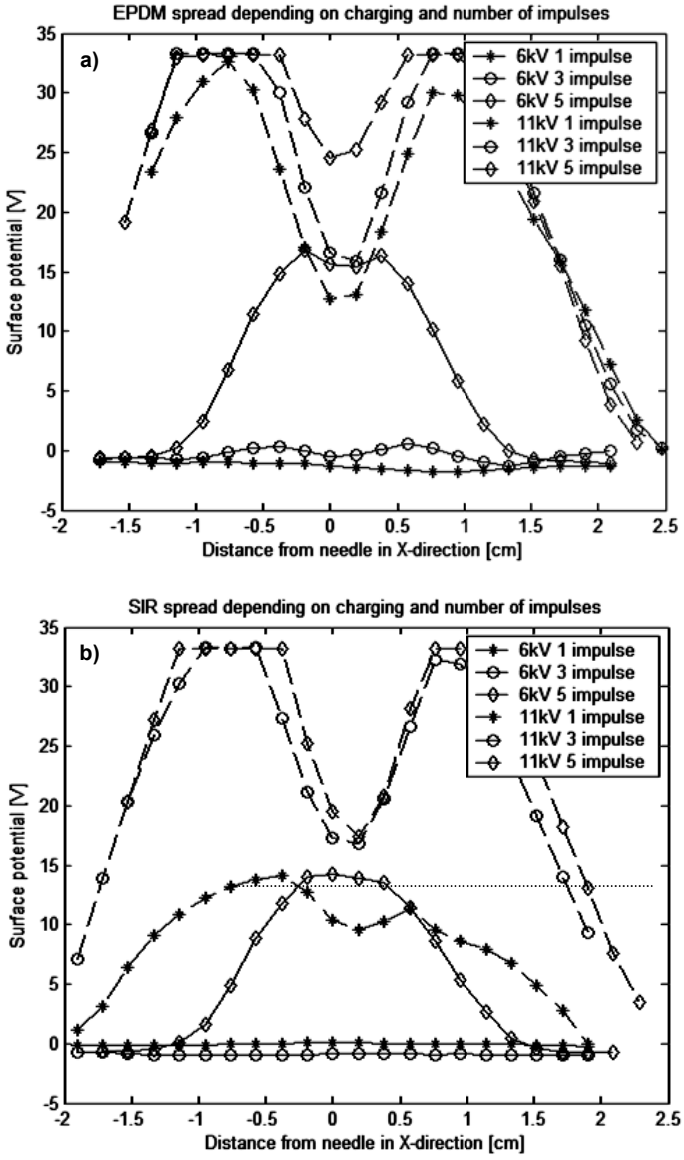

Fig. 3. Surface potential distributions along the midline of EPDM (a) and SIR (b) samples 60 s after charging with various numbers (1, 3 or 5) of corona pulses at 6 and 11 kV

The data in Fig. 3 shows that the surfaces of the samples were weakly charged when one and three impulses of low amplitude (6 kV) were applied and the sign of the measured surface potential was opposite as compared with the polarity of the applied impulses. The potential of the same sign (positive) was recorded on the surfaces when five impulses in series with the amplitude of 6 kV were applied as well as for any number of impulses with the amplitude of 11 kV. In the latter case, one can observe that the magnitudes of the measured surface potentials are higher for EPDM samples than for SIR, i.e. the charge accumulation process is more effective. This correlates with the measured volume resistivities of the materials: the higher resistivity of EPDM prevents leakage of deposited charges through the bulk of the material leading to their higher concentrations on the surface.

It can be also observed on Fig. 3 that the number of corona pulses as well as the magnitude of the charging voltage affected the expansion of the deposited charges over the surfaces of the samples. The distributions became broader at higher charging voltages and the difference between the spreads is about twice as large for the higher voltage. The same refers to the increasing number of corona pulses. This is in agreement with the observations reported in [3].

One may notice from Fig. 3 that for the same number of corona impulses and their magnitude, the spread of charges over the sample surfaces is stronger for SIR samples. This correlates with the fact that the measured magnitude of the surface resistivity of SIR is lower than that of EPDM (Table 1) and, hence, charge leakage along the surface of SIR samples is more intensive. It is also notable that the width of the charged regions is unexpectedly large (if compared with 1 mm gap between the corona needle and the sample surface). The explanation could be that the main expansion of deposited charges takes place very quickly during charging process, when the size of the charged region is very limited and the surface charge densities are extremely high. The process becomes slower with time due to reduction of the charge densities, and the results shown in Fig. 3 indicate the final stages of the process, when steady-state conditions are practically reached. Such a situation has been considered in [4], where fast expansion of charges over gas-solid interface (ca. 10 μs) was observed at streamer arrival to the insulator surface.

3.2. Surface potential decay

The time dependences of the surface potential measured at the point on the surface directly below the corona needle are presented in Fig. 4 separately for EPDM and SIR. The decay rates are dependent on the number of applied impulses (i.e., on the amount of the deposited charge). An exception is seen in Fig. 4b, where data for 3 and 5 impulses are practically on the top of each other. In general, the decay of the surface potential is faster for SIR material that can be attributed to its lower volume and surface resistivities leading to stronger charge leakage.

Table 2. Time constants in seconds for charging at 11 kV with 1, 3 and 5 corona pulses

Material	EPDM	SIR
1 impulse	8928	662
3 impulses	13 500	2440
5 impulses	6142	4064

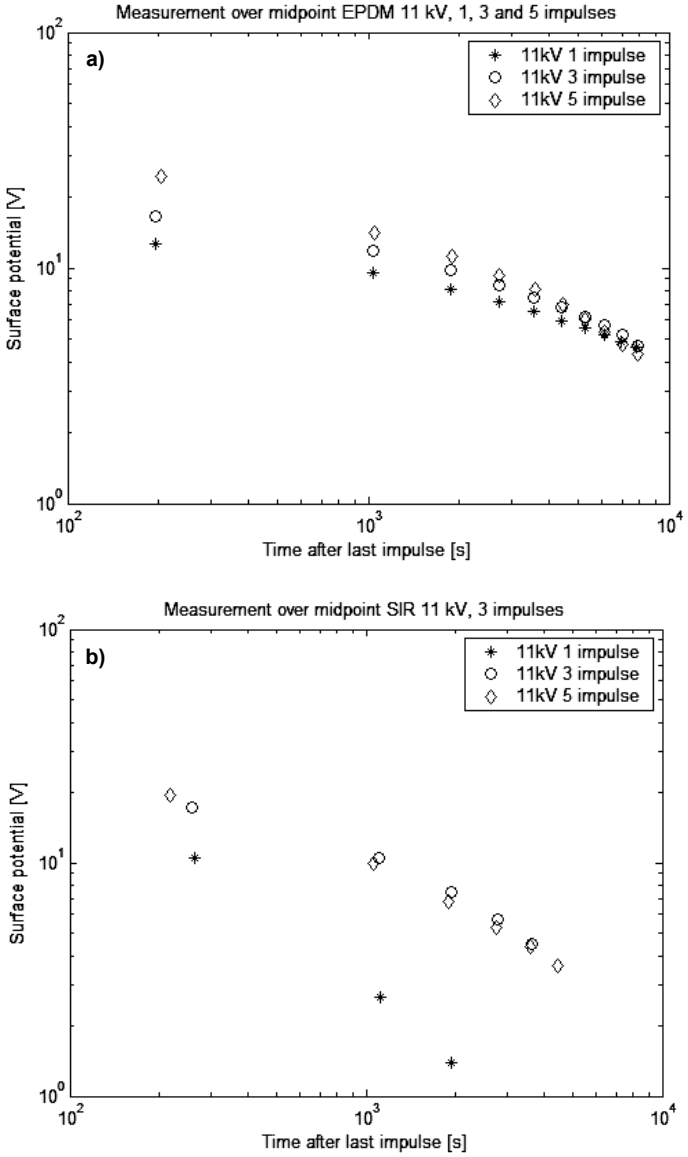

Fig. 4. Time variations of the surface potential on EPDM (a) and SIR (b) samples for the different number of impulses

Fitting the data in Fig. 4 with exponential functions provided decay time constants shown in Table 2. At the same time, estimations of the time constants made based on the measured volume resistivities of the materials and their permittivities (the dielectric constants were found to be equal to 4) yielded values of ca.8850 s and ca. 750 s for EPDM and SIR, respectively, which are in agreement with the data in Table 2 for single impulse charging. An analysis of the data in the table leads to important observation that the ratio between the time constants for EPDM and SIR decreases with increasing number of applied impulses, indicating that material properties become less important for the potential decay at higher amount of deposited charges.

4. Discussion

The presented experimental results allow arguing that the dominating charge decay mechanism for the studied materials is mostly through the bulk of the samples, similarly as observed in [5]. An additional source of charge neutralization may be recombination with ionic species in the air. The fact that the spread of the surface charge distributions (Fig. 3) did not change with time may indicate that the driving force for the spreading originates from own electric field of the deposited charge. If this field appears too low, the width of the distribution remains fixed, as is shown in Fig. 5 for the low charging voltage. The own charge field, on the other hand, is most effective for the spreading during the short periods of corona pulse action, since the initial charge distribution is point-like and therefore has a strong own field.

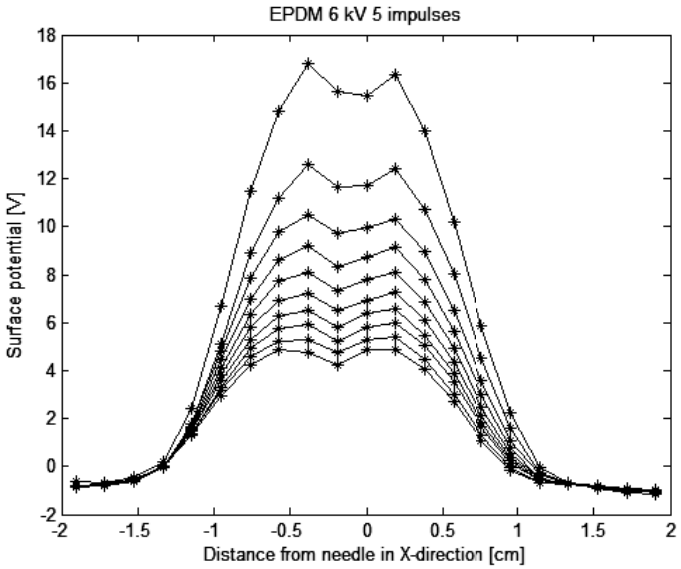

Fig. 5. Spatial- and temporal variations of the surface potential on EPDM sample for 5 corona pulses at 6 kV; the time interval between the decaying potential curves is 15 min

An interesting feature observed was that the surface potential distributions had a saddle-like shape in the region close to the needle electrode. Vaious explanations may exist for this feature. A similar behaviour of the surface charge as reported here was observed by Baum et al. [6, 7] on thin polyethylene films when charging with negative corona pulses. The authors explained the faster decay in the central region in terms of photoinjection from the surface states into the material bulk which are induced by the corona radiation. At the same time the effects of positive corona pulses were also studied, but they did not yield the saddle-like shape of the surface charge distribution [7].

Numerical simulations showed that the positive impulse corona in the arrangement of Fig. 1 appeared in the form of burst pulses taking place even during one applied voltage impulse. Hence, several waves of positive charges were sent out from the needle. This led to accumulating each time more surface charge in the region close to the needle axis and producing a strong field component along the surface, which thereafter pushed the charge further away. The simulation resulted in the saddle-like surface potential distributions, similar to ones observed in the experiments. However, the magnitudes of the computed potentials were higher than those obtained experimentally and resulted from assuming infinite volume resistivity of the solid material. More experiments and simulations are required to clarify and to understand the observed phenomenon.

5. Conclusions

The behaviour of surface charge deposited by impulse positive corona on samples of two polymeric materials, EPDM and SIR, has been studied. It was found that the spatial spread of the surface charge was dependent on the amount of the deposited charges defined by the level of the charging voltage and the number of applied impulses. The higher charging voltage or more impulses applied, the wider spread of the surface charge was recorded. The temporal and spatial variations of the surface potentials were found to correlate with material surface and volume resistivities, however, the influence of these parameters on potential decay rates decreased with increasing amplitude of the voltage or number of the applied impulses.

Acknowledgements

This work has been supported by the Swedish Energy Agency, Elforsk, ABB and Areva.

References

[1] HACKAM R., IEEE Trans. Dielect. Elect. Insul., 6, (1999), 585.

[2] BLENNOW J., SÖRQVIST T., *Effect of Surface Charge on Flashover Voltage of Polymer Materials,* Proc. 19th Nordic Insul. Symp., Trondheim, Norway, June 2005, 13–15.

[3] ZHOU Y.X., ZHANG B.L., BU D., WANG N.H., WANG N.Y., LIANG X.D., GUAN Z.C., *Nanosecond Pulse Corona Charging of Polymers*, IEEE Trans. Dielect. Elect. Insul., 14,(2007), 495.
[4] SERDYUK YU.V., GUBANSKI S.M., *Computer Modelling of Interaction of Gas Discharge Plasma with Solid Dielectric Barriers*, IEEE Trans. Dielect. Elect. Insul., 12 (2005), 725.
[5] MAUSETH F., *Charge Accumulation in Rod-plane Air Gap with Covered Rod*, PhD Thesis at NTNU, 2007.
[6] BAUM E.A., LEWIS T.J., TOOMER R., J. Phys. D: Appl. Phys, 10 (1977), 487.
[7] BAUM E.A., LEWIS T.J., TOOMER R., J. Phys. D: Appl. Phys, 10 (1977), 2525.

Received 2 May 2007
Revised 17 August 2007

Materials Science-Poland, *Vol. 27*, *No. 4/2*, *2009*

Experience with optical partial discharge detection

M. MUHR*, R. SCHWARZ

Institute of High Voltage Engineering and System Management,
Graz University of Technology, Inffeldgasse 18, 8010 Graz, Austria

Partial discharge (PD) diagnostics was used to evaluate electrical insulations of high voltage equipment as a quality control and to detect insulation deterioration. Improvements, new developments as well as lower costs of sensors, electronics and processing units are some reasons for the increasing usage of PD measurements. The paper presents investigations in the area of optical partial discharge measurement technique. In an overview, PD measurement systems were presented, advantages and disadvantages of the optical method were discussed. An unconventional optical partial discharge detection system was developed and comparative measurements to a conventional electrical PD measurement system were accomplished. The system was tested by using a PD source in air or alternatively in oil to evaluate the sensitivity and the impulse behaviour in correlation to the conventional measurement technique.

Key words: *partial discharge; optical spectrum*

1. Introduction

Partial discharges are local enhancements of the electric field in the area of inhomogeneities, either in gaseous, liquid or solid media. The presence and the strength of partial discharges are criterions for the evaluation of the insulation quality of the electrical equipment. On one side, partial discharges only have a small short time of influence on the electrical firmness of electrical resources. On the other side, a long time of influence shows a destructive effect predominantly on organic insulation systems, which degrade the electrical characteristics of the insulation or the insulation systems. This can lead to a breakdown and a failure of the electrical resource.

The partial discharge measurement is a sensitive, non-destructive method for testing and monitoring the condition of insulation of a high voltage equipment. Various techniques are used for detection and localisation. Apart from the conventional current pulse flowing in the circuit, partial discharge activity can also generate weak light, acoustic signal, local temperature rise, etc. Various techniques have been explored to measure partial discharge activities in various apparatuses.

*Corresponding author, e-mail: muhr@hspt.tu-graz.ac.at

2. Basics

For the measurements, physical effects such as optical, chemical, electrical and acoustical appearances, were used.

2.1. Optical partial discharge detection

The optical partial discharge detection is based on the detection of light produced as a result of various ionization, excitation and recombination processes during the discharge. However, the optical spectrum of different types of discharge is not the same.

The amount of the emitted light and its wavelength depends on the insulation medium (gaseous, liquid or solid) and different factors (temperature, pressure etc.). Thus the spectrum of the light emitted by partial discharges depends on the surrounding medium and the intensity of the discharge. The optical spectrum extends from the ultraviolet over the visible range into the infrared one [1]. For example the wavelength of faint corona is lower than 400 nm. The main part falls in the ultraviolet region. The wavelength of a strong flash discharge is between 400 nm and 700 nm. The spectrum of surface discharges along a solid dielectric is more complex and influenced by many factors such as solid material, surface condition including composition of gases etc. [2].

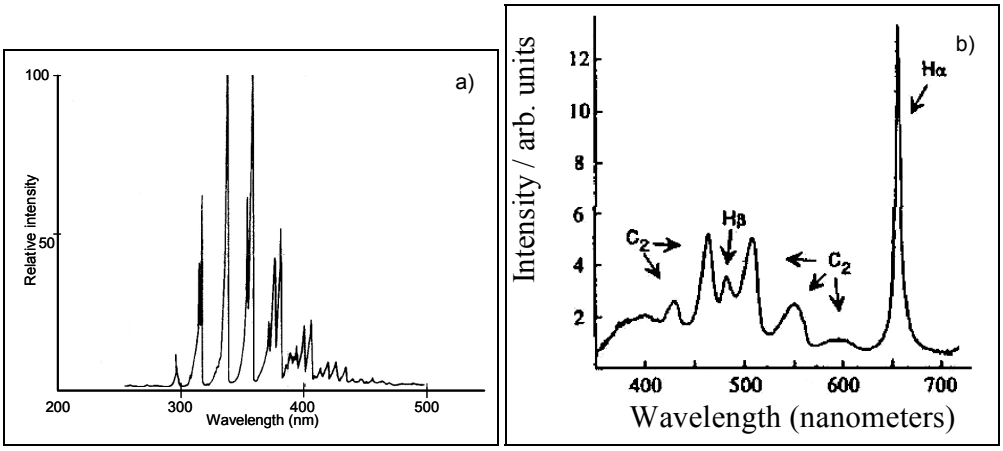

Fig. 1. Typical emission spectra: a) corona discharge, b) discharge in oil

In gases under low pressure, a very small fraction of the energy (1%) of the partial discharge may be emitted as light [3]. In liquids and solids, this part is still smaller in comparison to the total energy. In a rough approximation, the light emitted by partial discharge is proportional to their charge. Nitrogen dominates the optical spectrum of discharges in air. 90% of the total energy of the emitted optical spectrum of PD is in the ultraviolet region. The corona discharge emits radiation in the 280–405 nm spec-

tral range, mostly in the ultraviolet (UV) (Fig. 1a). The main part of the emission is invisible to the human eye. A relatively weak emission at about 400 nm might be observed at night under conditions of absolute darkness.

Hydrogen however has its emission spectrum in the visible region and a smaller part in the infrared one. The spectrum of SF_6 lies in the ultraviolet and in the blue -green region of the visible light. Transformer oil exhibits emission in the range from 350 nm to 700 nm, depending on oil composition (Fig. 1b). The emission spectrum of oil is predominantly formed by hydrogen and hydrocarbons such as methane, ethane and ethyl.

2.2. Classification of the measurement techniques

Radiation due to electrical discharge may lie in the ultraviolet, visible or infrared region. Depending on the wavelength range of the spectrum, sensors with various optical systems should be chosen: UV corona scopes, night vision, low-light enhancers, photodiodes, photomultipliers.

Three categories of optical PD detectors are available: imaging, quantitative non-imaging and optical/electric detectors

Two different measuring techniques (applications) can be used. The techniques for the optical detection on the surface of the electrical equipment (A) and techniques to detect the optical signal inside of equipments in combination with fibre optic cables as sensors and as transport media for the optical signal (B).

A. Surface discharge outside the equipment. UV radiation emission measurements and observations with a night-vision device for detection of corona and other electrical discharges on surfaces are used. With a daylight–UV inspection camera corona and arc localization can be accomplished at high voltage transmission lines and in power

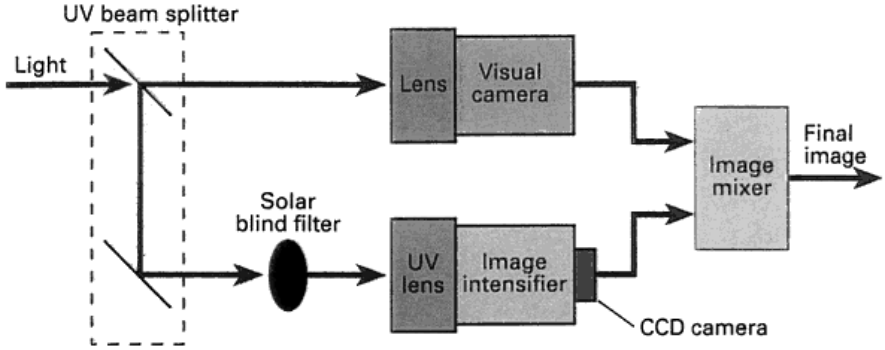

Fig. 2. Operation diagram camera DayCor II™ [4]

stations. The DayCor® corona camera is a bi-spectral Solar Blind UV–Visible imager [4]. The UV channel works within the so-called sun blind range from 240 nm to 280 nm of

the UV region. In this wavelength range, the UV radiation of the sun is absorbed perfectly by the ozone layer before reaching the earth. Due to this particularly developed filter, those UV rays can be produced by fires or electrical discharges also by day without the sunlight.

The camera has two representation channels and contains an UV sensitive channel for the corona discharge and the second within the visible range for the admission of the environment. Both images are superposed and result in a video picture (Fig. 2).

B. Surface discharge "inside" the equipment. If a high voltage equipment is enclosed and light tight as transformer or GIS (environment light are totally enclosed), an optical detection under the use of fibre optical technology is possible. An optical fibre collects the light produced by partial discharges inside the equipment and transmits the signal outside to a detection unit. The optical characteristics of different fibre optic cable and optical detector materials (the relative spectral sensitivity in function of the wavelength) must be considered.

2.3. Opto-acoustic partial discharge measurement

A modified form of optical detection is to influence an optical signal within a fibre optic cable by the acoustic wave (pressure) produced by the partial discharge. During a partial discharge in gas or oil, an acoustic wave in the sonic and ultrasonic range is generated. If a PD in the surrounding medium arises, the pressure wave results in a deformation of an optical fibre and its optical transmission characteristic is changed. It comes to a mechanical stress and a stretch of the fibre and an influence of the used polarized light by this fibre too. The result is a change of the optical distance as well as the polarization condition. This fact is used by the opto-acoustical sensor principle. So the optical fibre methods involve optical phase modulation by the pressure. Interferometry is used and intrinsic interferometers based on optical fibre.

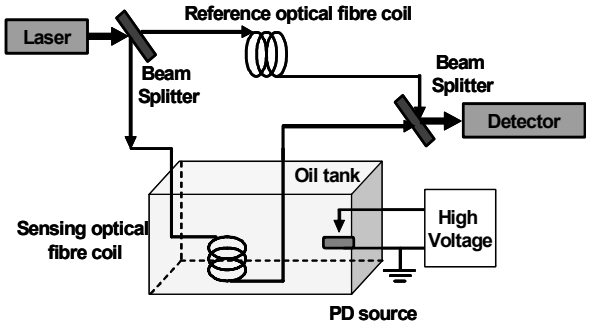

Fig. 3. Experimental setup of the optical interferometric detection of PD [5]

Figure 3 shows the scheme of the Mach–Zehnder interferometer with optical fibres in the reference and sensing arms. Both arms have the same lengths and are con-

structed with identical coils. The sensing optical fibre coil is in the oil tank and can be affected by the partial discharge signal (pressure), the other fibre is isolated from the impact of the acoustic wave and used as the reference arm for the optical path of the light. The interferometer is illuminated with a coherent light source. A beam splitter is used at the laser output to divide the light for the two fibre coils and also a mixer is used for the recombination of the two beams focused onto the optical detector [5].

The partial discharge measuring technique as a part of the insulation diagnose is an object of investigations at the Institute of High Voltage Engineering and System Management at the University of Technology in Graz. A scientific project deals with the economic possibilities of the optical detection of partial discharge with special fibre optic cables and the acquisition of the impulse behaviour of PD in various isolating media.

3. Investigations

An optical system for PD detection for converting the light into electrical signals and a detection unit was developed. The system consists of a lens or alternatively a special fluorescent fibre optic cable in front of a conventional fibre optic cable, which is connected to a photodiode alternatively to a photomultiplier for the conversation of the light into an electric signal. Various procedures of the light linking into the fibre optic cable, as well as various geometrical arrangements to the source of partial discharges were analysed. One method is to use a lens system in front of the optical fibre. Another method is using a fluorescent optical fibre, whereby the light penetrates over its surface into the fibre (Fig. 4). The light signal is coupled into the optical fibre and at the end of the fibre the signal is transmitted to the photodiode and/or a photomultiplier and the amplifier circuit.

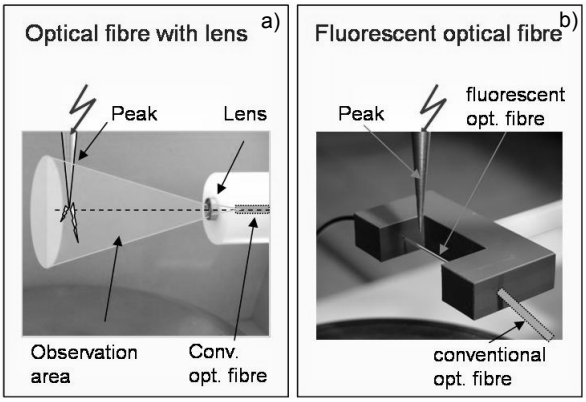

Fig. 4. Optical fibre arrangement in front of a peak electrode:
a) lens and conventional optical fibre,
b) fluorescent and conventional optical fibre

A peak-plate arrangement as a test setup is used for the PD measurement. The distance between the peak and the plate can be changed in a range 1–20 cm, and the voltage supply from 0 to 100 kV. As isolating media, air or oil (transformer oil) under normal pressure are used. The experimental setup is placed in a shielded and darkened high voltage room in order to prevent influences from outside.

Investigations with an conventional detection systems according to IEC 60270 in comparison to the optical system were carried out. The PD pulses were observed simultaneously by the used systems. Further investigations about the PD impulse behaviour at ac and dc were made.

4. Test results

In Figure 5, PD impulses in air are shown measured by conventional and optical measurement systems.

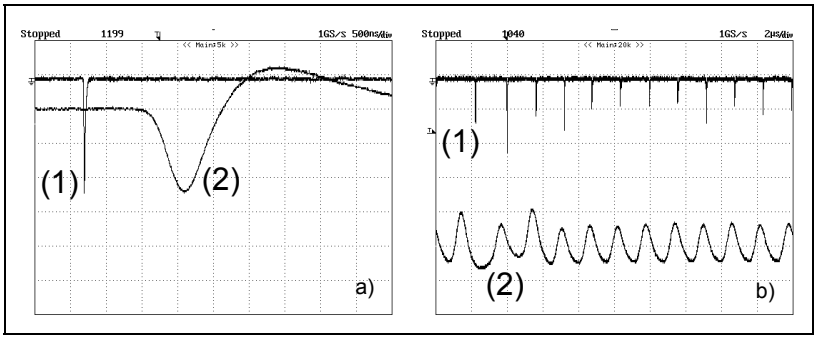

Fig. 5. Conventional detected PD signal (2) and optical detected impulses (1) in air with: a) fluorescent fibre, b) lens

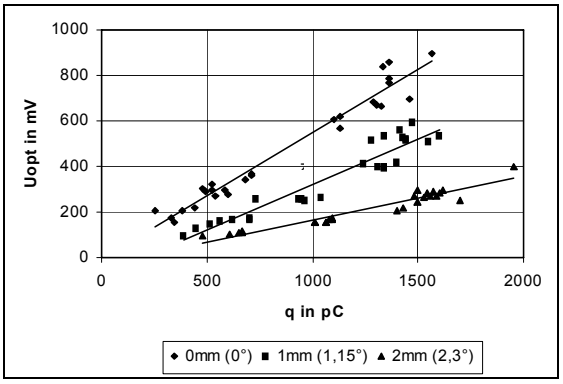

Fig. 6. Output voltage of the optical system as a function of the apparent charge during angle (0°–2.3°) dependent light linking (air, lens)

The PD impulses (Fig. 5) measured with the optical system (1) show the rise time ca. 5 ns and the impulse duration of ca. 20 ns. The signal processing of the used conventional system (2) results in the time delay of about 1μs and also an signal extension of about 2.5 μs. There is a good correlation between the conventional measured PD signal (in air) and the output signal from the optical system (Fig. 5 and Fig. 6). By varying the angle to the PD source between the peak and the sensor (lens + optical fibre), a change in the peak value of the light pulse was observed as shown in Fig. 6.

In oil, the detected discharges are scattered in amplitude and shape. Positive streamers show a superposition of fast pulses and negative streamers are composed of a burst of fast pulses of growing intensity. The PD impulse amplitude and the repetition rates were randomly distributed within the acquisition period.

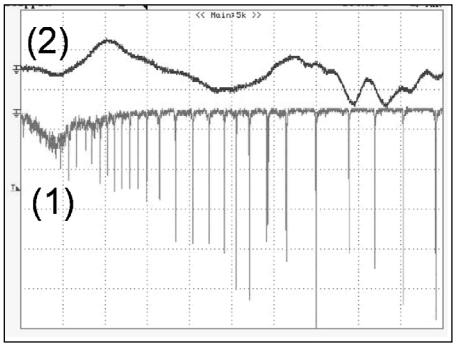

Fig. 7. Comparison of a conventional detected PD signal (2) and optical detected impulses (1) in oil

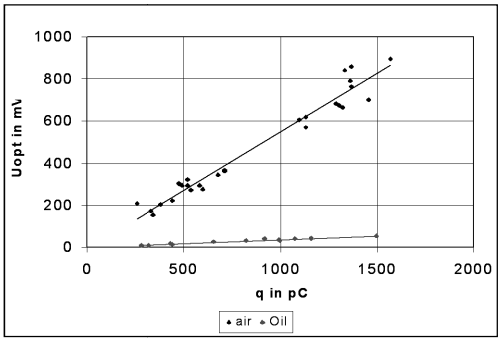

Fig. 8. The relationship of the optical signal and the discharge level in air and in oil at the same arrangements

The result (Fig. 7) shows that the conventional PD system (2) with the limited bandwidth of the measuring technique cannot correctly represent fast impulses in oil. A dependence of the detected single impulses of the optical system (1) on the result of the conventional PD measurement (2) could not be found (exception: occasionally arising single pulses with a larger pulse interval). Both the air and the oil gap conditions were measured and the relationship between the electrical and optical signal is shown in Fig. 8.

In air and in oil different discharge behaviours, optical absorptions, as well as different spectral regions of the radiated light are present. This also influences the characteristic of the optical system change, evidently caused by the large differences in the received output signals (Fig. 8).

5. Conclusions

The optical measurement is a sensitive method in comparison to the conventional electrical techniques especially by on-site measurements. Other advantages of this

method are the immunity to EMC and insensitivity to electromagnetic and acoustic interference sources. Thus the light detection is not affected by the environmental noise and highly flexible and large bandwidths of the system. Furthermore, the optical partial discharge detection can be simply used under impulse voltage condition.

Air and SF_6 are almost to 100% transparent, thus the light can be detected from a lager distance. Adverse in liquids and solid insulations, a section or the whole emitted light will be absorbed and no detection is possible. Also in comparison with the conventional measuring the optical detection of PD cannot be calibrated.

References

[1] SCHWARZ R., *Optische Teilentladungsdiagnostik für Betriebsmittel der elektrischen Energietechnik*, Dissertation, TU, Graz, 2002.

[2] CHEN G., YANG X., MING Y., XIAOLONG C., CHANGRONG Q., *Comparison between optical and electrical methods for PD measurement*, The 6th International Conference on Properties and Applications of Dielectric Materials, Xian, June 2000.

[3] FORSYTH K.W., *Optical partial discharge detection*, Iris Rotating machine Technical Conference, March 1998.

[4] [http://www.daycor.com]

[5] MACIA-SANAHUJA C., L-RIVERA H., *Wavelet analysis of partial discharges acoustic waves obtained using an optical fibre interferometric sensor for transformer applications*, 0-7803-7912-8/03/ 2003 IEEE.

Received 16 April 2007
Revised 9 August 2007

Materials Science-Poland, *Vol. 27*, *No. 4/2*, *2009*

Comparative analysis of lightning overvoltages in distribution lines on the ground of laboratory tests and measurements

W. SKOMUDEK*

EnergiaPro Energetic Concern Co., Department of Opole,
Technical University of Opole, Department of Electrical Engineering, Poland

Determination of extreme voltages induced on overhead and cable power lines by nearby lightning strokes is a complex problem. Results of computer simulation (laboratory tests) and measurements of such overvoltage processes due to lightning discharges occurring in overhead and cable lines, as elements of a distribution network, are presented. A principal, simulation tool was the PSpice program.

Key words: *induced overvoltage; computer simulation; power line; lightning strokes*

1. Introduction

Rapid development of industrial processes controlled by devices in which digital-circuit engineering is used obliges distribution companies to apply up-to-date techniques and technologies. It tends towards achieving of high quality and reliability of power networks. Beyond a doubt, one of serious causes of damages of network elements are direct and indirect lightning overvoltages [7–9, 21]. Such a threat concerns electrical equipment and particularly overhead and cable power lines. Distribution networks of middle voltage (MV) include traditional overhead power lines with bare conductors or more and more frequently with covered conductors and, furthermore, power cable lines composed of three single bundle assembled cables, placed in the ground or in the air (under slung on supports).

Influences of lightning surges on power lines according to produced harmful effects can be divided into influences being operational hazard caused by excessive electrical strength within line insulation systems leading to their degradation and influences posed a threat to the environment (electric shock hazard). In the former case

*Corresponding author, e-mail: waldemar.skomudek@pse-operator.pl

a measure of influences are induced overvoltages of high amplitude and frequency during a transient state in the circuit composed of a conductor and a thunderstorm cloud caused by electromagnetic field (generated by a lightning current). The other case is related first of all to electromagnetic field as a consequence of passage of lightning current by metallic coating of cables; a measure of dangerous influences in this instance is the voltage between the metallic coating and the ground.

Theoretical considerations dealing with overvoltages induced on power networks can be based on mathematical models worked out by Rusck, Agraval or Taylor [1, 3, 4, 6, 13, 20]. The principle for description of line elements pertinent to conditions of induced overvoltages is a general Maxwell equation in vectorial form:

$$\nabla^2 \mathbf{E} = \mu\varepsilon \frac{\partial^2 \mathbf{E}}{\partial t^2} \tag{1}$$

equivalent to three scalar equations in the Cartesian coordinate system:

$$\begin{aligned}
\frac{\partial^2 E_x}{\partial x^2} + \frac{\partial^2 E_x}{\partial y^2} + \frac{\partial^2 E_x}{\partial z^2} &= \mu\varepsilon \frac{\partial^2 E_x}{\partial t^2} \\
\frac{\partial^2 E_y}{\partial x^2} + \frac{\partial^2 E_y}{\partial y^2} + \frac{\partial^2 E_y}{\partial z^2} &= \mu\varepsilon \frac{\partial^2 E_y}{\partial t^2} \\
\frac{\partial^2 E_z}{\partial x^2} + \frac{\partial^2 E_z}{\partial y^2} + \frac{\partial^2 E_z}{\partial z^2} &= \mu\varepsilon \frac{\partial^2 E_z}{\partial t^2}
\end{aligned} \tag{2}$$

where each component of the electric field intensity vector **E** satisfies the wave equation.

In real power networks, due to dissipation of high-variable electromagnetic field, the following tendencies are observed: decrease of peak voltages and change of waveforms during a nonstationary state. Suppression and deformation of waves (caused by influence of a series resistance of conductors, change of soil resistivity of soil, and occurrence of dynamic corona) can be modelled on the ground of processing programs.

However, owing to computer techniques:

– analyzes of induced lightning overvoltages are facilitated,

– mathematical model of lightning discharge canal has been perfected,

– solution of complex equations describing electromagnetic field has been simplified,

– a model of power system elements has been more detailed,

– computer simulations enable us to record variation of overvoltages at various points of an analyzed network area.

Evaluation of overvoltage hazard dealing with power line and cable insulating systems in various networks has been presented in numerous papers [2, 10, 11, 12, 16]. It has been pointed that application of PSpice program (Design Center Eval packet) to simulate transient states caused by lightning overvoltages is possible [14, 15]. Such

a statement is significant because PSpice program was intended in principle for electronic circuits.

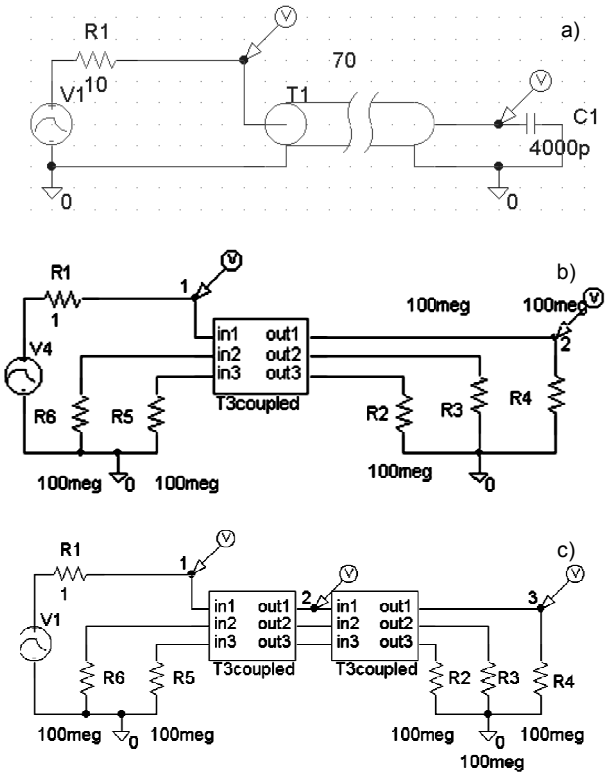

Fig.1. Schematic diagrams of the sections of simulated systems composed of:
a) overhead line segment, b) cable line segment, c) mixed system segment.
V1, V4 – input pulse sources, R1 – internal resistance of a source, C1 – capacitance,
T1, T3 – models of power overhead line and cable line, R2–R6 – loading resistances

In the paper, the results of computer simulation of transient states due to direct and induced lightning overvoltages have been compared with the results of laboratory tests of models and those of measurements of overvoltages in real conditions. The latter case concerns power MV lines operated in a mixed system, i.e. overhead line connected with a cable line of different lengths. Final conclusions are formulated based on results of computer simulation.

2. Computer simulations

Computer simulation of transient states resulting from atmospheric discharges realized by means of processing programs, enables one to analyze transient states occurring within electric (electronic) systems in real time. Such programs, also employed to

design overvoltage protective systems, can be of various types depending on their function. The most known are Electro-Magnetic Transients Program program (EMTP) and Simulation Program with Integrated Circuits Emphasis (PSpice program) but others programs are also used to analyze of selected electrical processes. It is important that results of simulation should be verified (in respect of their quantity and quality) by comparing them with results of measurements related to physical models or – better – to real technical objects.

During numerous measurements and simulations a certain regularity has been noticed: wave front time of excitation impulse affects visibly overvoltages in particular elements of a power system. In order to confirm a level of overvoltage hazard and to determine the influence of wave-front time duration on rate-of-rise of the voltage stressing insulation, a computer simulation (using PSpice program) has been carried out [5].

Quick-variable passages of electromagnetic energy cause overvoltages of very high frequencies so each power overhead line and cable line during simulation should be treated as an element with distributed parameters. The following parameter values have been admitted:

- cable line (C_0 = 0.1 μF/km; L_0 = 0.49 mH/km; R_0 = 0.0289 Ω/km; Z_0 = 70 Ω; v = 142.86 m/μs)
- overhead line (C_0 = 7,37 μF/km; L_0 = 1.71 mH/km; R_0 = 0.35 Ω/km; Z_0 = 482 Ω; v = 281.69 m/μs).

Stimulation of design systems is an impulse (pulse) with exponential edges and variable values of parameters (Fig. 2). Simulations have been carried out for three systems presented in Fig. 1.

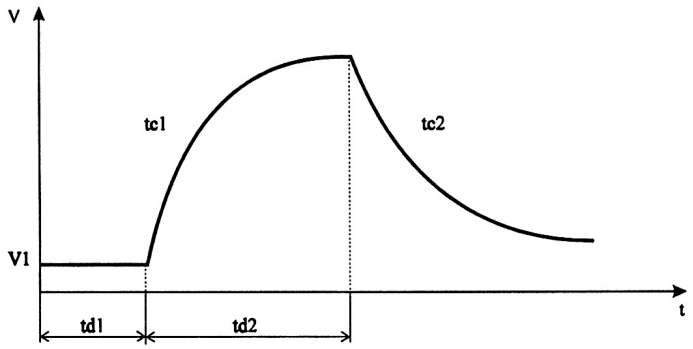

Fig. 2. Stimulation of a design system with exponential characteristic, accessible in PSpice program: t_{d1} – rise delay, t_{d2} – fall delay, t_{c1} – rise time, t_{c2} – fall time

Equivalent active parameters of power line conductors during overvoltages increase their values due to a skin effect. Such a phenomenon occurs also in a layer of

the soil and affects inductance of lines. In turn, dynamic coronas change capacities of lines. Each of these phenomena influences: wave impedance, velocity of wave propagation along conductors and deformation of impulse waves (Fig. 3c).

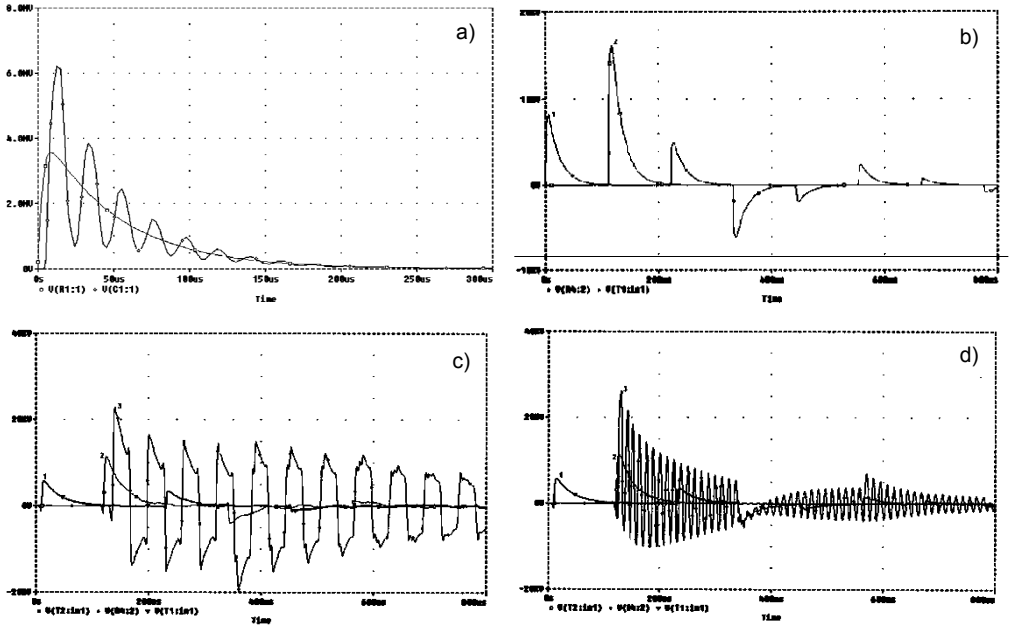

Fig. 3. Chosen time-dependent overvoltages occurring at points fixed in Fig. 1 for:
a) one-phase overhead line, b) three-phase cable line, c) three-phase mixed system of overhead l = 5000 m and cable line l = 500 m and d) three-phase mixed system of overhead l = 1000 m and cable line l = 500 m

Prospective failure frequency of MV power network elements due to lightning strokes is considerable. In some cases, that may lead to multiple damages of insulating systems. It has been proved by mathematical analyses and computer simulations (Fig. 3d). On the other hand, internal overvoltages generated during transient states are not a significant threat because impulse strength of insulating systems is much higher than prospective peak values of internal overvoltages.

Results of simulation prove that each direct lightning stroke in electric power elements and almost each nearby lightning stroke causes multiple reflections of waves leading to flashover or breakdown of insulating systems (Fig. 3). Occurrence of such breakdowns at many places of power cable lines is a very probable event.

The highest value of the voltage stressing insulating systems during lightning overvoltages depends positively on time parameters describing an overvoltage, i.e. time-constants t_{c1} and t_{c2} (relating to an aperiodic component of rise/fail delay of the wave). Time-dependent overvoltages in Fig. 3 are damped; they pose a threat to insulating systems as amplitude of stimulating signal increases or shape factor value the signal decreases (Fig. 4).

Computer simulation enables us to obtain numerous time-dependent overvoltages which prove that wave-front time of these overvoltages does not affect rate-of-rise of the voltage stressing insulating systems within individually screened cables. However, such a regularity is not confirmed towards belted cable.

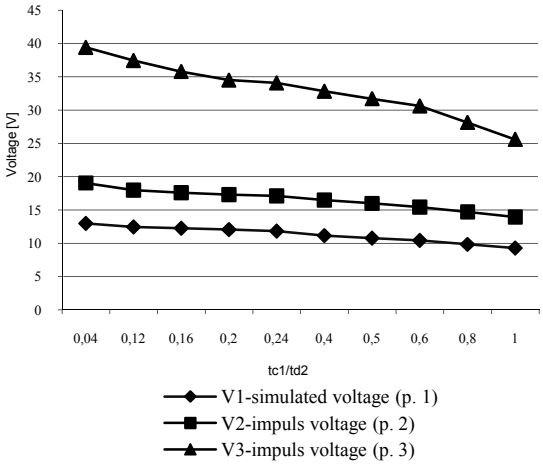

Fig. 4. Levels of voltage induced at measuring points 1, 2, and 3 from Fig. 1c depending on shape factor of stimulation pulse value – t_{c1}/t_{d2} (Fig. 2)

In the case of belted cables (network elements of frequent occurrence) decreasing of slope of the wave-front (input pulse) causes additional displacement of response amplitude towards longer lines; such a regularity has been proved during laboratory tests and investigations of real systems (Figs. 6a and 8). A displacement of response amplitudes during lightning overvoltages is caused by heterogeneity of metallic coating which affect increase of electromagnetic field dissipation and wave impedance of cables with not screened conductors in respect of cables with concentric conductors.

3. Laboratory tests and investigations in selected real lines

Results obtained from the simulation process have been verified based on the measuring system made both for single-core screened and three-core belted cables (Fig. 5). The system was equipped with a special pulse generator which allows us to regulate the slope and wave front duration. In the case of three-core line only the generator of rectangular pulses energized one from all the conductors.

Transient time-dependent voltages caused by the pulse in the energized conductor (in the three-core line and in non-energized neighbouring conductors) have been recorded by means of a multi-channel digital oscilloscope. The obtained transients reveal that pulse time parameters at the input of the examined system have great impact on the shape of reflected and induced waves in neighbouring cable wires. However, in

the case of unscreened cables, lowering of the input pulse inclination causes additional shifting of reflection amplitude to longer timing.

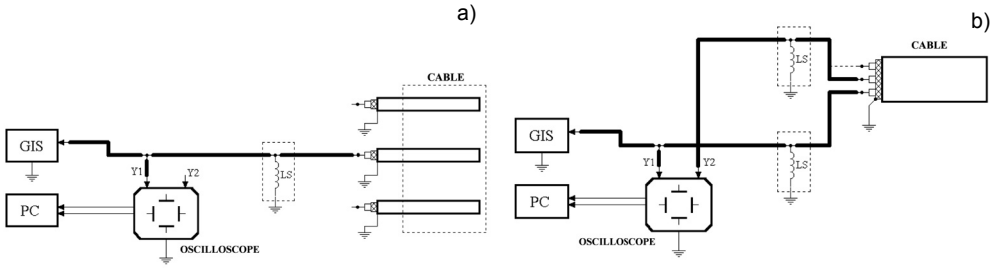

Fig. 5. Scheme of the measuring system [14] for: a) single-core concentric line, b) three-core belted cable; LS – system protection, Y1, Y2 – oscilloscope canals, GIS – pulse generator

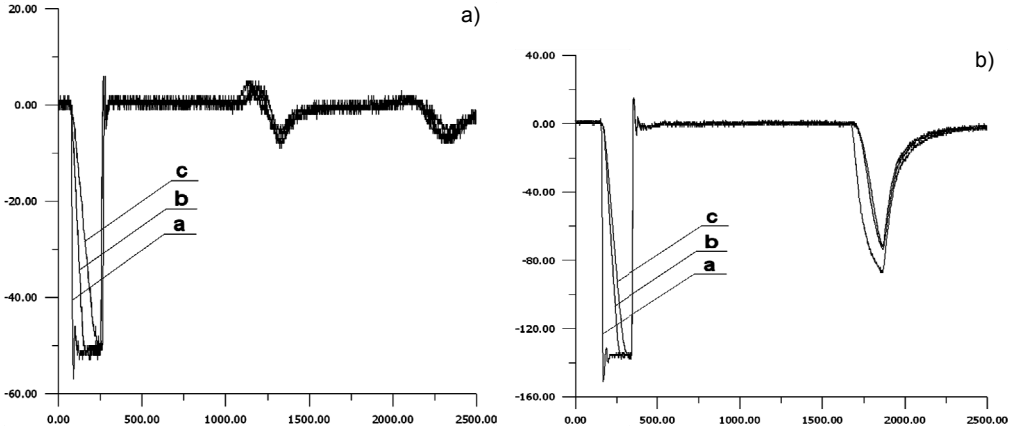

Fig. 6. Time-dependent overvoltages occurring in line models [13]:
a) traditional three-core, b) single-core; input signal: amplitude 4.1 V, breadth $\Delta t = 250$ ns;
a, b, c – input impulses V_a, V_b, V_c for various pulse rise times

Results of laboratory tests, carried out for two chosen type of lines, are presented in Fig. 6. Recording of time-dependent overvoltages in real overhead/cable lines between high voltage station Prudnik and medium voltage-to-low voltage station Oczyszczalnia has been made similarly [17, 18]. As a source of stimulation, a 12 kV test transformer was used. Chosen test results for various pulse rise times of wave front overvoltage are presented in Fig. 7.

Initiation of travelling waves in power network leads to occurring of periodical variable voltages (overvoltages) at the ends of power lines as an effect of multiple wave reflections. Such overvoltages, after several periods, cause considerable deformation of waves in comparison with a stimulation pulse.

Shapes, amplitudes and reciprocal displacements of overvoltages recorded during tests (Figs. 7, 8) are compatible with theoretical wave phenomena. Investigations carried out in network elements [19] and in laboratory models confirm results

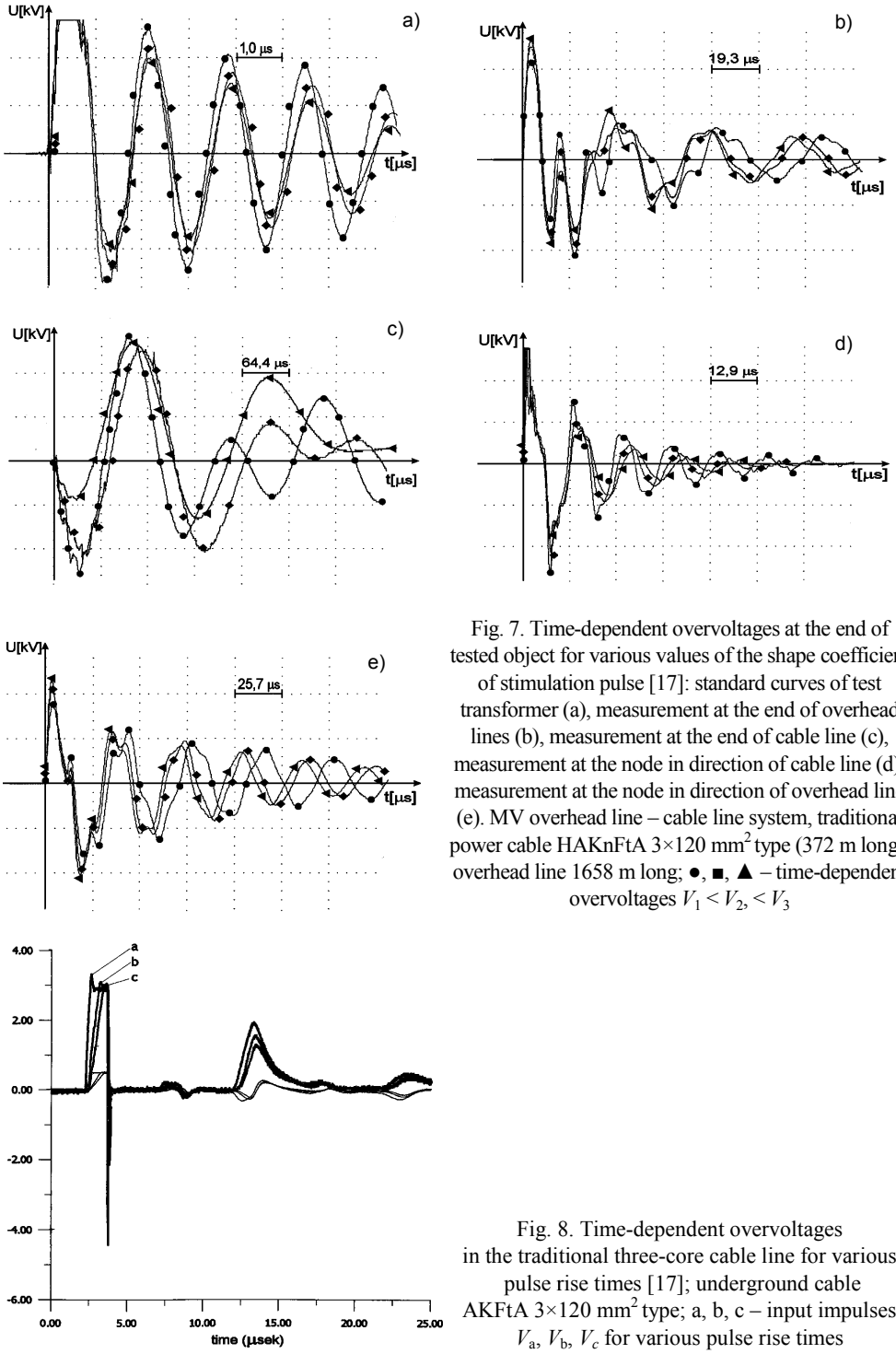

Fig. 7. Time-dependent overvoltages at the end of tested object for various values of the shape coefficient of stimulation pulse [17]: standard curves of test transformer (a), measurement at the end of overhead lines (b), measurement at the end of cable line (c), measurement at the node in direction of cable line (d), measurement at the node in direction of overhead line (e). MV overhead line – cable line system, traditional power cable HAKnFtA 3×120 mm^2 type (372 m long), overhead line 1658 m long; ●, ■, ▲ – time-dependent overvoltages $V_1 < V_2, < V_3$

Fig. 8. Time-dependent overvoltages in the traditional three-core cable line for various pulse rise times [17]; underground cable AKFtA 3×120 mm^2 type; a, b, c – input impulses V_a, V_b, V_c for various pulse rise times

of computer simulations concerning the nodes and points of discontinuity where wave impedance undergoes changes. However, it is advisable to verify additionally the obtained results by means of other processing programs (e.g., EMTP). It aims also at selection of the most suitable informatics tool to analyze transient states in power networks.

4. Conclusions

- Tests and many years of observations of atmospheric discharges show that peak value and steepness of wave front are random values of negligible correlation. This means that these parameters can be analyzed independently.
- Analysis results of computer simulations, laboratory tests, and measurements in real power networks prove that time duration of an overvoltage does not affect the rate of rise of the voltage stressing insulating systems in overhead lines. Such a conclusion is true for individually screened cables. Dominant influence of the voltages stressing insulating systems in line elements, due to overvoltage processes, are their parameters: the rate of rise and time duration of a wave.
- PSpice program applied to analyze overvoltage processes in power systems enables one to reproduce easily a stimulation pulse, to observe propagation of voltage waves in the first phase of a transient state and afterwards – when a wave reaches a node point. An analysis of the influence of wave processes in multiple conductor lines on the overvoltages in particular conductors is possible too.
- An analysis of time dependent voltages as a result of simulation processes with models accessible in the program shows that PSpice program is a convenient simulation tool, although obtained models do not take into account two essential phenomena: skin and corona effects during transient states. Such imperfections overstate amplitudes of signals returned from the lines.
- Due to dynamic corona effect, the velocity of wave propagation decreases nonlinearly when actual values of impulse voltage increase. This causes a favourable effect consisting in deformation of impulse waves and in decrease of their slopes.

References

[1] AGRAWAL A.K., PRICE H.J., GURBAXANI S.H., IEEE Trans. Electomagn. Compat., EMC-22 (1980), 119.
[2] ANDREOTTI A., DE MARTINIS U., VEROLINO L., Adv. Eng. Software 31 (2000), 757.
[3] BAJOREK J., GAMRACKI M., *Effectiveness of mathematical modelling of lightning coupling to overhead conductors*, Proc. 26th Int. Conf. Lightning Protection, Cracow, 2002, 208–213.
[4] BAJOREK J., MASŁOWSKI G., *Mathematical models of electromagnetic field of lightning*, Proc. 22nd Inte. Conf. SPETO, Gliwice–Ustroń 1999, 97–100.
[5] BARANOWSKI K., WELO A., *Simulation electronics chosen. MIKOM*, Warsaw, 1996 (in Polish).
[6] COULSON C.A., JEFFREY A., *Waves, mathematics models*. WNT, Warsaw, 1982.
[7] FLISOWSKI Z., KOSZTALUK R., Przeg. Elektrotechn., No. 2, 1997 (in Polish).

[8] GACEK Z., SKOMUDEK W., *An analysis of overvoltage hazard due to lightning discharges in medium voltage overhead lines with covered conductors*. Proc. of the 12th Int. Symp. High Voltage Engineering – ISH, Delft, 2003, 77.
[9] GACEK Z., SKOMUDEK W., Energetyka, No. 1, 2003 (in Polish).
[10] KRAFT L.A., IEEE Trans. Power Syst., 6 (1991).
[11] MCDERMOTT T.E., SHOT T.A., ANDERSON J.G., IEEE Trans. Power Delivery, 9 (1994).
[12] NUCCI C.A., RACHIDI F., IANOZ M, MAZZETTI C., IEEE Trans. EMC, 35 (1993), 75.
[13] RUSCK S., *Induced lightning overvoltages on power transmission lines with special reference to the overvoltage protection of low voltage networks*. Ph.D. Thesis, the Kungi, Tekniska Hogskolan, Stockholm, Sweden, 1957.
[14] SKOMUDEK W., J. Electr. Eng., No. 5–6, Slovakia, 2004.
[15] SKOMUDEK W., *Evaluation to make use of PSpice program to modelling lightning inducted voltages of power systems*. Computer Application in Electrical Engineering, Zakopane, 2005.
[16] SKOMUDEK W., GACEK Z., *Influence of selected parameters of overvoltages on hazard of insulating systems in MV power lines*. Electronic and Electrical Engineering, No. 2, Lithuania, 2006.
[17] SKOMUDEK W., *Registration of time dependent overvoltages in authentic overhead/cable lines between 15/0.4 kV switching stations: Prudnik and Oczyszczalnia Prudnik*. 7, 2004 (in Polish).
[18] SKOMUDEK W., *Registration of time dependent overvoltages in authentic cable lines in GSZ Cementownia Górażdże*, Chorula, 11, 2004 (in Polish).
[19] TARCZYŃSKI W., SKOMUDEK W., *Wave phenomena in MV cable lines*, Rep. from own tests, Opole 2004 (in Polish)
[20] TAYLOR C.D., HARRISON C.W., SATTERWHITE R.S., IEEE Trans. Antennas Propagat., AP-13, 1965.
[21] YOKOYAMA S., IEEE Tran. Power App. Syst., 103 (1984).

Received 20 April 2007
Revised 21 July 2007

Proszę podać nr strony w Ref. 10, 11, 20, 21

Materials Science-Poland, *Vol. 27*, *No. 4*, *2009*

Return voltage measurements Diagnostic interpretations based on the dielectric time constants

R. PATSCH*, D. KAMENKA, J. MENZEL

Institute of Materials and Diagnostics in Electrical Engineering, University of Siegen, Germany

Return voltage measurements of paper-oil insulations such as medium voltage cables have proven to be a reliable method to determine the actual state of degradation and/or the humidity of the insulation. As a first step, the interpretation of the measurements can be done based on the *p*-factor. This parameter is sensitive to the dielectric properties and especially the humidity of the solid part of the insulation, whereby aged or humid cables show a higher *p*-factor. The calculation of the dielectric time constants τ_1 and τ_2 of the two insulating materials oil and cellulose is unique for the return voltage method and hence exceeds the information extractable from other diagnostic methods.

Key words: *return voltage; paper-oil insulation; boundary polarization; ageing; Maxwell model; dielectric time constants*

1. Basics of the return voltage method

The principle is known for many years [1–3], the readings are reproducible and reliable, at least with regard to the collection of the data but unfortunately not always with regard to all methods of interpretation. Return voltage measurements are less sensitive to disturbances by external noise, a situation that is favourable for measurements in the field. The extractable information is comparable to that derived from other dielectric methods like e.g., measurements of polarization and depolarization currents [4, 5].

The experimental procedure consists of the following: application of a dc voltage U_p for the time t_p, formation of a short circuit for the time t_d, and measurement of the voltage that builds up between the external electrodes after the release of the short circuit. Commonly used parameters of the return voltage curves are the peak voltage U_m, the time t_m of the voltage peak and the initial incline *s o*f the curve. In many cases,

*Corresponding author, e-mail: rainer.patsch@uni-siegen.de

a linear dependence of the return voltage curve on the height of the poling voltage exists but in some cases a sublinear dependence may indicate some ageing. The *p*-factor defined as

$$p = \frac{U_m}{st_m} \tag{1}$$

does not depend on the height of the poling voltage U_p and is also independent of the geometric parameters of the cable. Ageing and degradation processes increase the *p*-factor.

2. Interpretation of experimental results

The analyses of time dependences of return voltage or of polarization and depolarisation currents are often done by a numerical fit based on equivalent circuits consisting of three or more RC series elements with different time constants in parallel (Fig. 1b shows only one RC-element). This equivalent circuit is physically adequate for the description of atomic polarization processes in insulating materials, namely for molecules with different polarizabilities. For other processes such as e.g., the built-up of space charges or boundary polarization processes such an equivalent circuit is just a tool for a formal mathematical fit without any correspondence to physical parameters.

3. Dielectric behaviour of a multilayer insulation

The insulation of classic power equipment such as oil filled power transformers or cables with paper-oil insulation consists of different insulating materials with different dielectric properties (ε_r and σ) and thus – in addition to molecular processes in the short time range – shows the phenomenon of boundary polarization, i.e. the accumulation of charge carriers at the boundaries between different dielectrics.

If a dc voltage is applied to the external electrodes of such a system, starting with a capacitive voltage distribution, a continuous change into a resistive voltage distribution occurs. Electric charges move within the different dielectrics and in part accumulate at the interfaces, where they generate local electric fields that are necessary to fulfil the continuity equation for the current density and the necessary correlations between the electric fields at both sides of the interface.

After removal of the poling voltage, during the short circuit an instantaneous release of the charges at the external electrodes takes place and the charges accumulated at the inner boundaries move within the dielectric materials, thus producing a discharge current. After the release of the short circuit this current generates a voltage difference between the two external electrodes, that first increases, passes a maximum

and decreases again, thus producing the return voltage curve. In so far, no single molecular polarization or depolarization processes are responsible for the experimentally found behaviour of compound insulations during return voltage measurements.

4. Maxwell model

For boundary polarization – and this is the relevant process in power equipment with paper-oil insulation – another equivalent circuit, the Maxwell model with two RC parallel circuits in series, is more appropriate, because it closely reproduces the physical reality [6]. Figure 1a shows the basic equivalent circuit. This circuit is in good correspondence with a physical model discussed in the literature for power equipment with paper-oil insulation [7].

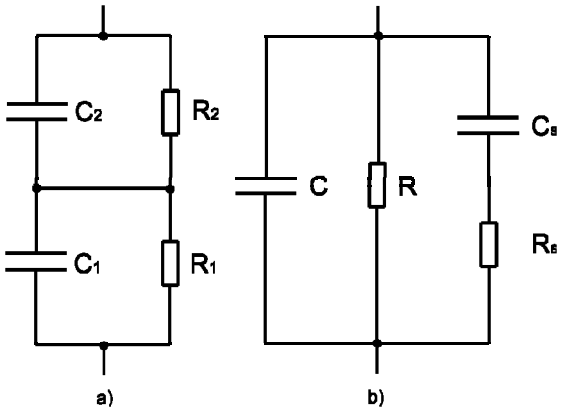

Fig. 1. Equivalent circuits to describe return voltage curves:
a) physically relevant model, b) formal equivalent circuit

The equivalent circuit in accordance to the Maxwell model can be transformed into the commonly used equivalent circuit with RC series elements that is commonly used to describe molecular polarization processes. If the measured specimen consists of two parts connected in parallel, as e.g. a cable length consisting of two parts with different properties, two Maxwell circuits in parallel must be used for the description. In the formal equivalent circuit, a second RC series element is necessary.

Both equivalent circuits shown in Fig. 1 are able to describe the return voltage curves. They can be transformed into each other [8]

$$C = \frac{C_1 C_2}{C_1 + C_2}, \qquad R = R_1 + R_2 \tag{2}$$

$$C_s = \frac{(R_2 C_2 - R_1 C_1)^2}{(R_1 + R_2)^2 (C_1 + C_2)} \tag{3}$$

$$R_s = \frac{R_1 R_2 (R_1 + R_2)(C_1 + C_2)^2}{(R_2 C_2 - R_1 C_1)^2} \tag{4}$$

$$\tau_s = \frac{R_1 R_2 (C_1 + C_2)}{R_1 + R_2} \tag{5}$$

The two equivalent circuits can be used for basic discussions, e.g. with regard to the influence of the measuring resistance R_m or the influence of a parallel capacitance C_m. The time constant τ_s of the RC series element equals the time constant τ of the Maxwell equivalent circuit during polarization or under short circuit conditions.

According to the Maxwell model, the shape of the return voltage curve $U_r(t)$ can be calculated analytically and (neglecting the influence of R_m at the moment) is given by

$$U_r(t) = U_s \left(\mathrm{e}^{-t/\tau_2} - \mathrm{e}^{-t/\tau_1} \right) \tag{6}$$

U_s is the voltage over C_1 and C_2 immediately after the release of the short circuit being influenced by the polarization voltage U_p, the elements R_1, R_2, C_1 and C_2 of the equivalent circuit the time of polarization t_p and the time of short circuit

$$U_s = \frac{\lambda - 1}{1 + \lambda + \frac{R_2}{R_1} + \frac{C_2}{C_1}}, \qquad U_p \left(1 - \mathrm{e}^{-t_p/\tau} \right) \mathrm{e}^{-t_d/\tau} \tag{7}$$

with

$$\tau = \frac{\tau_2 R_1 + \tau_1 R_2}{R_1 + R_2} \tag{8}$$

The time constants $\tau_2 = R_2 C_2$ and $\tau_1 = R_1 C_1$ of the two RC parallel elements in the equivalent circuit correspond to the physical dielectric time constants $\tau_i = \rho_i \varepsilon_i \varepsilon_0$ of the two dielectrics cellulose ($i = 2$) and oil ($i = 1$) [9] and R_m is the resistance of the measuring circuit. The correspondence of the elements in the equivalent circuit and the physical properties of the real dielectric in the measured object is obvious. The inner resistance R_p of the insulation or any other parasitic resistances at splices or terminations behave in the same way.

5. Parameters used for RVM evaluation

The three basic parameters used for the evaluation of return voltage measurements can be calculated analytically. The diagnostic parameters s and U_m contain U_s as a factor and are consequently influenced by the geometric dimensions of the object

under test. The time t_m of the voltage maximum depends only on the ratio $\lambda = \tau_2/\tau_1$ and the time constant τ_1

$$U_m = U_s \left(\lambda^{1/(1-\lambda)} - \lambda^{\lambda/(1-\lambda)}\right) \tag{9}$$

$$s = \frac{U_s}{\tau_1}\left(\frac{\lambda-1}{\lambda}\right) \tag{10}$$

$$t_m = \tau_1\left(\frac{\lambda}{\lambda-1}\right)\ln\lambda \tag{11}$$

The ratio U_m/s does not depend on U_s but only on τ_1 and the ratio $\lambda = \tau_2/\tau_1$

$$\frac{U_m}{s} = \tau_1\frac{\lambda}{\lambda-1}\left(\lambda^{1/(1-\lambda)} - \lambda^{\lambda/(1-\lambda)}\right) \tag{12}$$

In addition to the use of the standard plots of U_r over t as a first documentation of the results measurements, a more effective characterization of the results of return voltage measurements can be made by the analysis of the dependence between the two parameters U_m/s and t_m. Both parameters contain τ_1 and depend only on the ratio $\lambda = \tau_2/\tau_1$. The ratio between the two parameters can be taken as a new parameter λ [10].

The p-factor defined as

$$p = \frac{U_m}{st_m} = \frac{\lambda^{1/(1-\lambda)} - \lambda^{\lambda/(1-\lambda)}}{\ln\lambda} \tag{13}$$

eliminates not only the factor U_s but also τ_1, since s is inversely and t_m is directly proportional to τ_1. p depends only on the ratio $\lambda = \tau_2/\tau_1$ of the two time constants instead of R_1, C_1, R_2 and C_2 separately. Hence the p-factor is not only independent of the geometric dimensions of the two dielectrics but also independent of all parameter changes that influence τ_1 and τ_2 in the same way. This holds – at least in first approximation – e.g. for the influence of the temperature of the measured object. This may be important if measurements performed in different seasons of the year are compared [11]. In addition the p-factor is also independent of the height of the polarization voltage, because both, s and U_m are proportional to U_p. On the other hand, if p changes with the polarization voltage this is an indication of field dependent conductivities in the dielectrics, possibly as a consequence of ageing processes.

6. Evaluation of τ_1 and τ_2

A very interesting and unique possibility of the interpretation of the experimental results based on the Maxwell model is the possibility to use the dependence of U_m/s on

t_m to calculate the time constants τ_1 and τ_2 of the two RC elements of the equivalent circuit in Fig. 2. These time constants are characteristic of the two dielectrics paper and oil in the cable, and – important for application of the method in the field – they do not depend on the actual geometry of the specimen, i.e. neither the cable length nor the cross section of the conductor or the insulation thickness are of importance.

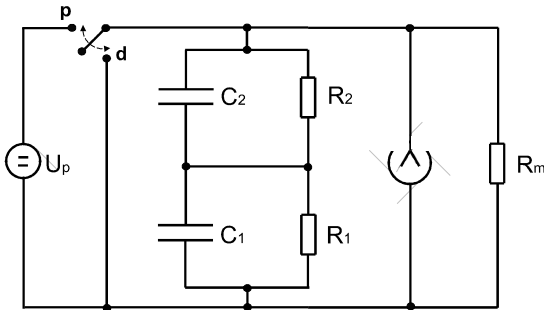

Fig. 2. Equivalent circuit of a paper-oil-dielectric with $\tau_2 = R_2C_2$ and $\tau_1 = R_1C_1$ and a basic measuring circuit

For an insulating material, the dielectric time constant τ is proportional to $\rho\varepsilon$, the product of the specific resistance ρ and the relative permittivity ε. The time constant is sensitive to changes of ρ and ε, whereby for cellulose materials the specific resistance ρ is very sensitive to the content of water. In the case of paper-oil insulations, one of the main parameters in the ageing process is the water content of the paper that on one hand accelerates ageing and on the other hand appears as a degradation product. Hence the ageing process significantly influences the corresponding dielectric time constant τ_2.

By use of the Eqs. (13) and (11) it is possible to calculate the time constants τ_2 and τ_1 directly from the experimental parameters U_m, t_m and s. The time constants are per definition independent of the specimen geometry and thus characterize directly the dielectric properties of the two insulating materials – paper and oil.

7. Influence of the measuring resistor

For short lengths of cables in very good condition a complication may arise. This is the case if the input resistance R_m of the measuring system is of the same size as the leakage resistance of the measured object, or – in terms of the equivalent circuit – comes into the region of values of the resistors R_1 and R_2. In this case, the influence of the additional resistor R_m cannot be neglected. The analysis shows that in this case the type of the return voltage curve indicated in Eq. (1) remains, but the time constants τ_1 and τ_2 are changed. Instead of τ_1 and τ_2, effective time constants τ_1' and τ_2' must be used and also different elements in the equivalent circuit.

The resistor R_m influences τ_1 and τ_2 but not U_s. The quantitative influence of this resistance can be calculated analytically. Equations (14)–(17) show the correlations

$$U_r(t) = U_s\left(\mathrm{e}^{-t/\tau_2'} - \mathrm{e}^{-t/\tau_1'}\right) \tag{14}$$

$$\begin{aligned} \tau_2' &= \left(\alpha - \sqrt{\alpha^2 - \beta}\right)^{-1} \\ \tau_1' &= \left(\alpha + \sqrt{\alpha^2 - \beta}\right)^{-1} \end{aligned} \tag{15}$$

$$\alpha = \frac{1}{2}\left[\frac{\tau_1(R_2 + R_m) + \tau_2(R_1 + R_m)}{\tau_1\tau_2 R_m}\right] \tag{16}$$

$$\beta = \frac{(R_1 + R_2 + R_m)}{\tau_1\tau_2 R_m} \tag{17}$$

with $\tau_1 = R_1C_1$ and $\tau_2 = R_2C_2$

8. Measurements in the field

In dependence on the actual structure of the distribution network, various lengths of cable segments are to be measured and hence the capacitance C_p and the resistance R_p of the measured cable sections are different.

In principle, the return voltage curve does not depend on the length of a measured cable, because every part of the cable contributes with a certain amount of current from the depolarization processes, whereby the current per length of the cable is constant. This current charges the cable and since the capacitance C_p of the measured cable is also proportional to its length, no dependence of the return voltage curve on the length of the cable should occur.

The measurement resistor R_m of the measurement system leads to a discharge of the cable capacitance C_p and hence may influence the real return voltage curve. A characteristic parameter to describe this influence is the time constant $\tau_m = C_pR_m$ of the system. If this time constant is significantly higher than the time t_m at which the maximum of the return voltage occurs, the influence of R_m can be neglected.

If the time constant $\tau_m = C_p R_m$ is in the same region or smaller than the time constants τ_1 and τ_2 in Figure 2 there is an influence of the measurement procedure on the experimentally found return voltage curve. It is obvious that the shorter the cable is, the more pronounced the influence of R_m may be. Hence the *p*-factor calculated from the return voltage curve may be higher as a consequence of the measurement resistor, thus indicating a higher degradation of the cable.

To evaluate the influence of the measurement resistor R_m, experiments were performed with cables of various lengths and with various measurement resistors. The results show that the explanation given is relevant. In one set of experiments, three

cores L1, L2 and L3 of a cable of 150 m long were measured with measuring resistors of 12 and 42 GΩ. In some measurements, two or three cores of the cable were measured in parallel, thus forming specimens with different lengths. The results are shown in Fig. 3. The curves from the three cores are very similar. The measurement of core L1 alone with 42 GΩ generates nearly the same curve as the measurement of L1 || L2 || L3 with 12 GΩ, a result that verifies the influence of the time constant $\tau_m = C_p R_m$. Cores L2 and L3 in parallel show a slightly higher return voltage curve. In this case even with a measurement resistor of 42 GΩ a small dependence on the length of the measured object exists.

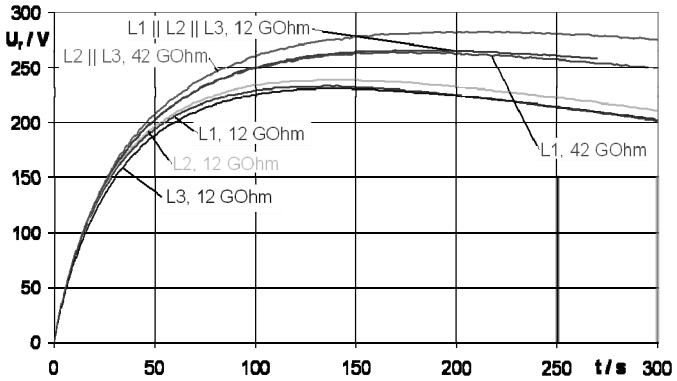

Fig. 3. Return voltage curves from measurements of three cores L1, L2 and L3 of a 150 m long cable (GA9) with various measuring resistors

Another set of measurements was performed with a cable 1300 m long. This cable was measured with resistors of 2 and 12 GΩ. Also in this case single cores or two or three cores in parallel were measured. The results are shown in Fig. 4. The dependence found is similar as the aforementioned.

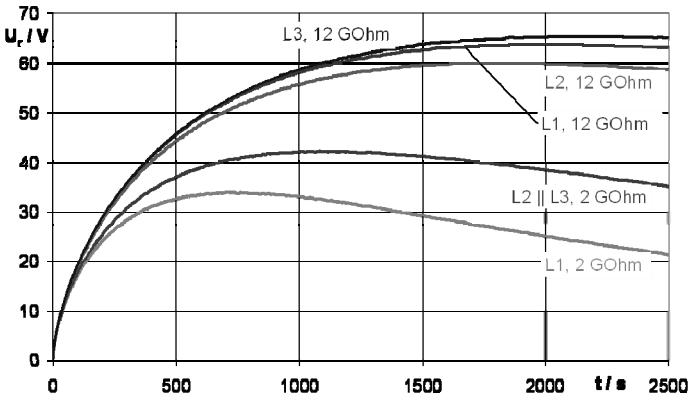

Fig. 4. Return voltage curves from measurements of three cores L1, L2 and L3 of a 1300 m long cable (TOR) with various measuring resistors

For another cable with the length of 330 m (HEI) measurements were performed using measuring resistors of 12 and 62 GΩ. Due to the influence of the measurement resistor, in the measurement with 12 GΩ a slightly higher *p*-factors were found.

The measurements with 62 GΩ showed no length dependence of the *p*-factors and the calculated dielectric time constants. The comparison of the measurements of L1, L1 || L2 and all three cores in parallel showed values that were to be expected with respect to the separate measurements of the three cores. Table 1 shows the *p*-factors and the dielectric time constants calculated from the aforementioned measurement data.

Table 1. *p*-Factors and electric permittivities for the measurements of cable HEI (3 cores of 330 m each) with various measuring resistors and for various circuits

12 GΩ	L1	L2	L3
U_m [*V*]	35.6	36.86	47.39
t_m [s]	312	331	325
s [V/s]	0.672	0.725	0.771
p	0.170	0.154	0.189
$\lg \tau_2$ [s]	4.24	4.50	4.01
$\lg \tau_1$ [s]	1.73	1.71	1.80
62 GΩ	L1	L2	L3
U_m [V]	33.0	38.2	60.5
t_m [s]	329	405	405
s [V [s]	0.671	0.759	0.892
p	0.150	0.124	0.167
$\lg \tau_2$ [s]	4.56	5.19	4.38
$\lg \tau_1$ [s]	1.70	1.70	1.84
62 GΩ	L1 || L2	L3	L1 || L2 || L3
U_m [V]	36.8	57.6	41.4
t_m [s]	371	417	373
s [V/s]	0.701	0.908	0.717
p	0.142	0.152	0.155
$\lg \tau_2$ [s]	4.77	4.63	4.53
$\lg \tau_1$ [s]	1.72	1.81	1.77

The time constants τ_1 were about 50 s in all cases. For the measurements of one, two or three cores with 62 GΩ no length dependence was found. The measurements of parallel circuits showed dielectric time constants compatible to the results of single measurements of the cores. Figure 5 shows the calculated dielectric time constants τ_1 and τ_2 for the measurements of different parallel circuits of the three cores with 62 GΩ.

Whether the measurement resistor R_m has an influence on the measured results depends on the 'quality' of the measured object. If the measurement resistor is significantly higher than the over all resistance R_p of the insulation of the measured cable

(including all splices, terminations, etc.) the return voltage curve is not significantly influenced.

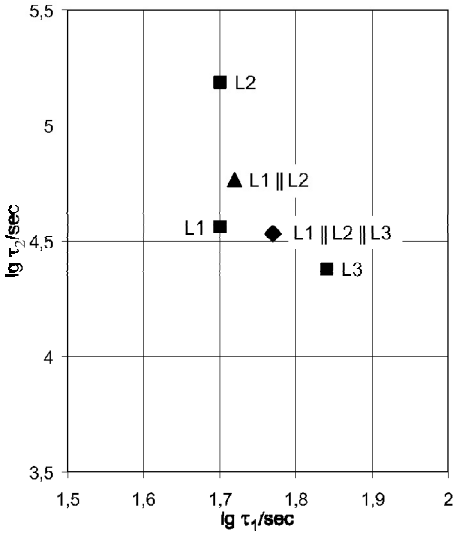

Fig. 5. Dielectric time constants τ_1 and τ_2 for the measurements with 62 GΩ (selection from Table 1)

In general shorter cable lengths tend to show higher *p*-factors and lower time constants τ_2, but this is not always the case. Different cables of similar lengths often show different *p*-factors and different time constants τ_2 thus allowing a relative ranking.

Measurements of cables in one utility showed no influence of the cable lengths at all. In this case, it showed up that the cables in general showed a high degree of degradation, so – even for low lengths of the cables – the inner resistances R_p of the cables were significantly smaller than the measuring resistor R_m.

9. Further experience from the field

Similar to other diagnostic methods, return voltage measurements in various seasons of the year may show different results. Figure 6 and Table 2 show the results from three measurements within 14 months. Compared to the measurement in winter, as a consequence of the higher temperature of the soil around the cable, the measurement in summer resulted in lower dielectric time constants for paper and oil. The second measurement in the cold season showed that no ageing had occurred, the dielectric time constants were the same as 14 months before.

The ageing processes in a cable in general lead to a decrease of the resistance of the cellulose. The same holds for an uptake of water in the cellulose, whereby water on one hand accelerates the degradation of the cellulose and on the other hand it also occurs as a degradation product. Thus ageing will result in a decrease of the time constant τ_2 of the cellulose. The time constant τ_1 of the oil will be influenced only to a less extent.

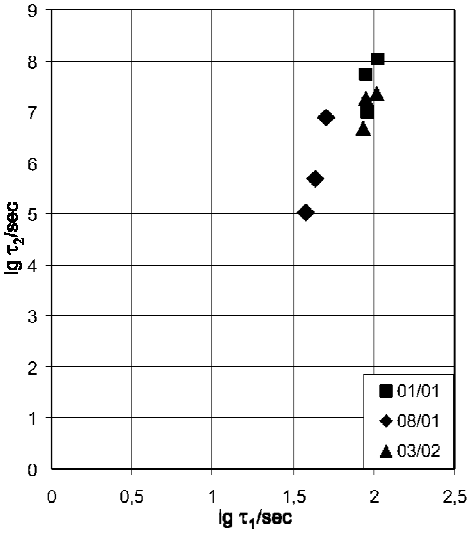

Fig. 6. Dielectric time constants for measurements of cable DYR in various seasons of the year (see Table 2)

Table 2. *p*-Factors and electric permittivities for various measurements of the three cores of cable DYR

	L1	L2	L3
1 January			
U_m [V]	171	192	167
t_m [s]	1178	1463	1052
s [V/s]	1.94	1.82	1.84
p	0.075	0.073	0.086
$\lg \tau_2$ [s]	7.74	8.03	7.01
$\lg \tau_1$ [s]	1.95	2.02	1.96
1 August			
U_m [V]	387	449	343
t_m [s]	403	606	302
s [V/s]	8.96	8.82	9.04
p	0.107	0.084	0.126
$\lg \tau_2$ [s]	5.68	6.88	5.03
$\lg \tau_1$ [s]	1.64	1.71	1.58
1 March			
U_m/V	197	220	181
t_m [s]	1087	1283	937
s [V/s]	2.22	2.10	2.10
p	0.082	0.082	0.092
$\lg \tau_2$ [s]	7.27	7.36	6.69
$\lg \tau_1$ [s]	1.95	2.02	1.94

The described ageing processes have been found also in practice. Figure 7 shows the results of two measurements of a cable in different seasons of the year. In this case

the first measurement was performed in summer. The measurement 6 months later expectedly showed higher time constants τ_1 of the oil. Interestingly the time constants τ_2 of the cellulose had decreased. The ageing of the cores during the time interval between the two measurements was different (see Table 3). The *p*-factors showed corresponding changes.

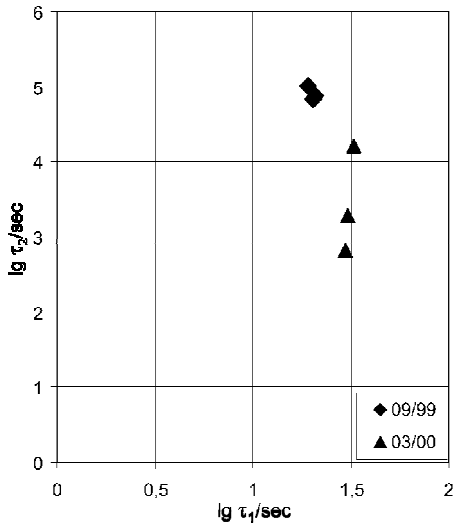

Fig. 7. Change of the dielectric time constants as a consequence of ageing during 6 months (Table 3)

Table 3. *p*-Factors and electric permittivities for the measurements of three cores of cable GER6 in various seasons of the year

	L1	L2	L3
September 1999			
U_m [V]	569	590	590
t_m [s]	165	165	171
s [V/s]	29.7	29.1	28.4
p	0.116	0.123	0.121
$\lg \tau_2$ [s]	5.02	4.83	4.89
$\lg \tau_1$ [s]	1.28	1.31	1.32
March 2000			
U_m [V]	306	273	370
t_m [s]	129	96	203
s [V/s]	10.7	10.7	11.5
p	0.222	0.266	0.159
$\lg \tau_2$ [s]	3.29	2.82	4.21
$\lg \tau_1$ [s]	1.49	1.47	1.51

In a set of measurements in one utility, the cables measured showed the general tendency that – for cables of lengths below a few hundred meters – the *p*-factors increased with decreasing lengths. But nevertheless even in this dataset, cables of nearly

identical lengths showed significantly different *p*-factors, indicating different degradations. Measurements of cables in another utility showed no influence of the cable lengths. For these cables with a higher degree of degradation the influence of the measuring resistor was not relevant even for lengths of about 100 m [12].

10. Summary

In dependence on the actual condition of a cable examined with the return voltage method the diagnostic result may be influenced by the actual length of the cable. The calculated *p*-factor of short cable lengths may be higher than representative for the degree of degradation, indicating a more severe degree of ageing. This influence can be overcome by the use of higher measuring resistors or by an appropriate correction of the measured data.

Based on the Maxwell model, an appropriate concept for the description of the phenomena that occur in a paper-oil insulation, return voltage curves can be used to calculate the dielectric time constants τ_1 and τ_2 of the two dielectrics oil and paper. Ageing and degradation of the insulation significantly reduces the time constant τ_2 of the cellulose.

References

[1] NÉMETH E., *Zerstörungsfreie Prüfung von Isolationen mit der Methode der Entlade- und Rückspannungen*, IWK'66, Ilmenau, Germany, 1966, 87–91.

[2] BOGNAR A., KALOCSAI L., CSEPES G., NÉMETH E., SCHMIDT J., *Diagnostic Tests of High Voltage Oil-Paper Insulating Systems (In Particular Transformer Insulation) using DC Dielectrometrics*, CIGRE '90, Paris, France, 1990, 15/33–08.

[3] NÉMETH E., *Practical experiences of diagnostic testing of power cable lines by the voltage-response method*, IWK '95, Ilmenau, Germany, 1995, 699–708.

[4] ZAENGL W.S., IEEE EI-Mag., 19, (2003), 5.

[5] ZAENGL W.S., IEEE EI-Mag., 19, (2003), 9.

[6] PATSCH R., BERTON F., KOUZMINE O., *The Influence of the Ambient Temperature on the Diagnostic Response of Paper-Oil Insulated Cables*, APTADM '01, Wroclaw, Poland, 2001, 34–37.

[7] HOUHANESSIAN V.D., *Measurement and Analysis of Dielectric Response in Oil-Paper Insulation Systems*, PhD-Thesis, ETH Zürich, Switzerland, 1998.

[8] ALEKSEEV B.A., Elektrichestvo, 2 (959), 58.

[9] PATSCH R., KOUZMINE O., WSEAS Trans. on Circuits and Systems, 9 (2005), 1191.

[10] PATSCH R., KOUZMINE O., *p-Factor, a Meaningful Parameter for the Evaluation of Return Voltage Measurements*, CEIDP '02, Cancun, Mexico, 2002, 906–909.

[11] PATSCH R., KOUZMINE O., *The Influence of Climatic Conditions on the Diagnostic Results of Return Voltage Measurements*, ISEI'02, Boston, USA, 2002, 191–419.

[12] PATSCH R., KOUZMINE O., *Return Voltage Measurements – a good Tool for the Diagnosis of Paper-Oil-Insulations*, IEEE PowerTech, St. Petersburg, Russia, 2005, CD.

Received 29 May 2007
Revised 21 August 2007

Materials Science-Poland, *Vol. 27*, *No. 4/2*, *2009*

Nanoscale evaluation of thin oxide film homogeneity with combined shear force emission microscope

A. SIKORA[1*], T. GOTSZALK[2], R. SZELOCH[2]

[1]Electrotechnical Institute, Division of Electrotechnology and Materials Science

[2]Wrocław University of Technology, Faculty of Microsystem Electronics and Photonics

Very fast development of large scale integrated circuits causes downsizing of the structures. Due to this fact, the thickness of oxide layer in the gate area decreases as well. In order to perform test of dielectric layer with nanometer resolution in a lateral plane, one can use AFM with a conductive tip. Biased tips can be used to measure current flow to the surface of the sample in order estimate its electrical properties. In the paper a modular shear force emission microscope has been presented. A metallic scanning microtip is used as a nano e-beam and it allows one to measure the local surface emission and investigate the quality of dielectric layers in semiconductor chips.

Key words: *AFM; field emission; shear force microscopy; gate oxide tests*

1. Introduction

The progress of downscaling of the integrated circuits continues as a result of increasing the performance and reducing the power consumption. More than four decades ago this progress was predicted by Moore [1] although it was expected to last about ten years. Today one can still observe new achievements of semiconductor's technology when new generations of integrated circuits are released. It should be emphasized, that once this level was reached – the engineers must face specific issues and in order to solve problems, they need very sophisticated tools.

One of the important components of the MOS transistor is the dielectric layer, which isolates the gate and the channel. Its thickness obtained level of few nanometers or even 1.2 nm [2] in experimental chips. Theoretically it can be reduced down to 0.8 nm [3]. Silicon dioxide layers are fabricated by oxidation the silicon surface. This process is known and developed very well. It is however very difficult to obtain such thin layer and avoiding presence of defects which could make the structure useless. The fabrication process if not adjusted properly can lead to appearance of undesired

[*]Corresponding author, e-mail: sikora@iel.wroc.pl

objects like pinholes or even larger conductive spots. Thereby one must very carefully investigate the quality of oxide layer in order to optimize the production process and perform the tests of developed structures during mass production.

The oxide quality and reliability is essential when the lifetime of the integrated circuit is considered. Thereby this issue was investigated [4] as well as the methods of diagnosing the ultrathin oxide layers [5, 6]. One of the tools which allows investigation of the surface with nanometer resolution is atomic force microscopy (AFM). This method was developed by Binnig et al. [7]. The idea of AFM methods has been developed, and several scanning methods are now available in order to investigate various parameters of the surface. By using conductive tip and biasing the sample, one can measure the topography and current flow between the tip and sample. This allows to investigate electrical properties of the surface [8–14]. Such methods unlike in macroscopic measurement techniques can deliver much more valuable information about the oxide layer homogeneity and continuity. The application of the AFM scanning tip to diagnose the oxide layer was already successfully attended [15, 16]. Although generally very small force is applied to the tip in order to observe tip–sample interaction, sharp tip can damage very thin layer during the scanning process. Thereby non-contact methods can reduce significantly the risk of damaging the surface. Moreover, the wear of the tip changes the electrical filed around the tip and the measurement conditions can become unstable.

2. Experimental setup

The experiments were performed with a home-built setup. Its simplified scheme is shown in Fig. 1. As a scanning tip, the tungsten wire with diameter 120 μm was used. After electrochemical etching the obtained curvature radius of the tip was about 30 nm.

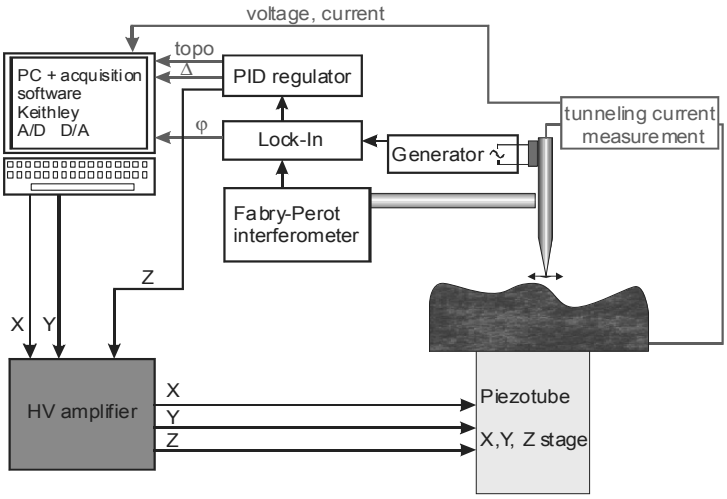

Fig. 1. A simplified diagram of the combined shear force emission microscope setup

In a shear force microscope, the tip oscillates laterally to the surface near one of its mechanical resonant frequencies. At a distance of a few nanometers from the surface in question, oscillations become damped out by shear forces (Fig. 2). This is used for tip–sample distance regulation as a basis for high resolution topographic imaging. In order to measure the microtip oscillation, a fibre Fabry–Perot interferometer is used. An advantage of this system is that quantitative measurements of tip vibration amplitude are easily performed.

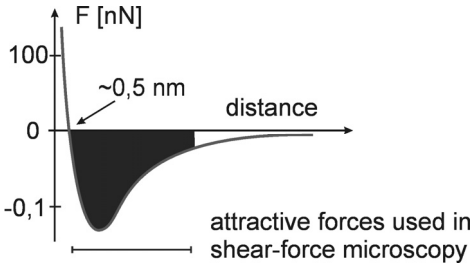

Fig. 2. Tip-sample force distribution curve. The vertical scale is distorted in order to show both attractive and repulsive forces

Moreover, the optical detection system allows one to apply voltage to the conductive microtip. In this case, the microtip can be used as an electron beam (e-beam), as a collector of field emission current flowing between the tip and surface. The small amount of force acting between the tip and a sample increases the lifetime of the tip and reduces the risk of the tip and sample damaging.

At the wire length varying from 5 to 7 mm, and when the spring constant is in the range from 1 N/m up to 3 N/m, the resonance frequency is about 12 kHz and a typical Q factor of the resonance is 100–200. Tungsten tips are commonly used in STMs due to convenient etching technology and well known work function.

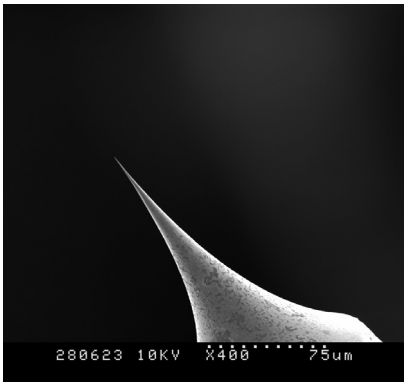

Fig. 3. The SEM photograph of electrochemically etched tungsten scanning tip used in the setup. The diameter of tungsten wire is 120 μm

The tip oscillation amplitude was measured with a single mode fibre Fabry–Perot interferometer. The face of the fibre was placed in the distance of several hundreds of micrometers from the tip, which reflected light beam back to the fibre. The main part of the interferometer was placed outside the measurement chamber and therefore stable environmental conditions for the laser and detector were provided. The interfer-

ometric signal detected by a lock-in voltmeter allowed the measurement of the tip oscillation amplitude and to use it as the tip–sample distance indicator. As the tip approaches the surface, the oscillation amplitude decreases and a phase shift appears.

During the experiments, the setpoint value was about 90% of the free oscillation amplitude, which correlates with the tip–sample distance of about 10 nm. The detailed description of the interferometric detection setup has been published elsewhere [17, 18]. This solution allowed one to obtain a quantitative measurement with very high sensitivity.

When the biasing tip–sample voltage is applied, the setup allows taking measurements in two modes: simultaneous surface topography and emission current (Fig. 4), and the voltage-current curve measured in a specific spot over the surface.

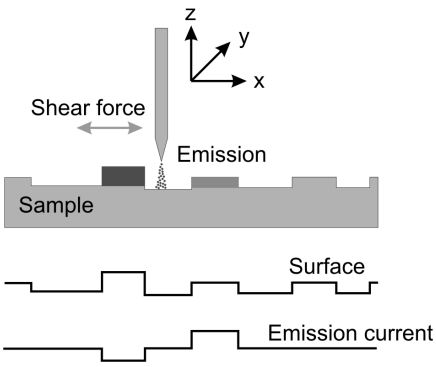

Fig. 4. The idea of simultaneous investigation of the topography and properties of the electrical surface with the combined shear force emission microscope setup

The field emission appears when electrical field causes deformation of potential barrier and electrons can leave the surface due to their high energy. This phenomena is also called the Fowler–Nordheim tunnelling [18], and can be described as follows:

$$I \approx A \frac{CE^2}{\varphi \cdot t^2(y)} \exp\left\{-\frac{B\phi^{3/2} v(y)}{E}\right\} \tag{1}$$

where A is the emitter surface area, E is the applied electric field, ϕ is the work function of the metal, B and C are constants, $v(y)$ as well as $t(y)$ are functions which arise due to the inclusion of image charge effects. The emission current depends on work function of the surface when other parameters are constant.

The energy necessary to obtain field emission phenomena is achieved as the result of a very small tip–sample distance. By the typical distance between 10 and 15 nm and the applied tip–sample voltage just about few volts – the electric field can reach level of tens of MV/m. It is must be mentioned that the real distance between the tip and conducting bulk can be bigger than the approach curve could indicate, due to presence of water film on the surface and thin oxide layer (oxidation process can appear naturally, when the clean metallic surface is exposed to the humidity, and as result the surface is covered by thin oxide layer). Thereby a real electric field can be smaller

than the estimated one, nevertheless it is still sufficient to obtain emission current from the surface which was confirmed experimentally.

According to the presented equation, when the all factors are constant, the value of current will vary, when the tip moves over the areas made of different materials (different values of work function).

3. Results

In order to demonstrate the efficiency of the method, some tests were performed. Presented examples were obtained by simultaneous measurement of the surface topography and the emission current. The first example shows a two metal sample: alumina structures deposited on chromium substrate by magnetron sputtering. The topography is shown in Fig. 5. The edge of the structure is visible clearly as well as relatively rough surfaces of chromium and alumina. Also, the side of the structure is visible due to sample tilt. It allows one to recognize the structure and the substrate very clearly.

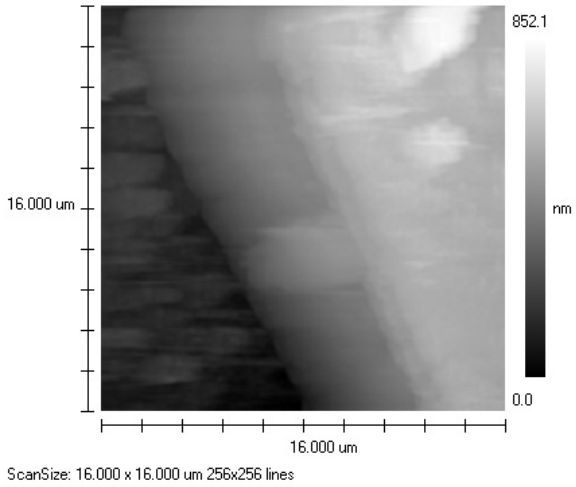

Fig. 5. The surface picture recorded
on alumina deposited on chromium substrate

On the emission picture (Fig. 6), one can see the emission area which is correlated to the chromium surface but no emission was recorded over the alumina surface. The result is connected probably to the relatively thick native alumina oxide layer which makes the emission very weak in this measurement conditions. Increase of the voltage could allow one to obtain the emission current through the alumina oxide but the risk of overload the current–voltage converter during the chromium area emission measurement should be taken into account. This problem can be solved by applying logarithmic current–voltage converter instead of the linear one. It can allow one to meas-

ure the current up to eight orders of magnitude which should be a satisfying solution in this case.

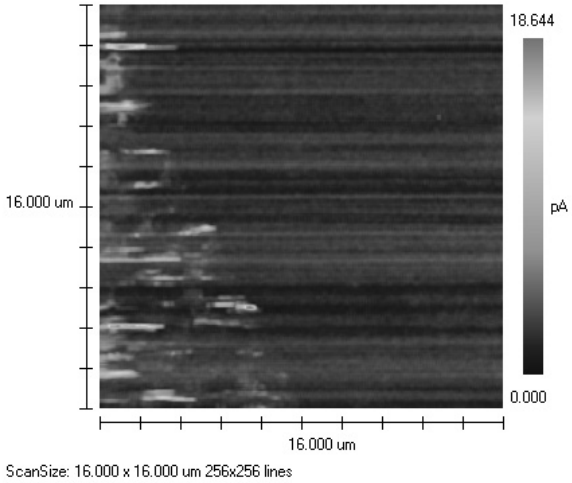

Fig. 6. The emission picture recorded on alumina deposited on chromium (tip–sample voltage – 11 V)

Next example shows a silicon sample covered with a native oxide layer (Fig. 7). Such layers are usually ca. 1 nm thick. This surface is very flat, without major features or structures. At a closer look, one can note few black points which can be easily overlooked, but even noticed, can be ignored as insignificant artefacts connected to the noise presence during the measurement.

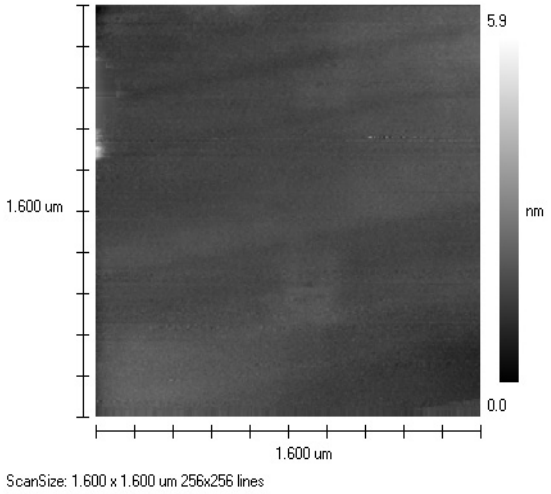

Fig. 7. The surface picture recorded on a silicon sample

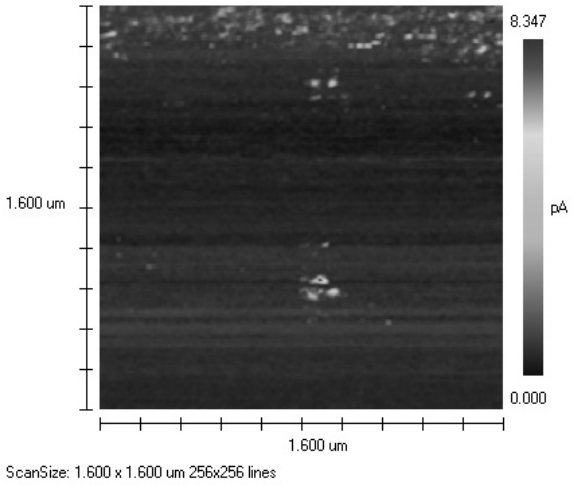

Fig. 8. The emission picture recorded
on a silicon sample (tip–sample voltage – 5 V)

The current emission map shows the correlation between black spots on the topography picture and significantly increased emission areas (Fig. 8). This picture shows weak points of the oxide layer, where the potential barer is smaller than the other places and current flows easier. An additional measurement of the topography in those areas should be the performed in order to investigate more closely the conductive spots.

4. Summary

The modular shear force emission microscope has been presented. It can be used for diagnostics of thin dielectric layers. Such layers are used not only in semiconductor industry but they are utilized generally in wide spectra of industrial production. In this case, however, the quality and continuity of the dielectric layer in submicrometer scale is crucial. Thereby this method can applied in other research issues as well.

One should be aware of possible difficulties. Some surfaces can be covered relatively quickly by native oxide when left in ambient conditions. This issue must be taken into account when the measurement is planned. This problem can be solved by performing the measurements in vacuum, but that causes major increase of costs. Moreover some processes cannot be performed in vacuum and another solution must be developed in such cases.

The main advantage of presented method is a non-contact measurement which allows providing the long life of the tips. Moreover, electrochemically etched tungsten tips are much cheaper than silicon cantilevers with metal covered tips and very good known work function of the tungsten is always valid. Thereby one can always measure

with confidence. In silicon cantilevers, the metal coating can be removed from the tip due to wear and the results can be no longer reliable.

Presented results proved efficiency of the method, however further research and tests are necessary in order to develop the method and the setup as well. In addition, the measurement conditions, sample preparation procedure, and its impact on the result should be carefully investigated.

References

[1] MOORE G.E., Electronics 38 (1965), 114.
[2] BOHR M., Intel Unveils, Intel's 90 nm Technology: Moore's Law and More, Intel 2002.
[3] HIROSE M., KOH M., MIZUBAYASHI W., MURAKAMI H., SHIBAHARA K., MIYAZAKI S., Semicond. Sci. Technol., 15 (2000), 485.
[4] WU E.Y., STATHIS J.H., HAN L.K., Semicond. Sci. Technol., 15 (2000), 425.
[5] YU Y.J., GUO Q., ZENG X., LI H., LIU S.H., ZOU S.C., Semicond. Sci. Technol., 20 (2005), 1116.
[6] JIE B.B., LO K.F., QUEK E., CHU S., SAH C.T., Semicond. Sci. Technol., 19 (2004), 870.
[7] BINNIG G., QUATE C.F., GERBER CH., Phys. Rev. Lett., 56 (1986), 930.
[8] O'BOYLE M.P., HWANG T.T., WICKRAMASINGHE H.K., Appl. Phys. Lett., 74 (1999), 2641.
[9] WATERS R., VAN ZEGHBROECK B., Appl. Phys. Lett., 73 (1998), 3692.
[10] HASSANIEN A., TOKUMOTO M., KUMAZAWA Y., KATAURA H., MANIWA Y., SUZUKI S., ACHIBA Y., Appl. Phys. Lett., 73 (1998), 3839.
[11] RADNOCZI G., SAFRAN G., KOVACS I., GESZTI O., BIRO L., Acta Phys. Slov., 50 (2000), 679.
[12] JIA J.F., INOUE K., HASEGAWA Y., YANG W.S., SAKURAI T., J. Vac. Sci. Technol. B, 15 (1997), 1861.
[13] ICHIZLI V., HARTNAGEL H.L., MIMURA H., SHIMAWAKI H., YOKOO K., Appl. Phys. Lett., 79 (2001), 4016.
[14] VAN DER WEIDE D.W., NEUZIL P., J. Vac. Sci. Technol. B, 14 (1996), 4144.
[15] PORTI M., BLASCO X., NAFRÍA M., AYMERICH X., Nanotechnology 14 (2003), 584.
[16] LAURITSEN J.P., FOSTER A.S., OLESEN G.H., CHRISTENSEN M.C., KÜHNLE A., HELVEG S., ROSTRUP -NIELSEN J.R., CLAUSEN B.S., REICHLING M., BESENBACHER F., Nanotechnology, 17 (2006), 3436.
[17] SIKORA A., GOTSZALK T., SZELOCH R., *Combined shear force – tunnelling microscope with interferometric tip oscillation detection for local surface investigation and oxidation*, [In:] G. Wilkening, L. Koenders (Eds.), *Nanoscale Calibration Standards and Methods*, VCH, Berlin 2005, 144.
[18] SIKORA A., GOTSZALK T., SZELOCH R., Microel. Eng., 84 (2007), 542.
[19] FOWLER R.H., NORDHEIM L., Proc. Roy. Soc. London, A119, (1928), 173.

Received 28 June 2007
Revised 26 March 2008

Materials Science-Poland, *Vol. 27*, *No. 4/2*, *2009*

Broadband dielectric spectroscopy of $Al/Lu_2O_3/Al$ thin film sandwiches

T. WIKTORCZYK*

Institute of Physics, Wrocław University of Technology,
Wybrzeże Wyspiańskiego 27, 50-370 Wrocław, Poland

The paper focuses on the dielectric characterization of electron beam deposited lutetium oxide thin films sandwiched between aluminium electrodes. The complex capacitance characteristics were recorded in the frequency domain (from 10 μHz to 10 MHz) with a dielectric response analyser. The influence of the temperature, the insulator thickness and sample ageing on $C'(\omega)$ and $C''(\omega)$ characteristics was examined. It was shown that high frequency/low temperature dielectric data are assigned to the volume of lutetium oxide film, whereas the low frequency/high temperature results are connected with M/I interfaces. The width of near electrode regions (Schottky barriers) was estimated ($\lambda \approx 2.6$–4.7 nm).

Key words: *lutetium oxide; thin films; dielectric properties; MIM structures; rare earth oxides*

1. Introduction

In the last decade, thin films of rare earth oxides (REO) have attracted great attention due to their applications in modern electronics and optoelectronics [1–12]. The REO thin films, known as high-dielectric constant materials, exhibit excellent physical and chemical stability. They have large bandgap (4–6 eV) and high relative dielectric permittivity (10–20). The REO films exhibit good insulating properties and high dielectric breakdown field strength (>1 MV/cm). These properties make them interesting dielectric materials for various microcircuits such as field effect transistors (CMOS type structures), thin film capacitors (MIM type structures), miniaturized capacitors in DRAMs, etc.

The paper is focused on dielectric properties of lutetium sesquioxide films (Lu_2O_3). Recently, Lu_2O_3 films have been extensively examined [10–17]. At normal pressure, Lu_2O_3 exhibits cubic bixbyite type structure (C-type structure) with the lattice constant of 1.0391 nm [4]. Lu_2O_3 exhibits the largest bandgap (5.5 eV) [13], the

*E-mail: tadeusz.wiktorczyk@pwr.wroc.pl

highest lattice energy (–13.871 kJ/mol) [14] and the highest melting point (2467 °C) [13] among lanthanide oxides. Lu_2O_3 films are transparent in the visible and NIR spectral range [13]. Their refractive index is about 1.84 [13].

Lu_2O_3 thin films have been fabricated by various methods such as: sol-gel method [10–11], electron beam deposition (E-B) [12–13], pulsed laser deposition (PLD) [14] and atomic layer deposition (ALD) [15]. In this paper Lu_2O_3 films have been prepared by physical vapour deposition (PVD). An E-B gun was used as Lu_2O_3 evaporation source.

The aim of this paper is application of the broadband dielectric spectroscopy (in the frequency range from 10 μHz to 10 MHz) for examination and dielectric characterization of $Al/Lu_2O_3/Al$ thin film sandwiches.

2. Dielectric properties of MIM structures

The dielectric properties of any MIM structure can be described by the complex capacitance in a parallel representation:

$$C^*(\omega) = C'(\omega) - jC''(\omega) = C_p(\omega) - \frac{jG_p(\omega)}{\omega} \tag{1}$$

where: $G_p(\omega)$ and $C_p(\omega)$ are total conductance and capacitance of a specimen at the circular frequency ω ($\omega = 2\pi f$), respectively.

For parallel-plate configuration of the sample geometrical capacitance is expressed as:

$$C_0 = \varepsilon_0 s d^{-1} \tag{2}$$

where: ε_0 is the dielectric permittivity of a free space, s is the sample surface area and d its thickness.

The material properties are characterized by complex dielectric permittivity, $\varepsilon^*(\omega)$, which is related to $C^*(\omega)$ by a geometrical factor C_0:

$$\varepsilon^*(\omega) = \frac{C^*\omega)}{C_0} = \varepsilon'(\omega) - j\varepsilon''(\omega) \tag{3}$$

We have also applied the complex impedance diagnostic for the analysis of $Al/Lu_2O_3/Al$ thin film structures. The complex impedance of a specimen is defined in the following way:

$$Z^*(\omega) = Z'(\omega) - jZ''(\omega) = R_s(\omega) - \frac{j}{\omega C_s(\omega)} \tag{4}$$

where $R_s(\omega)$ and $C_s(\omega)$ are series resistance and capacitance of a specimen, respectively.

3. Experimental details

Al/Lu_2O_3/Al thin film capacitors were prepared on quartz substrates by the PVD method. The surface areas of the specimens were in the range 0.8–1.2 mm^2. Sample thicknesses ranged from 0.2 μm to 0.6 μm. All dielectric measurements were carried out in the frequency range 10^{-5}–10^6 Hz by means of an Alpha type Novocontrol frequency response analyser at a low voltage signal (U_{ac} = 100 mV). The measurements were performed at ambient conditions. Before measurements, the specimens were thermally annealed at 500 K for 24 h. More experimental details may be found elsewhere [13, 16].

4. Experimental results

4.1. Capacitance characteristics at various temperatures

Frequency dependent capacitance characteristics for Al/Lu_2O_3/Al structures measured at various temperatures are presented in Figs. 1 and 2. Figure 1 shows $C'(f)$ characteristics whereas Fig. 2 presents $C''(f)$ characteristics.

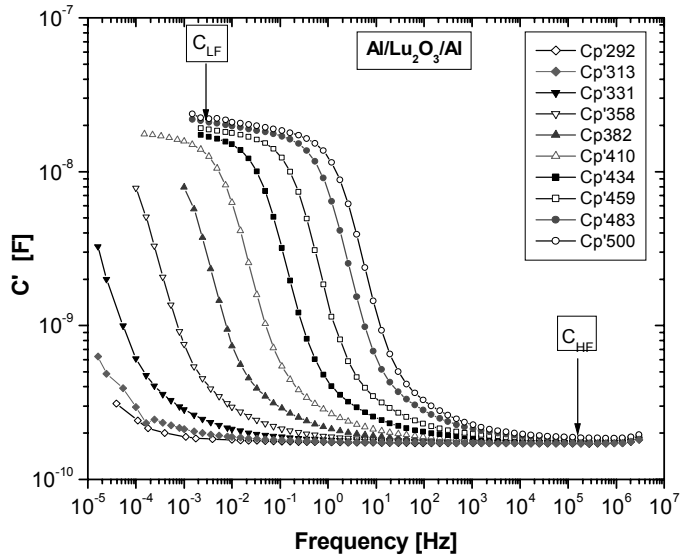

Fig. 1. Frequency dependence of the real part of the capacitance of Al/Lu_2O_3/Al structures at various temperatures. Film thickness: 546 ±2.5 nm, sample surface area: 0.95 ±0.02 mm^2

High frequency parts of all $C'(f)$ curves (denoted as C_{HF}) are almost flat, showing a weak dependence on temperature. For low frequencies, $C'(f)$ characteristics rapidly increases until they become saturated, reaching values of C_{LF}.

Curves of the imaginary part of the capacitance in Fig. 2 show distinct loss peaks, the half widths of which amount almost 1.5 decades in the frequency scale. The C″(f) maxima are thermally activated according to the relation:

$$f_{C''_{\max}} = f_0 \exp\left(\frac{E_a}{kT}\right)$$

in which: f_0 is a constant, E_a – the activation energy, k – the Boltzmann constant and T – temperature. From log(C''_{max}) plot vs. inverse temperature, the activation energy of C''_{max} was estimated. Taking into account the slope of this curve (not shown here), the activation energy was found to be 1.08 ±0.02 eV.

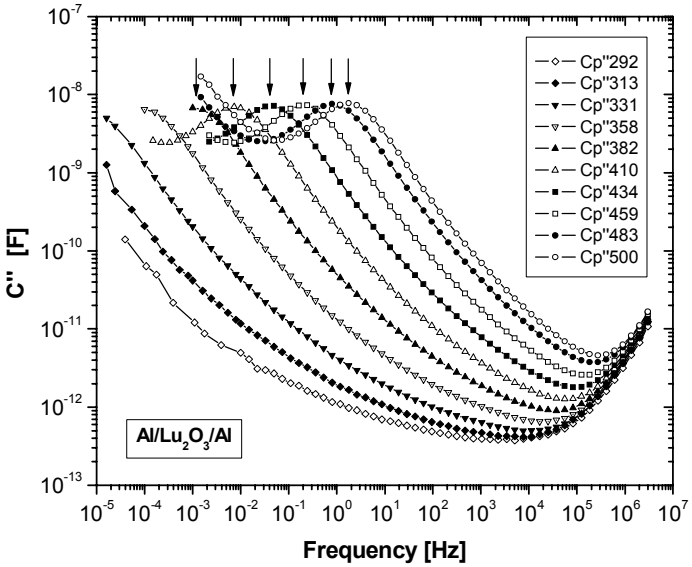

Fig. 2. Frequency dependence of the imaginary part of the capacitance of Al/Lu_2O_3/Al structures at various temperatures. Film thickness: 546 ±2.5 nm, sample surface area: 0.95 ±0.02 mm^2

A marked increase in C″(f) curves for the r.f. range is observed at all temperatures. Such an effect for Al/Lu_2O_3/Al structures can be explained as due to combined lead and contact resistances for high frequencies.

4.2. Insulator thickness

In Figure 3, dispersion characteristics of the real part of the capacitances of three samples of different Lu_2O_3 film thickness measured at 410 K are shown. It is seen that the capacitance is thickness dependent for high frequencies (f > 0.1 Hz). Dielectric permittivity in this range has values from 11 to 13, being close to the bulk dielectric permittivity of Lu_2O_3 itself [13]. For frequencies below 1 MHz, the capacitance (C_{LF}) becomes thickness independent in the saturation region.

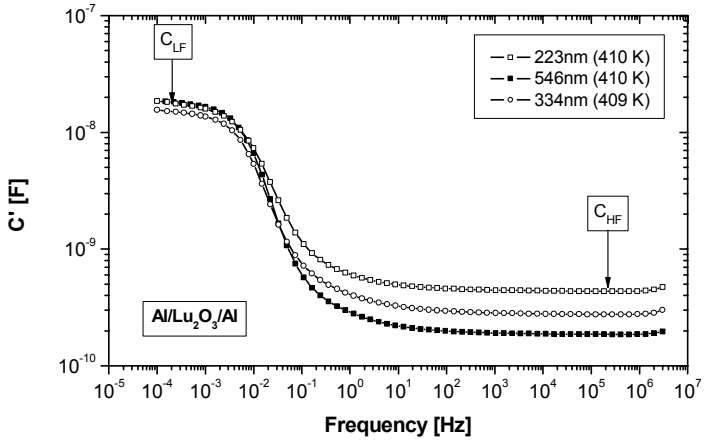

Fig. 3. Frequency dependence of C' at 410 K for Al/Lu_2O_3/Al structures with various insulator thicknesses. The capacitance was normalized for the sample surface area of 1 mm^2

Values of ε' estimated for various temperatures in this range (10^2–10^3) were thickness dependent and have to be taken as apparent values for Al/Lu_2O_3/Al structure. The high- and low-frequency capacitances (C_{HF} and C_{LF}) determined from $C'(f)$ curves at various temperatures have been compiled in Tables 1 and 2 where the values of the ratio C_{LF}/C_{HF} have also been given.

4.3. Ageing of Al/Lu_2O_3/Al structures

Figures 4 and 5 show frequency dependences of C' and C″ for aged samples. at dc electrical field at $U = 5$ V for 24 h. The ageing was carried out at 483 K.

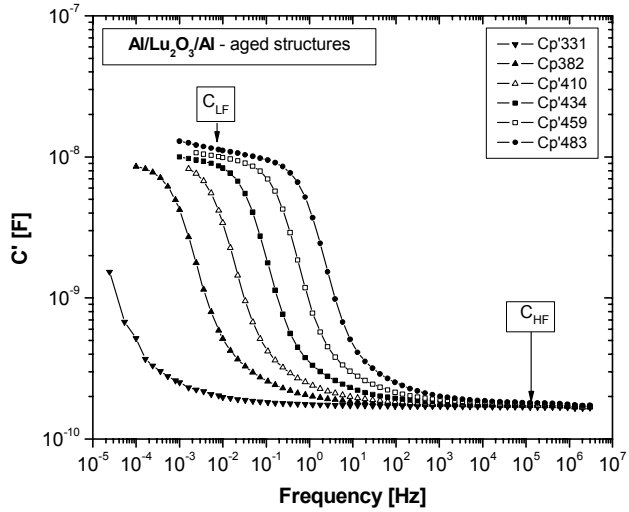

Fig. 4. Frequency dependences of C' for aged Al/Lu_2O_3/Al structures. Lu_2O_3 film thickness 546 ±2.5 nm, sample surface area 0.95 ±0.02 mm^2

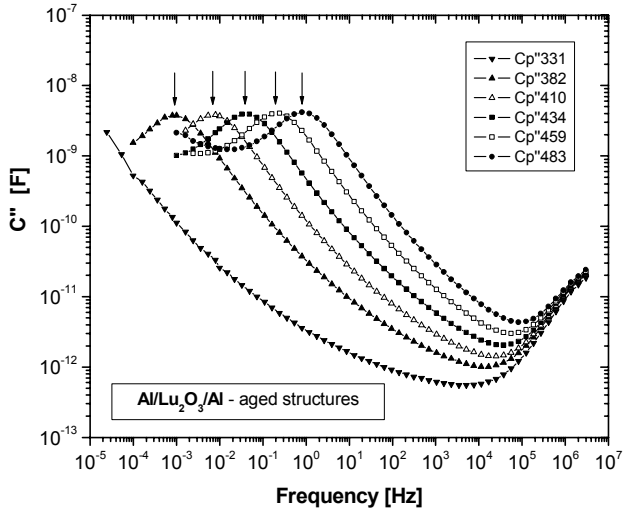

Fig. 5. Frequency dependence of C″ for aged $Al/Lu_2O_3/Al$ structures. Lu_2O_3 – film thickness: 546 ±2.5 nm, sample surface area: 0.95 ±0.02mm^2

C′ and *C″* characteristics in Figs. 4 and 5 exhibit frequency dependences similar to those presented in Figs. 1 and 2. However, sample ageing causes important reduction of the low-frequency real part of the capacitance (C_{LF}). The activation energy for temperature shift of C_{fmax} was found to be 1.11±0.02 eV.

5. Discussion

The results of dielectric measurements of $Al/Lu_2O_3/Al$ structures suggest that observed dielectric response comes from Al/Lu_2O_3 and Al/Lu_2O_3 near-electrode regions and from Lu_2O_3 film. We have assumed that Schottky barriers are formed at both metal/insulator boundaries [17, 18]. Figure 6 shows the energy diagram for examined $Al/Lu_2O_3/Al$ structures. The capacitance and the resistance of Lu_2O_3 film can be expressed in the following way:

$$C_v = \varepsilon_0 \varepsilon'_V \frac{s}{d} \tag{5}$$

$$R_V = R_0 \exp\left(\frac{E_V}{kT}\right) \tag{6}$$

where ε'_v denotes the dielectric permittivity of Lu_2O_3 film and E_v is its activation energy. From Figures 1 and 2 the values of the high frequency capacitance ($C_{HF} \approx C_v$) for annealed samples and for samples aged have been determined (Table 1). In the the

table, the values of R_v determined from the impedance plots (not shown here) are also given obtained by transformation the dielectric data according to Eq. (4).

Table 1. The parameters of the insulating film (Lu_2O_3) estimated in this paper

T [K]	Structures annealed at 500 K		Structures aged at 5 V	
	$C_{HF} \approx C_v$ [pF]	R_v [Ω]	$C_{HF} \approx C_v$ [pF]	R_v [Ω]
292	170.6	–		
313	171.5	5.6×10^{12}		
331	172.9	1.1×10^{12}	169.1	
358	173.8	9.5×10^{10}	–	
382	173.8	8×10^{9}	172	1.8×10^{9}
410	177.5	1×10^{9}	173.2	2.1×10^{9}
434	179.2	1.8×10^{8}	175.2	3.3×10^{8}
459	181.3	4.5×10^{7}	177.3	6.3×10^{7}
483	183.8	9×10^{6}	179.8	1.7×10^{7}
500	185.1	4.2×10^{6}		

Table 2. The parameters of the near electrode regions for Al/Lu_2O_3/Al structures estimated in this paper

T [K]	Structures annealed at 500 K			Structures aged at 5 V		
	C_{LF} [nF]	C_{LF}/C_{HF}	$C_{B1(2)}$ [nF]	C_{LF} [nF]	C_{LF}/C_{HF}	$C_{B1(2)}$ [nF]
382				9.7	56.4	19.4
410	18.5	105	37.0	9.9	57.2	19.8
434	18.8	105	37.6	10.1	57.6	20.2
459	19.2	106	39.0	10.3	58.1	20.6
483	19.5	106	39.0	10.7	59.5	21.4
500	20.0	108	40.0			

The capacitance of the depletion regions connected with Schottky barriers can be expressed by:

$$C_{b1(2)} = \varepsilon_0 \cdot \varepsilon'_{b1(2)} \frac{s}{\lambda_{1(2)}} \tag{7}$$

where $\varepsilon'_{b1(2)}$ denotes the dielectric permittivity of the near-electrode regions and $\lambda_{l(2)}$ is the thickness of these regions.

Assuming that both near-electrode regions exhibit the same properties, we get: $\varepsilon'_{b1} \approx \varepsilon'_{b2} = {}'_{b1(2)}$, $\lambda_1 \approx \lambda_2 = \lambda$ and $C_{b1} \approx C_{b2} = C_{b1(2)}$. Moreover, if $\varepsilon'_{b1(2)} \approx \varepsilon'_v = \varepsilon'(Lu_2O_3) = 11.5$, then for low frequency/high temperature approximation we get: $C_{LF} \approx ½C_{b1(2)}$.

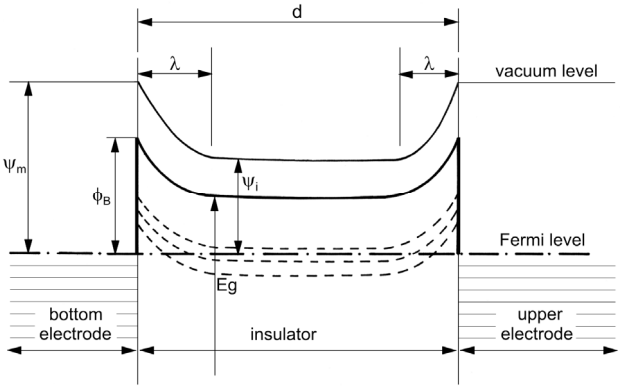

Fig. 6. Energy diagram of MIM structure having two Schottky barriers at M/I interfaces

For high frequency/low temperature approximation: $C_{HF} \approx C_v$. Taking into account the average values of $C_{b1(2)}$ equal to 9.6 nF and 5.07 nF for structures annealed and aged, respectively (see Table 2), the thickness of near electrode regions was determined from Eqs. (5) and (7). We obtained: $\lambda \approx 2.6$ nm for Al/Lu_2O_3/Al structures and $\lambda \approx 4.7$ nm for aged structures.

6. Concluding remarks

We have employed broadband dielectric spectroscopy for measurements in Al/Lu_2O_3/Al thin film structures. Experimental data for frequencies from 10 μHz to 10 MHz enable better understanding of dielectric properties of Al/Lu_2O_3/Al structure. We have shown that dielectric response of such a structure comes from the bulk of Lu_2O_3 film and from both metal/Lu_2O_3 interfaces. The parameters of Lu_2O_3 film and near electrode regions (Schottky barriers) have been determined.

References

[1] LESKELÄ M., KUKLI K., RITALA M., J. Alloys Comp., 418 (2006), 27.
[2] KWON K.-H., YANG J.-K., PARK H.-H., KIM J., ROH T.M., Appl. Surface Sci., 252 (2006), 7624.
[3] DURAND C., VALLÉE C., DUBORDIEU C., KAHN M., DERIVAZ M., BLONKOWSKI S., JALABERT D., HOLLINGER P., FAHG Q., BOYD I.W., J. Vac., Sci. Technol., 34 (2006), 459.
[4] DAKHEL A.A., J. Alloys Compd., 422 (2006), 1.
[5] KIM Y., MIYAUCHI K., OHMI S., TSUTSUI K., IWAI H., Miroelectronics J., 36 (2005), 41.
[6] NIINISTÖ L., PÄIVÄSAARI J., NIINISTÖ J., PUTKONEN M., NIEMINEN M., Phys. Stat. Sol. (a) 201 (2004), 1443.
[7] EVANGELOU E.K., MAVROU G., DIMOULAS A., KONOFAOS N., Sol. State Electron., 51 (2007), 164.
[8] SINGH M.P., SHIVASHANKAR S.A., J. Cryst. Growth, 276 (2005), 148.
[9] SCHAMM S., SCAREL G. FANCIULLI M., Topics in Appl. Phys., 106 (2007), 153.
[10] GARCIA-MURILLO A., LE LUYER C., PEDRINI C., MUGNIER J., J. Alloys Compd., 323–324 (2001), 74.
[11] GUO H., YIN M., DONG N., XU M., LOU L., ZHANG W., Appl. Surf. Sci., 243 (2005), 245.

[12] OHMI S., TAKEDA M., J. Electrochem. Soc., 151 (2004), G279.
[13] WIKTORCZYK T., Opt. Appl., 31 (2001), 83.
[14] DARMAWAN P., Sol. State Comm., 138 (2006), 571.
[15] SCAREL G., BONERA E., WIEMER C., TALLARIDA G., SPIGA S., FANCIULLI M., FEDUSHKIN I. L., SCHUMANN H., LEBEDINSKII YU., ZENKEVICH A., Appl. Phys. Lett., 85 (2004), 630.
[16] WIKTORCZYK T., J. Non-Cryst. Sol., 351 (2005), 2853.
[17] WIKTORCZYK T., Pys. Stat. Sol., 139 (1993), 397.
[18] NADKARNI G.S., SIMMONS J.G., J. Appl. Phys., 47 (1976), 114.

Received 25 May 2007
Revised 17 August 2007

Materials Science-Poland, *Vol. 27*, *No. 4/2*, *2009*

Space charge decay in low density polyethylene –montmorillonite clay multilayer nanocomposites

T. KRAUSE[1], L. MOROŃ[2], E. MOTYL[3], P. ŻYŁKA[*3]

[1]Alstom Power Sp. z o.o., Wrocław Branch, Poland

[2]Electrotechnical Institute, Division of Electrotechnology and Materials Science, Wrocław, Poland

[3]Wroclaw University of Technology, Institute of Electrical Engineering Fundamentals (I-7), Poland

The space charge accumulation and decay at low density polyethylene (LDPE)/(LDPE– montmorillonite (MMT) nanofiller composite) interfaces were investigated using the step electroacoustic (SEA) method. A three-layered specimen was polarized under dc voltage at 90 °C. After cooling under field, the short circuit currents as well as SEA signals were measured during TS discharging of the sample. The MMT nanofillers affect the electrical properties, particularly conductivity of composites and play an important role in charge distribution. LDPE/LDPE–MMT interfaces act as carrier traps and favour accumulation of charges at higher temperatures.

Key words: *LDPE insulation; nanocomposites; insulation interface; space charge dynamics; SEA technique*

1. Introduction

Polymer–clay nanocomposites are two phase materials where nanoscale inorganic particles are dispersed in an organic polymer matrix. On a nanometer level, the inorganic fillers improve the properties of the polymer. Since the nylon–clay nanocomposites with excellent mechanical properties were developed, polymer–clay interactions have been actively studied [1, 2, 3]. The most commonly used clay is montmorillonite (MMT). MMT is a crystalline, 2:1 layer clay mineral in which a central alumina octahedral sheet is sandwiched between two silica tetrahedral sheets [4]. The thickness of the platelets is of the order 1 nm and the aspect ratios are high, typically 100–1500. The molecular weight of the platelets (about 1×10^8) is considerably higher than that of typical commercial polymers. The layers are stacked one above another and the interlayers are occupied by metallic cations, usually Na^+. The silicate layers are coupled by

[*]Corresponding author, e-mail: zylka@elektryk.ie.pwr.wroc.pl

weak dipolar forces or van der Waals forces. The sheets bear charge on the surface and edges, this charge being balanced by counter ions which reside in the inner layer spacing of the clay. One important consequence of the charged nature of the clays is that they are generally highly hydrophilic species and therefore naturally incompatible with a wide range of polymer types. A necessary prerequisite for successful formation of polymer–clay nanocomposites is therefore alteration of the clay polarity to make the clay "organophyllic". It is made by ion exchange reaction. Na^+ ions residing in the interlayers can be replaced by organic cations such as alkylammonium ions, which makes organosilicates compatible to polymers. The organosilicates can be broken down into their nanoscale structures and homogenously distributed in the polymeric matrix to form exfoliated nanocomposites [5]. The exfoliated structure is the most desirable for improvements of mechanical properties, thermal stability and heat resistance. The polymer–clay nanocomposites exhibit improved tensile modulus, decreased permeability to gases, flammability reduction, chemical resistance and environmental protection [6].

Low density polyethylene (LDPE) is one of the most widely used polymers as electrical insulation. LDPE–MMT nanocomposites show improved tensile strength and modulus with good flammability resistance [7, 8]. The improved tensile strengths were observed also at 70 °C [9]. In addition to higher heat resistance and flame retardancy, the LDPE–MMT nanocomposites show the lower impermeability to gases and vapours, what can be the effect of barrier properties [10]. The electric properties of LDPE–MMT nanocomposites were rarely reported. Some results indicate that addition of nanoparticles enhances partial discharge and corona resistance and affects the conduction mechanism of nanocomposites [10–12].

In the present paper, the space charge accumulated in LDPE/LDPE–MMT/LDPE composite multilayer samples after thermoelectret polarization at higher temperature was investigated. The space charge distribution along the sample thickness was measured using step electroacoustic method. The measurements were performed during thermally stimulated discharge of the electret sample with the constant heating rate.

2. Experimental

Materials. Low density polyethylene GGNX 18-D003 (melt index 0.3 g/10 min) was used as a matrix polymer. The MMT nanofiller in the form of granular concentrate C.30.PE (50% PE + 50% MMT) was supplied by Nanocor. A suitable amount (1:7.3) of granular concentrate was added to LDPE matrix in order to obtain concentrations of 6 wt. % of MMT nanofiller. The compounds were mixed simultaneously using internal mixer of rotating single screw extruder. Test specimens were prepared by pressing at 170 °C for 1 min.

Samples. A schematic structure of a specimen is shown in Fig. 1. The thickness of the specimen was typically ca. 210 μm, consisting of 3 layers. The LDPE–MMT layer ca. 90 μm thick is placed in between two LDPE layers ca. 60 μm thick. Ag electrodes

with the diameters of 12 mm were evaporated on the sample in vacuum. The interfaces were formed by laminating pure and composite LDPE films. The layers were

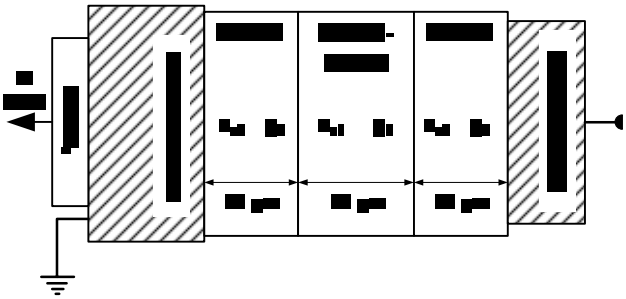

Fig. 1. Schematic diagram of a specimen

pressed firmly at 90 °C in order to avoid any cavities at interfaces. The electrical behaviour of the interfaces depends on microstructure and smoothness of the surfaces, their physical properties as well as temperature and contact pressure. That is why the sample preparation has been completed very carefully. Such three layered samples were polarized at 90 °C by 10 min under dc voltage of 2.1 kV and slowly cooled down under field to room temperature. Then the thermoelectret samples were discharged thermally at constant heating rate b = 2 K/min.

Space charge distribution method. The space charge profiles along the sample thickness were measured using a step electroacoustic system illustrated in Fig. 2.

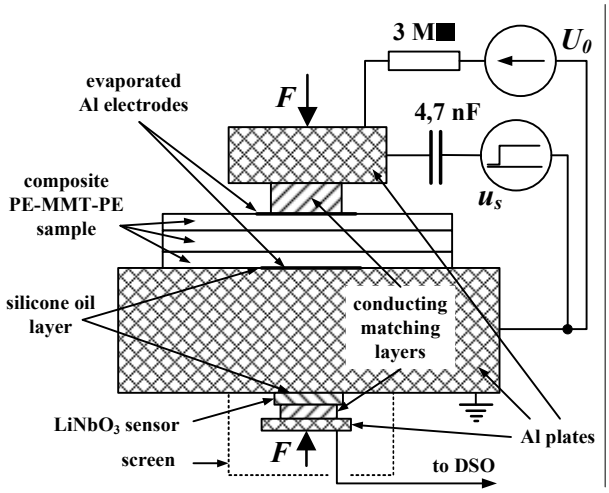

Fig. 2. Schematic SEA setup for measurement of acoustic waves

The three-layered specimen is inserted between electrodes and a step-like voltage u_s is applied to the sample to generate pressure wave. Its rise time is about 1 ns and the

amplitude is 3 kV. The bias dc voltage U_0 was applied for calibration and for measurements. The measurement system is placed in a temperature-controlled chamber with a controlled linear temperature rise. In the presented system, a 0.4 mm thick $LiNbO_3$ piezoelectric crystal was used as a transducer of acoustic waves. It enables measurements at higher temperatures to be performed.

Space charge distributions were measured under dc electrical voltage U_0 = 1.5 kV at temperature range from room to 390 K. The output signal is voltage generated in thick piezoelectric crystal by transmitting pressure wave and measured along R = 50 Ω input of DSO. In the case of the step voltage applied to the sample and thick piezoelectric sensor, the signal related to short circuit current response gives information on electric field distribution. The measured signal $u_R(t)$ is distorted by measurement circuit and should be processed in order to get information on electrical field profiles. In order to obtain quantitative information, the calibration has to be carried out. For this reason, the electric field profiles were integrated. The maximum of the integrated signal corresponds to the sum of the applied voltage u_s+U_0. The calibrated profiles of electric potential distribution for various values of U_0 are shown in Fig. 3.

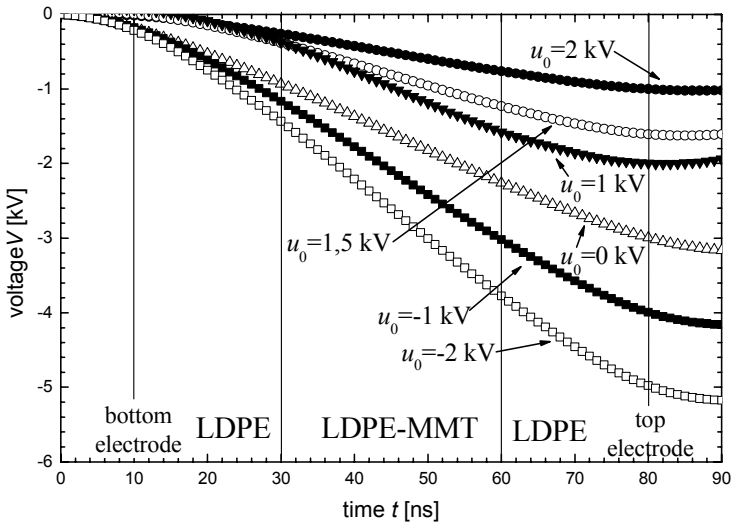

Fig. 3. Electric potential distribution obtained after integration of short circuit signals proportional to the electric field. The positions of interfaces in 3-layered specimen are marked with lines. The specimen was thermoelectrically charged under dc voltage 2.1 kV at 90 °C for 10 min, u_s = –3 kV

The calibrated profiles of the electric field and space charge distributions are obtained from the first and second derivatives and of potential profiles respectively. Location of the charge at position z can be described in terms of time because of the relation $z = vt$, when the sample acoustic wave velocity is v. Perturbation forces generated by step voltage u_s depend on internal space charges in a sample as well as on polarizing U_0 and step u_s voltages applied to the sample. The SEA measurements were per-

formed under condition $U_0 = -0.5u_s$. Under this condition, perturbation forces theoretically should not be related to external voltages and measured signal should give information on internal electrical state of charged sample [13]. It can be seen from Fig. 3 that in the case of $U_0 = -u_s$, the signal at the top electrode equals zero. This means that pressure signals from internal charges and external applied voltages are compensated. This signifies that initial potential from internal charges equals ca. 1.5 kV.

3. Results and discussion

3.1. The SEA signals

The SEA signals measured from 300 K to 375 K for the layered sample are shown in Fig. 4. It can be seen that positions of peaks are shifted in time with the increasing temperature. The shift may be the result of the thermal expansibility as well as decreasing of acoustic wave velocity in Al delay line. These changes were taken into account during interpretation of test results.

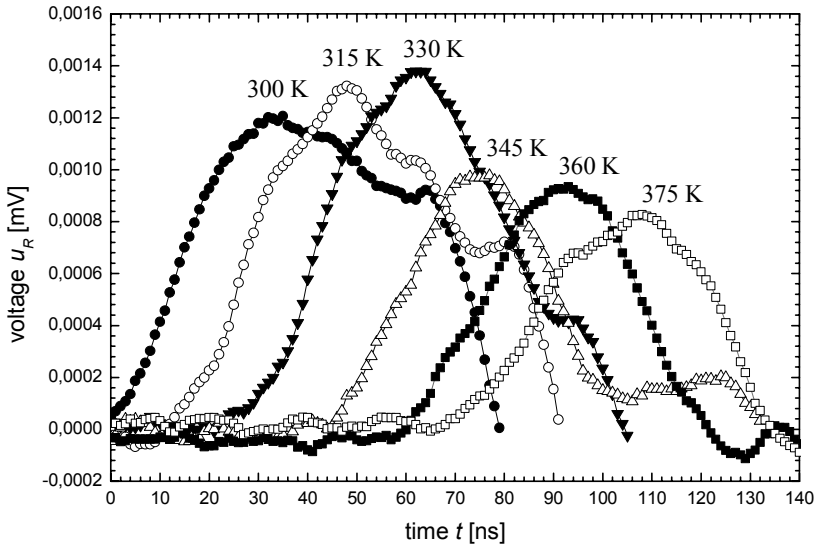

Fig. 4. SEA signals are shifted in time with the increasing of measuring temperature, ranging from 300 K to 375 K; $u_s = -3$ kV, $U_0 = 1.5$ kV

3.2. Space charge and electric field distributions

Figure 5 shows how the internal space charge distribution evolves with time during thermally stimulated discharge process. Signals from charges at electrodes related to applied voltages ($U_0 + u_s$) are not observed.

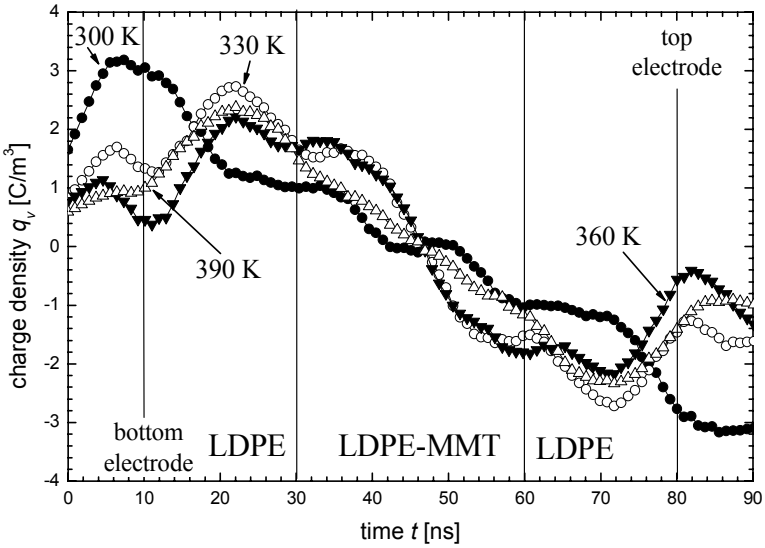

Fig. 5. Evolution of the space charge distributions during TSD at elevated temperatures. Sample polarized under 2.1 kV at 90 °C by 10 min

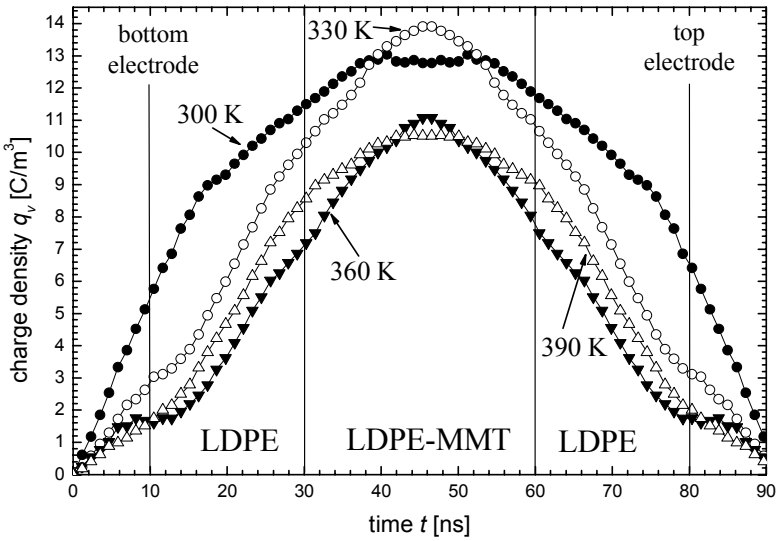

Fig. 6. Electrical field profiles along the LDPE/LDPE–MMT/LDPE composite samples during thermally stimulated discharge

Accumulated charges are heterocharges because the sign of the charge near the electrode is opposite to the electrode potential during polarization process. The heterocharges are dominant in each layer of a triple laminate specimen and in each stage of discharging. The heterocharges originate from the bulk and not from the electrodes. Various organic and inorganic impurities are the major contributor to heterocharges at

low electric field [14]. Initially (300 K) the charge accumulated near electrodes can be seen. Small space charges were observed near LDPE/LDPE–MMT interfaces. Positive heterocharges accumulated in the left LDPE layer near electrode decay during discharging and near the left LDPE/LDPE–MMT interface hetorocharge builds up. It can be observed already at 330 K on the both sides of the interface. The similar behaviour is observed near right LDPE/LDPE–MMT interface for negative heterocharges. The accumulated charges decay gradually with temperature.

Slow decay of space charge causes decreasing of the electric field mainly in the near electrode regions as it is seen in Fig. 6. The maximum electric field occurs in LDPE–MMT layer of the specimen, where the space charge density is equal to zero. It is probably the effect of charges recombination. The slow decay of space charges shows that the nanostructure of MMT generates traps and interfaces which are barriers for charge transport. Electrical properties of LDPE–MMT layer seem to have great influence on space charge distributions.

3.3. Electric characterization of LDPE layers

The measurements of electrical conductivities and permittivities of LDPE and LDPE–MMT nanocomposites were performed from 300 K to 396 K. The temperature dependences of electrical conductivities are shown in Fig. 7.

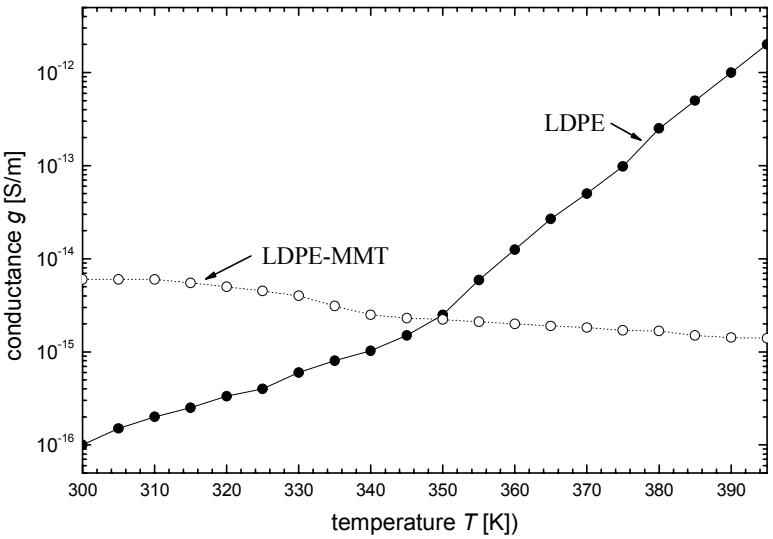

Fig. 7. The temperature dependences of conductivities of pure LDPE layer and MMT doped LDPE layer

A substantial increase of conductivity from 10^{-16} S/m to 10^{-12} S/m in LDPE is observed in the given temperature range, which is a well known phenomenon. However, in the LDPE–MMT nanocomposite, only a slight decrease of conductivity from

6×10^{-13} S/m to 2×10^{-13} S/m can be seen. It indicates that concentration of charge carriers in LDPE–MMT does not change. At low temperatures up to 350 K the conductivity of the LDPE–MMT prevails that of LDPED, while at higher temperatures, the conductivity of pure LDPE is higher than in LDPE–MMT nanocomposite. Therefore, the differences in conductivities can affect the observed changes in space charge and electric field distributions. It seems that permittivities do not affect the observed distributions very much because differences in their values are not significant as it can be seen in Fig. 8.

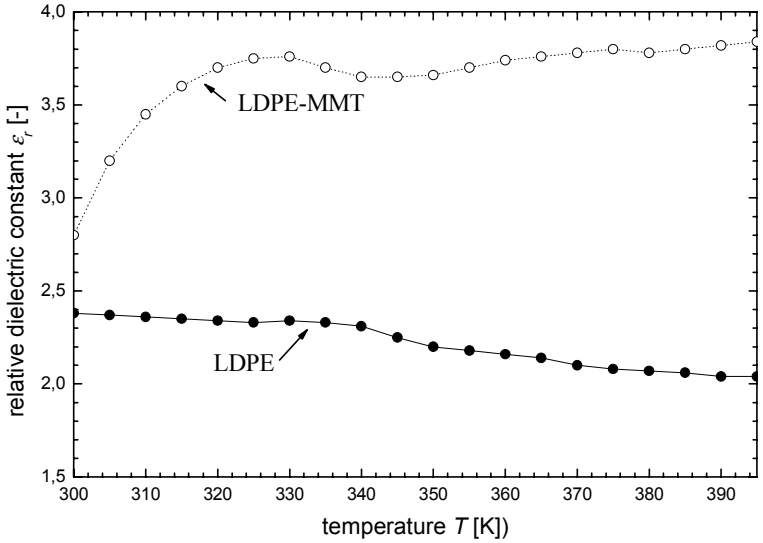

Fig. 8. The temperature runs of relative permittivities of pure LDPE and MMT doped LDPE

3.4. TSD currents

Figure 9 shows short circuit TSD current for triple layer thermoelectret sample polarized at 90 °C by 10 min under 2.1 kV and next slowly cooled to room temperature under the electric field. The thermogram shows peak at 385 K. This peak is related to decay of heterocharges in LDPE stored at near electrode regions. They may originate from low molecular mass impurities [15]. LDPE is partially polar because of organic peroxide compounds, and ketonic carbonyl groups. Such kinds of impurities could be polarized under the voltage to form heterocharges. The released charge during TSD is about 40 μC/m^2 and is similar to the change of the charge accumulated near the electrode. The measuring efficiency of various TSD processes depends on the mechanism of charge decay. The current release by dipole reorientation has the 100% efficiency. In the case of the excess charge decay by drift or conductivity, current efficiency is poor. Decay of symmetrical or antisymmetrical distributions of space charge may give no current in external circuit [16]. The distribution seen in Fig. 5 is symmetric and

great amount of charge is stored near LDPE/LDPE–MMT interfaces above 390 K. Therefore, the interfaces can act as barriers for charge migration where some charge can be trapped during polarization.

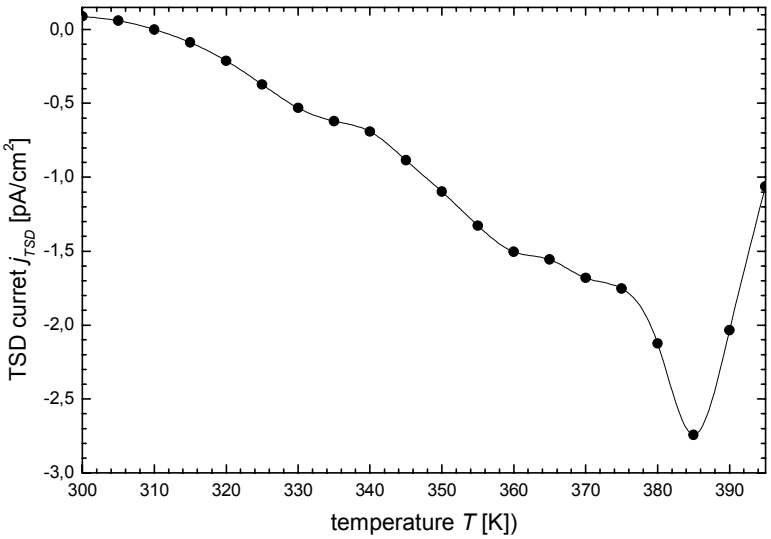

Fig. 9. Thermally stimulated discharge current of triple layer specimen. Thermoelectret sample polarized at 90 °C for 10 min under 2.1 kV

4. Conclusions

A heterocharge was accumulated at interfaces after thermoelectret polarization of triple layer LDPE/LDPE–MMT/LDPE specimens. During thermally stimulated process charge accumulated near electrodes decays first. The change of the charge accumulated near electrode is similar to the released charge during TSD. The high efficiency of decay process suggests dipole reorientation as the main discharge process. The heterocharge stored at LDPE/LDPE–MMT interfaces is very stable. Such interfaces create deep traps and barriers for charges. This phenomenon would result in the reduction of the local electric field between the electrode and the bulk.

References

[1] OKADA A., KAWASUMI M., KURAUCHI T., Polym. Prepr., 28 (1987), 447.
[2] XU W.B., BAO S.P., HE P.S., J. Appl. Polym. Sci., 84 (2002), 842.
[3] ZHANG J., JIANG D.D., WILKIE C.A., Thermochim. Acta, 430 (2005), 107.
[4] CHIN I., THURN-ALBRECHT T., KIM H., RUSSEL T. P. and WANG J., *On exfoliation of montmorillonite in epoxy*, Polymer, Vol. 42 (2001), 5947.
[5] WANG S., LONG C., WANG X., LI Q., QI Z.J., Appl. Polym. Sci., 69 (1998), 1557.
[6] RAY S.S., OKAMOTO M., Prog. Polym. Sci., 28 (2003), 1539.

[7] ZHANG Q., FU Q., JIANG L., LEI Y., 49 (2000), 1561.
[8] ZHANG J.G., WILIKIE C.A., Polym. Degrad. Stab., 80 (2003), 163.
[9] MORON L., ZYLKA P., *Modyfikacja wlasciwosci termoplastycznych nanowypelniaczami*, Dok. Techn. 500-4710-26, Instytut Elektrotechniki, 2003.
[10] CAO Y., IRWIN P.C., YOUNSI K., IEEE Trans. Dielectr. Electr. Insul., 11 (2004), 797.
[11] TANAKA T., MONTANARI G. C. and MULTHAUPT R., IEEE Trans. Dielectr. Electr. Insul., 11 (2004), 763.
[12] TANAKA T., IEEE Trans. Dielectr. Electr. Insul., 12 (2005), 914.
[13] MOTYL E., *Real charges and frozen-in polarization in PET electrets*, Proc. 12th Int. Symp. on Electrets, J.A. Giacometti, O.N. Oliveira Jr., R.M. Faria (Eds.), Salvador, Bahia (2005), p. 250.
[14] SUH K.S., KOO J.H., LEE S.H., PARK J., TAKADA T., IEEE Trans. Dielectr. Electr. Insul., 3 (1996), 153.
[15] LEE S.H., PARK J., LEE C.R., SUH K.S., IEEE, Trans. Dielectr. Electr. Insul., 4 (1997), 425.
[16] VAN TURNHOUT J., *Thermally Stimulated Discharge of Polymer Electrets*, Krips Repro, Leyden (1972).

Received 15 June 2007
Revised 7 October 2009

Materials Science-Poland, *Vol. 27*, *No. 4/2*, *2009*

Influence of thermal ageing on dielectric response of oil-paper insulation

J. GIELNIAK[1*], A. GRACZKOWSKI[1], S. GUBANSKI[2],
H. MORANDA[1], H. MOŚCICKA-GRZESIAK[1], K. WALCZAK[1]

[1]Poznan University of Technology, Poland,

[2]Chalmers University, Goeteborg, Sweden

Results of dielectric response measurements in frequency domain at various temperatures have been presented for oil impregnated paper samples unaged and thermally aged containing various amounts of moisture. The obtained results were used for defining respective master curves and activation energies. Discrepancies of the results for similar samples are also discussed. Finally, statistical spread of the data was presented and the influence of moisture content on the dielectric response of paper samples has been discussed.

Key words: *dielectric response; oil-paper insulation; thermal ageing; moisture content in oil-paper insulation*

1. Introduction

Increase of moisture content in paper results in appreciable decrease of its electrical strength. Similarly, electrical strength of oil depends on relative moisture content as well. Increase of moistening in transformer insulation system results in decrease of bubble effect initial temperature, a very dangerous phenomenon in transformers [1]. Moreover, the paper ageing rate almost linearly depends on its moistening [2–5].

Moisture can penetrate into transformer paper insulation not only from outside. It is a product of cellulose degradation at high temperatures. Unfortunately, presence of water additionally increases the ageing rate.

Paper insulation directly contacts with transformer winding, and is endangered to the influence of hot spots. Paper thermal ageing near hot spots can destroy its electrical strength and leads to transformer failure.

[*]Corresponding author, e-mail: jaroslaw.gielniak@put.poznan.pl

2. Experimental

Objects of investigation. Transformer paper samples impregnated with transformer oil were investigated. Their preparation included the following operations: drying, moisturising, and impregnation with oil. Firstly, samples were dried at 80 °C in a vacuum-thermal chamber for 2–3 days. Their weights were continuously monitored. After drying, the samples were kept in open atmosphere for absorbing moisture from air. Weight changes of the samples were again monitored to obtain predefined levels of moisture intakes. Then the samples were put into containers filled with unused mineral transformer oil, NYNAS Nytro 10 GBN for impregnation. Measured moisture content in the oil was 12 ppm. Three groups of samples were prepared with moisture intake equal to 0.6%, 2.0%, and 4.0%.

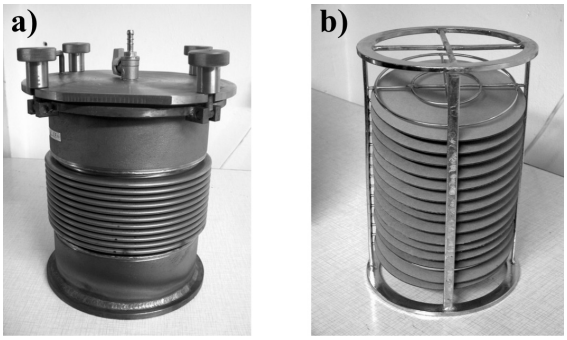

Fig. 1. Container (a) and the stand (b) used to store the samples

Special steel containers (Fig. 1a) were designed for sample storage. The containers were hermetically sealed and prepared to provide possibility for performing temperature treatment. Flexible bellows on the container body reduced inside pressure during ageing at high temperatures. Also a metal stand was designed for holding the samples inside the container. Fifteen samples with the same moisture intake were placed into one container (Fig. 1b).

Paper and pressboard samples with moisture intake of 0.6%, 2.0% and 4.0% were artificially aged. The ageing was carried out in a closed system at 130 °C. Total time of ageing was about 800 h. A temperature distribution in the oven and along the container was regularly observed using a thermal image from an infrared camera. Furthermore, in order to maintain the same ageing conditions, container positions in the oven were regularly changed. From each container (with unaged and aged samples), three samples with similar moisture content were selected and investigated.

Measurement set-up. For the measurements, a paper sample was placed into a test cell filled with oil. Similar oil was earlier used for impregnation of the paper. The test cell was placed in a conditioned chamber. The test cell was designed for three-electrode measurements as shown in Fig. 2. Object of investigation was connected to

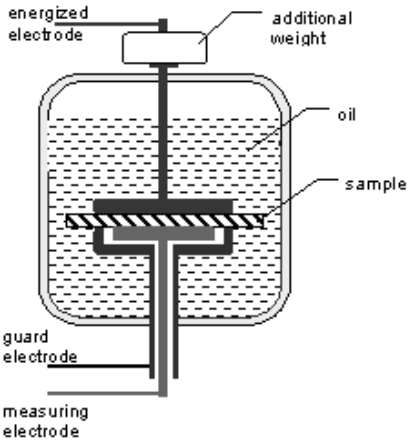

Fig. 2. Scheme of the test cell

Fig. 3. IDA 200 instrument

IDA 200 instrument (Fig. 3). Dielectric response in frequency domain (FDS) was investigated in the frequency range from 0.1 mHz to 1 kHz.

3. Results of investigations

3.1. Dielectric response of unaged and thermally aged paper

Figure 4 presents dielectric responses of chosen new and thermally aged paper-oil samples. Unaged paper was prepared on 4.0% moisture intake, but in the Karl–Fischer (K-F) measurement paper with 4.8% moisture intake was used. After ageing, paper samples were again investigated by the K-F titration, and 3.8% of moisture was determined.

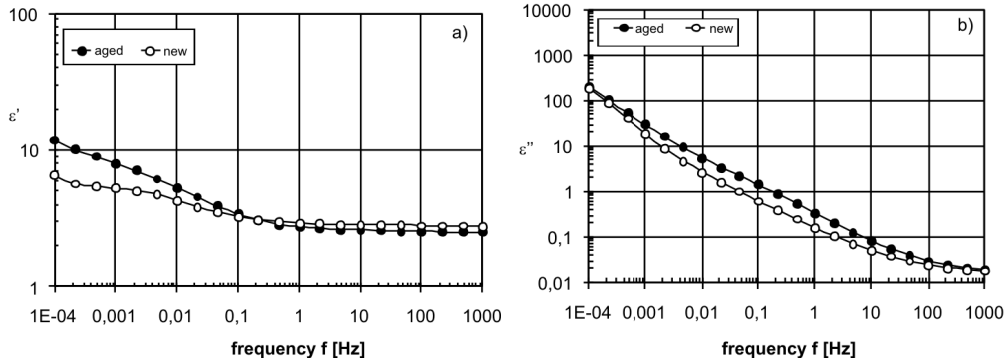

Fig. 4. Dielectric response of paper samples in frequency domain at 20 °C; permittivity: a) real part, b) imaginary part

The shift of dielectric response curves is probably connected with the increase of moisture content in paper samples during ageing. Unfortunately measurements by the K-F method showed decreasing amount of water in aged paper.

The dielectric responses of aged and new samples differ significantly. It clearly shows that dielectric response of paper depends not only on moisture content and temperature but also on ageing state or the substances formed during ageing such as low molecular acids. However, further careful analysis is essential for better clarification of the problem. Table 1 presents average moisture content for investigated paper samples.

Table 1. Average moisture content in paper samples before and after thermal ageing [%]

Moisture content before ageing [%]	Moisture content after ageing [%]
0.6	1.7
2.0	1.7
4.0	2.5

Unfortunately, very dry aged samples (with 0.6% moisture intake) were probably additionally moistened during transport, what manifests in the K-F titration results. The remaining data in Table 1, however, show possible problems with accuracy of the K-F titration method used for measurements.

3.2. Master curves and activation energy

Measured responses of the paper samples with various moisture intake at three temperatures were utilised for obtaining their master curves. Figure 5 presents chosen master curves of permittivity and losses of aged paper at 20 °C. All presented master curves are derived from mean response of three similar samples.

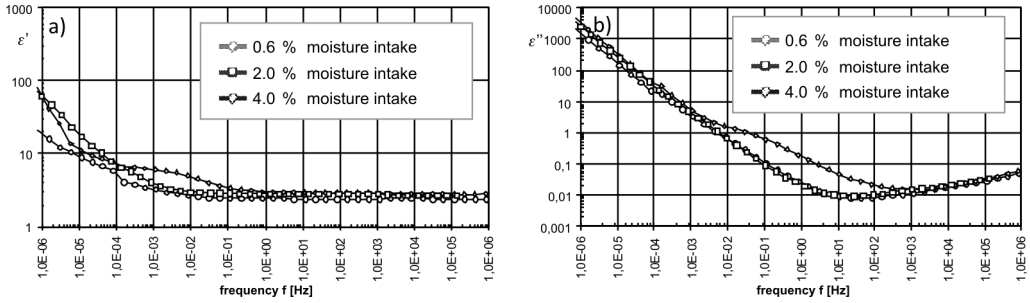

Fig. 5. Master curves at 20 °C for aged paper samples with various moisture content; permittivity: a) real part, b) imaginary part

At first it results from the figures that a real part of permittivity for aged paper is not a good criterion for evaluating the moisture content. Initial moistening of the paper has an immense influence on the ageing process. That is why two samples of the paper with identical moisture content (1.7%) have different ε' values. The moisture content in aged paper should be rather determined based on the analysis of the imaginary part of permittivity.

Table 2. Values of activation energy in aged paper samples

Average moisture intake [%]	Activation energy [eV]
0.6	0.9665
2.0	0.9116
4.0	1.0908

The activation energies with different moisture contents are given in Table 2. No clear dependence of the activation energy for aged paper samples on the moisture intake is visible.

3.3. Discrepancies of the results for similar samples

In Figure 6, the results of measurements of dielectric response for two groups of aged paper samples are presented, with moisture intake of 0.6% and 4.0% at 20 °C. The differences in the results are not significant. They are small enough to distinguish moisture degree of aged paper.

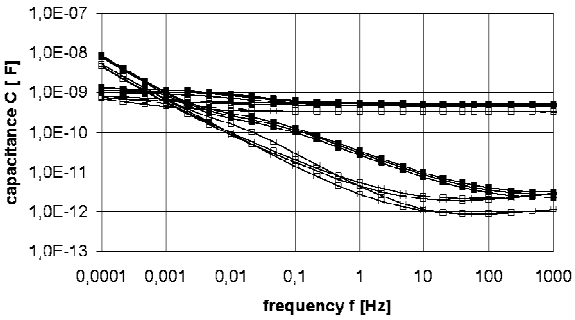

Fig. 6. Complex capacitance in the frequency domain of thermally aged paper samples with moisture intake 0.6% and 4.0% at 20 °C

Figures 7–9 show dispersion bars of dielectric responses for aged samples with 0.6%, 2.0% and 4.0% moisture intake. It is visible that dispersion bars decrease with increasing of moisture intake in paper.

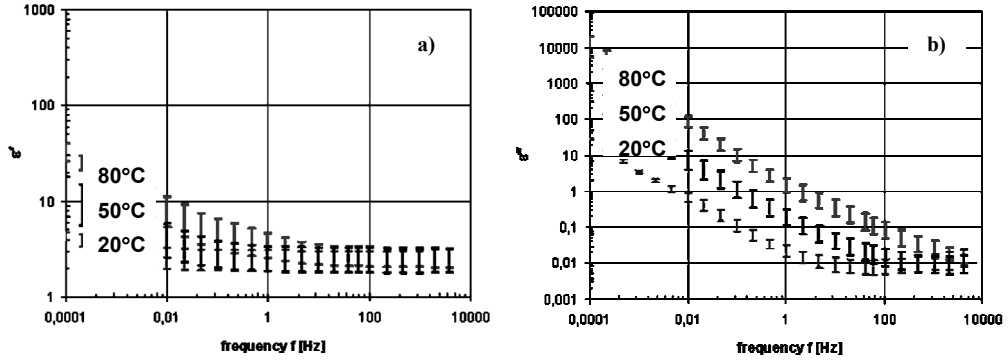

Fig. 7. Dispersion of permittivity error bars of three aged paper samples with moisture intake of 0.6%; permittivity: a) real part, b) imaginary part

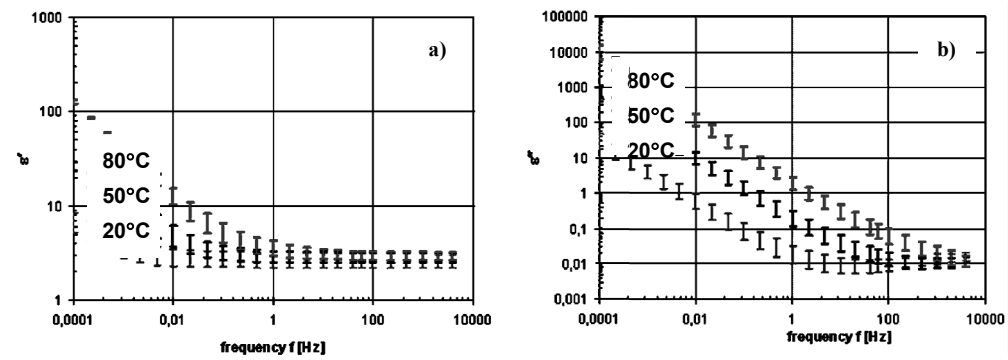

Fig. 8. Dispersion of permittivity error bars of three aged paper samples with moisture intake of 2.0%; permittivity: a) real part, b) imaginary part

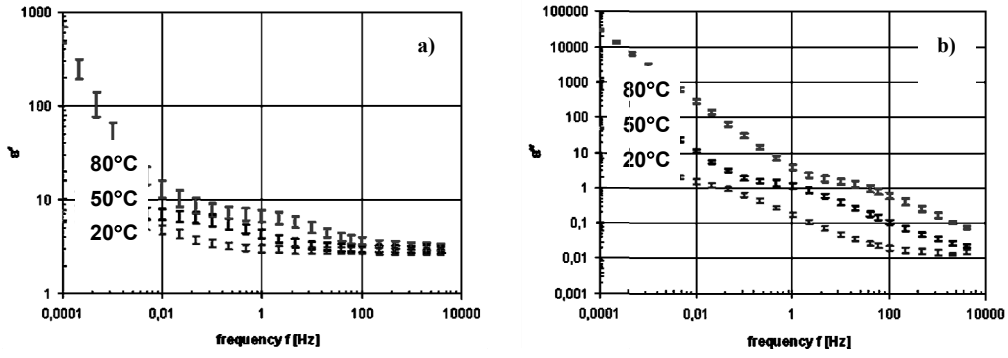

Fig. 9. Dispersion of permittivity error bars of three aged paper samples with moisture intake 4.0%; permittivity: a) real part, b) imaginary part

Presence of the discrepancies in the results of measurements is probably connected with slight differences in moisture content in samples due to various rates of ageing of samples connected with the location of the sample in the container during

ageing. These discrepancies in results of measurements diminish with increase of paper moistening.

4. Conclusions

- Measurements of moisture content in thermally aged paper by the Karl–Fischer titration underrates the values of water content.
- Paper dielectric response depends not only on moisture content and temperature but also on ageing state or presence of substances formed during ageing.
- A real part of permittivity for thermally aged paper is not a good criterion for evaluation moisture content,
- Initial moistening of the paper has a great influence on its thermal ageing.

References

[1] GIELNIAK J., MORAŃDA H., NEUMANN S., OSSOWSKI M., PRZYBYŁEK P., WALCZAK K., MOŚCICKA-GRZESIAK H., *Conditions of occurrence of bubble effect in a transformer with paper-oil* (In Polish), Prep. Sci.-Techn. Conf. Transformers in Operation, Kołobrzeg–Dźwirzyno, 20–22.04.2005, Energetyka, No. 6, 120–122.

[2] LEWAND L., *Understanding water in transformer systems*, NETA World Magazine, Spring, 2002.

[3] SŁOWIKOWSKI J., *Moisturing of a transformer. Reasons, effects and present day criteria of assessment*, Int. Conf. Power Transformers – Transformer 03, Pieczyska, 18–21.05.2003.

[4] GUBANSKI S.M., BLENNOW J., KARLSSON L., FESER K., TENBOHLEN S., NEUMANN C., MOSCICKA-GRZESIAK H., FILIPOWSKI A., TATARSKI L., *Reliable Diagnostics of Transformer Insulation for Safety Assurence of Power Transmission System. REDIATOOL – a European Research Project*, CIGRE Session, Paris 2006.

[5] GJAERDE A. C., LUNDGAARD L., ILDSTAD E., *Effect of temperature and moisture on the dielectric properties of oil-impregnated cellulose*, 9th Int. Symp. High Voltage Engineering, Graz 1995.

Received 2 July 2007
Revised 7 August 2007

Materials Science-Poland, *Vol. 27*, *No. 4/2*, *2009*

The effect of aluminium additive on the electrical properties of ZnO varistors

A. GUBAŃSKI[1], W. MIELCAREK[2*], K. PROCIÓW[2], J. WARYCHA[2], J. M. WRÓBEL[3]

[1]Institute of Electrical Engineering Fundamentals, Wrocław University of Technology, Wybrzeże Wyspiańskiego 27, 50-370 Wrocław, Poland

[2]Electrotechnical Institute, Division of Elecrotechnology and Materials Science, ul. M. Curie-Skłodowskiej 55–61, 50-369 Wrocław, Poland

[3]University of Missouri – KC, Department of Physics, 5100 Rockhill Rd., Kansas City, MO 64110 USA

Reliable and undisturbed operation of electric and electronic circuits is mainly achieved through the use of appropriate overload protection elements such as overvoltage surge arrestors. The stability of metal oxide varistors which are used insures that the circuits are adequately protected. The point of adding the varistor material with aluminium is the extension of the nonlinearity of *I*–V characteristic in high current region. In this work, both the aluminium doping for ZnO varistors, and the effect of this doping on the ageing processes in varistors were investigated. The current trend towards the production of better and more robust surge arrestors which utilize mainly ZnO varistors motivated these studies. The fundamental technological impediments include the repeatability of manufactured varistors and their susceptibility to ageing factors such as current shocks, elevated operation temperature and the extended effect of the operation potential. Improving the varistor imperviousness to ageing continues to be an imperative but, as yet, unsolved problem.

Key words: *ZnO varistors; Al additive; ageing;* I–V *characteristics; TSDC; nonlinearity exponent*

1. Introduction

In order to reduce the destructive effect of overvoltage in power networks, surge arresters are used. These circuits utilize varistors, meaning resistors with variable resistance (variable resistor – VR). Currently, varistors are widely used in both electronic circuits and power networks, often protecting costly devices or an entire installations. Those used in low power devices resemble small parallel-plate capacitors.

*Corresponding author, e-mail: mielcar@iel.wroc.pl

Varistors used in high power equipment have a cylindrical shape, are tens of millimetres in diameter, and are encapsulated in ceramic, epoxy or silicone pipe enclosures.

Varistor fabrication technology has undergone continuous transformation. This progress is stimulated by the desire to lower production costs and improve quality. Lowering the exploitation costs through better protection against failures provides a strong argument for the undertaking the research into varistor technology.

To have varistors working within their specifications is particularly important in exploitation of power networks. Low production costs and a high level of protection has increased the range of varistor applications. The first sintered ceramic varistors were made from silicon carbide (SiC). In the seventies, they were replaced by metal oxide varistors (MOV). Nowadays, oxide based varistors serve as arrestors in a wide range of voltage – from just a few volts to hundreds of thousands of volts [2]. They exhibit strong non-linear current dependence on voltage and are capable of absorbing large quantities of surge energy. Compared to other circuit protection systems such as electronic circuits, they are less expensive and simpler to construct making them more reliable. However, in order to market them effectively, their parameters must be repeatable and fall within precisely specified limits. Understanding and controlling the effects which occur in varistor ceramics, exceeds the range of a single discipline. Current research on this subject is focused on the problem of the conduction mechanisms, the role of the impurities and on the degradation processes. A typical (non-linear) voltage–current (*V–I*) characteristic of a varistor [3] is presented in Fig. 1. The principle of varistor operation is that a raise of the voltage across a varistor above the nominal value, causes an abrupt increase in the overflow current and limits further increase in the voltage.

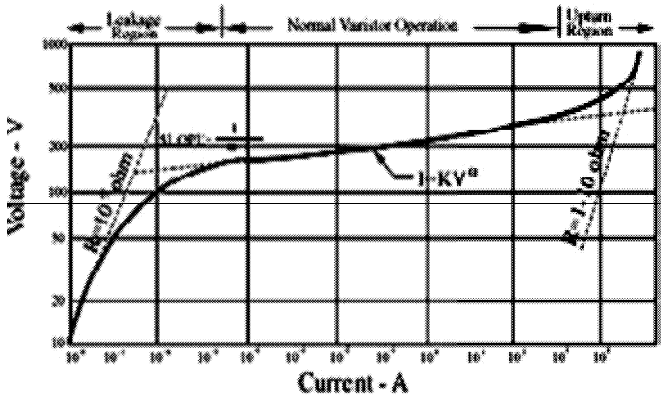

Fig. 1. The voltage–current characteristic of a typical varistor

Three distinct operation regions on the *V–I* characteristic exist; a leakage region (A), conduction (voltage clamping) region (B) and upturn (saturation) region. In the leakage region, the resistance of the varistor is in the gigaohm range and the current value at the applied working voltage is of the order of microamperes. The mechanisms responsible for the operation of ZnO varistors are described below.

The currents associated with thermal emission of electrons across the Schottky potential barrier dominate varistor conductivity in the leakage region. The temperature affects strongly the shape of the *V–I* characteristic in this region. For a single barrier, an exponential function describes the relation between the current density *J* and electric field strength *F* [1]:

$$J = J_0 \exp\left(\frac{E_b - \beta F^{1/2}}{kT}\right) \tag{1}$$

where J_0 is a current constant, β is the proportionality coefficient, k is the Boltzmann constant, E_b is the height of the Shottky barrier, and T is the operation temperature of the varistor.

In the conduction region, varistors reveal their surge protective properties. They become low resistance devices. This part of the *V–I* characteristic can be described by the following exponential dependence

$$I = kV^{\alpha} \tag{2}$$

where k is a ceramic constant dependent on the type of the varistor, the nonlinearity exponent α represents the slope of the characteristic on the double logarithmic scale

$$\alpha = \frac{\log\left(\frac{I_2}{I_{1\,1}}\right)}{\log\left(\frac{V_2}{V_1}\right)} \tag{3}$$

with arbitrary currents I and the corresponding voltages V from this operation region. The nonlinearity exponent of metal oxide varistors a few orders of magnitude exceeds that of carborundum varistors (based on silicon carbide SiC). Depending on the fabrication technology its value may reach 80.

Finally, the upturn region is characterized by a rise in dynamic varistor voltage in line with the current. It is caused by an increase in the resistivity of ZnO grains related to the saturation of free charge carrier concentration. The resistance of the varistor is small (1–10 Ω) and relation between current and voltage is again linear.

The individual operation regions of varistors correspond to the current ranges occurring under real conditions. The operational voltages and the dynamic overvoltages fall into the leakage region (A). The switching overvoltages correspond to the conduction region (B). Supervoltages in the upturn region (C) may be caused by lightning surges.

The tendency of varistors to deteriorate resulting in a rise of the leakage current and asymmetry of the *V–I* characteristics are the major faults of these devices. They are caused by varistor operation at elevated temperatures as well as overvoltage spikes [4–6]. As surge arrestors, varistors should be reliable and maintain their originally

declared specifications over an extended period of time. ZnO varistors are designed and manufactured for specific work conditions described by maximum (continuous) operation voltage V_c, nominal surge varistor voltage V_n, nominal surge current I_n, and the expected shunt current. Exceeding these values during exploitation may result in the failure of the arrestor. In particular, it puts the varistor at risk of degradation. In most cases, it leads to a rise of the leakage current resulting in self-heating of the varistor caused by excess power released in the device. Due to a positive value of the thermal coefficient of conductivity of metal oxide ceramics [7], a heat induced discharge may occur. In more drastic situations, ceramics may break or melt and a surface discharge may occur.

The common reasons for varistor degradation and failures due to ageing include:

- working voltage exceeding the maximum operation value (dynamic overvoltage and ground fault),
- lightning surge current which significantly exceeds the nominal surge current,
- current spikes,
- prolonged overvoltage,
- elevated temperature,
- environmental factors such as ozone, nitrogen oxides, humidity, and pressure.

For a continuous and high level protections of the electric devices provided by arrestors, the varistors must exhibit repeatable characteristics and be stable throughout the entire exploitation period. Usually this requires that any change in the varistor characteristic voltage $V_{1\ mA}$ (which is a voltage at which the current flowing in the varistor has the value of 1 mA [7]), caused by the earlier listed ageing factors, does not exceed 10% of its initial value.

2. Sample preparation

The composition of the material used to prepare the samples for characterization is given in Table 1. Materials of analytical purity were used for manufacturing the samples.

Table 1. Composition of the varistor

Compound	Content [wt. %]
Bi_2O_3	1
Sb_2O_3	1
Co_2O_3	0.5
MnO	0.5
NiO	0.8
Cr_2O_3	0.4
ZnO	95.8

The processing included milling, mixing and homogenization, drying, granulation, pressing, sintering (1250 °C for 1 h), deposition of the electrodes, and packaging. The prepared varistors were 12 mm in diameter and 2 mm thick. Hydrogenated aluminium

nitrate ($Al(NO_3)_3 \cdot 9H_2O$) mixed with ground ZnO powder was used for the aluminium doping of the varistor mass. The doping levels, as well as the dimensions of the samples prepared in this process, are listed in Table 2.

Table 2. Aluminium content and the parameters of the investigated samples

No.	Diameter [mm]	Thickness [mm]	Al content	
			[ppm]	[g]
1	12	2.40	0	0
2	12	2.42	12	0.001
3	12	2.38	24	0.002
4	12	2.18	48	0.004
5	12	2.18	96	0.008
6	12	2.26	192	0.016

3. Experimental

Varistor samples were placed in a heat chamber, and a laboratory made system for the investigation of passive elements was utilized. The system allows experiments to br carried out at both constant and pulsed currents at maxima of 2 kV and 200 A. Computer controlled, METEX multimeters were also used to measure the current and voltage.

Two ageing factors were used for provoking the degradation process:

- exposure of the samples to an elevated temperature of 115 °C,
- constant overvoltage resulting in a 50 μA current.

The ageing experiment was carried out over of a period of 24 h. Additionally, the stabilized current was maintained in the varistor during the process. The procedure allowed one to preserve the conductive paths within the volume of the varistor.

The system used for thermo-stimulated discharge current (TSDC) measurements is described elsewhere [8]. Before the temperature scan, the sample was cooled in a cryostat to 100 K at a constant electric field. The TSDC spectra were collected with the temperature increasing at a constant rate (4 deg/min) from 100 K to 500 K.

4. Results and discussion

The ZnO-based varistor samples were subjected to a series of investigative procedures. The goal of these studies was to determine their properties such as characteristic voltage ($V_{1\ mA}$), nonlinearity exponent, *I–V* characteristic curve, relaxation parameters (location and height of the TSDC peaks, and activation energy for individual depolarization processes) obtained in the TSDC measurements. The experimental results ob-

tained from examination of the as-received structures provide a basis for evaluation the influence of aluminium doping on varistors.

The investigations of the *I–V* characteristics were carried out using the constant current method. The voltage was normalized to 1 mm thickness of the sample. The results shown in Fig. 2, allow one to determine the parameters of the studied samples. The *I–V* curves were used for determination of the nonlinearity exponents in the 0.1 μA–1 A current range. In this range, the samples with smaller aluminium concentrations (0 and 12 ppm) reach the highest values of the nonlinearity exponent. A significant drop of this parameter is observed in the samples with 96 and 192 ppm additive concentrations. The investigated current range lies on the boundary between the leakage region and the conduction region, and the effect of the Al additive on the nonlinearity exponent may be related to an increase in the leakage current in the doped samples.

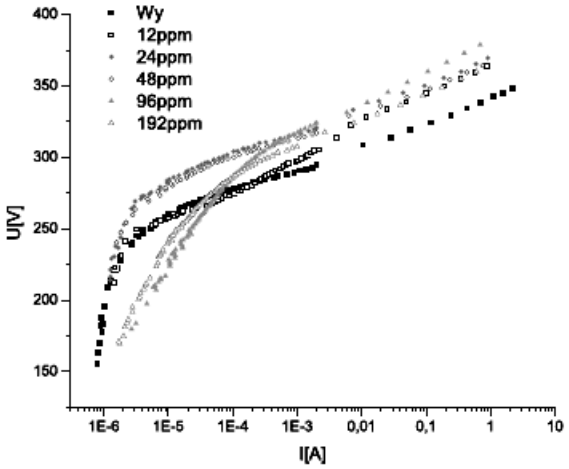

Fig. 2. The *I–V* characteristics of brand new varistors with various levels of aluminium doping

A significantly higher leakage current is observed in as-recived samples doped at 96 and 192 ppm levels. At 250 V (per 1 mm of sample thickness), the leakage current is greater by a factor of about ten when compared to less doped samples. This implies that aluminium exerts a detrimental influence on the leakage operation region of the varistors. Higher current values cause additional danger associated with selfheating. As seen in Fig. 3, the temperature coefficient of ZnO resistivity is negative, and hence the temperature rise further increases the current. It may eventually initiate the thermal breakdown of the resistor. The nonlinearity exponents found from the *I–V* characteristics are listed in Table 3. The results show that for as-received samples, higher aluminium doping reduces the slope of the *I–V* characteristic in the leakage region. Comparing the slopes on the *I–V* curves for samples with a different concentration of the additive, clearly indicates the undesirable influence of aluminium doping in the leakage region and no effect in the conduction region.

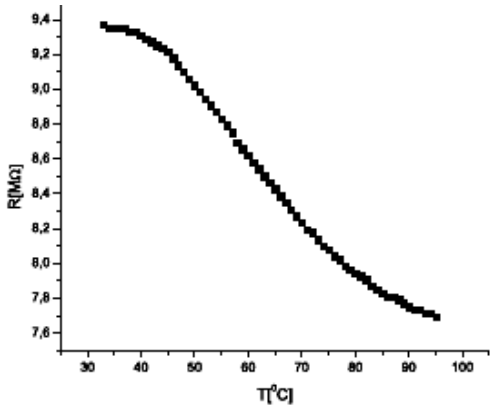

Fig. 3. Temperature dependence of resistance for a ZnO varistor at the stabilized current of 50 μA

Table 3. Nonlinearity exponents α, and characteristic voltages $V_{1\ mA}$ of as-recived varistor samples obtained from the *I–V* characteristics

Al [ppm]	α	$V_{1\ mA}$ [V]
0	42	291
12	33	297
24	42	317
48	44	314
96	36	317
192	39	307

Figure 4 represents typical TSDC spectra for the ZnO varistor cores being investigated. Three well separated peaks (α, β, and γ) appear in the spectra of undoped varistor material as well as in varistor material that has been slightly doped with aluminium (12, 24, 48 ppm). This has been interpreted to mean that the low temperature peak (α) may be associated with electron trapping in the layers between the ZnO grains [9]. The next peak (β) is linked to electron trapping on the donor levels in the depleted region of the Shottky barriers at the grain boundaries. Space charge and ion migration cause the last peak (γ). Highly doped samples, at the 96 and 192 ppm level, lack the low temperature peak in the TSDC spectrum. This is associated with trapping in the grains and indicates that aluminium additive may influence the relaxation process. The characteristic values of both the current and the temperature for the three spectral features in the TSDC spectrum of brand new samples are listed in Table 4. For purposes of comparison, three calculation methods were utilized in order to determine the activation energies. The initial rise method and the Bucci method [10, 11] yield considerably different values of the activation energy. The discrepancies are caused by the

differences in both the calculation methods and the assumed simplifications. The values obtained are listed in Table 5.

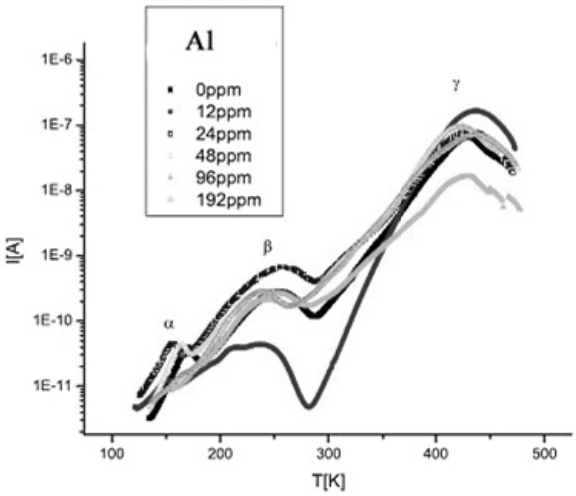

Fig. 4. TSDC spectra for aluminium doped ZnO samples

Table. 4. Maxima in the TSDC spectra of as-recived samples and their location on the temperature scale

Al [ppm]	I_{max} [A]			T_{max} [K]		
	α	β	γ	α	β	γ
0	3.9×10^{-11}	2.8×10^{-10}	6.6×10^{-8}	170	253	428
12	1.2×10^{-11}	4.4×10^{-11}	1.6×10^{-7}	151	237	435
24	4.5×10^{-11}	6.6×10^{-10}	7.8×10^{-8}	157	256	429
48	4.4×10^{-11}	2.2×10^{-10}	9.5×10^{-8}	164	243	420
96	–	2.6×10^{-10}	1.6×10^{-8}	–	251	428
192	–	2.8×10^{-10}	7.0×10^{-8}	–	238	436

Table 5. Activation energies E_a [eV] determined by the Bucci method, the initial rise method and with the TSDFit computer software

Al [ppm]	TSDFit	BFG	initial rise		
	α	β	α	β	γ
0	0.59	0.59	0.14	0.12	0.4
12	0.87	0.87	0.04	0.06	0.57
24	0.60	0.60	0.08	0.12	0.26
48	0.50	0.50	0.15	0.10	0.11
96	0.35	0.22	–	0.05	0.14
192	0.43	0.43	–	0.06	0.15

During the ageing processes, variations of the voltage across the varistor were continuously monitored over a 24 h period. Figure 5 represents a typical result for an electrothermally aged varistor. A drop in voltage is observed, confirming the existence of degradation processes in the sample. The removal of the thermal factor yielded a restoration of voltage, meaning that the varistor partially regained its initial properties. In order to find which factor has the decisive influence and what its character is, three samples were exposed exclusively to thermal ageing at the same temperature (115 °C) and over the same time period (24 h). For each sample, the original *I–V* characteristics were compared with those obtained after thermal ageing. The curves were identical before and after the process. Hence one can conclude that thermal factor alone does not cause deterioration of the varistor but accelerates degradation caused by the electrical factor.

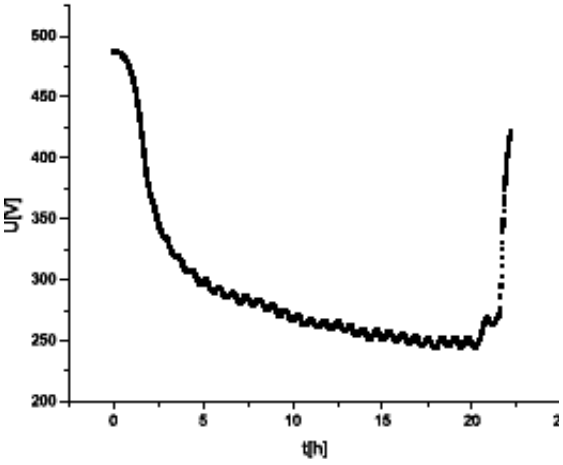

Fig. 5. The time dependency of the voltage across a varistor undergoing an electro-thermal ageing process

After the electrothermal ageing, the sample parameters were investigated again. The purpose of these measurements was to verify the sensibleness of aluminium doping and the influence of the impurities on the degradation processes in ZnO varistors. The measurements of the *I–V* characteristics as well as the measurements of the TDSC were carried out. Ageing related changes have been identified. From the *I–V* curves, the nonlinearity exponents in the 50 μA–1 A range and the characteristic voltages per 1 mm sample thickness were obtained. The values are listed in Table 6. In the undoped sample one can clearly see the effect of ageing on the *I–V* characteristic. Significant changes occur in both the leakage region and the conduction region of the varistor. The ageing caused an increase in the leakage current and deterioration of the nonlinearity exponent of the sample. Varistor degradation also increased the resistance of the sample in the conduction region. The aluminium doped samples behaved similarly in the leakage region. After ageing, the leakage current increases noticeably.

However, the degeneration looks different for a greater current. Samples with doping levels of 12, 24, 48 and 192 ppm do not exhibit degenerative changes in the conduction region. The sample doped at the 96 ppm level is an exception showing traces of degeneration in this region. Degradation had no effect on the value of the characteristic voltage. Independent of the doping level, the characteristic voltage remained at the original level after the ageing. Aluminium doping improved the stability of the nonlinearity coefficient. The undoped sample had the largest percentage drop of the nonlinearity coefficient after the ageing. The remaining samples even improved this parameter over their original values. However, there is no proportionality between the percentage changes of the coefficient and the doping level. Samples doped at 12, 48 and 192 have the lowest drop of the nonlinearity exponent due to ageing. The TSDC spectra of the aged varistors show degradation traces through the shift of the low temperature peak toward lower temperatures. The effect of ageing on the activation energies is also noticeable. In the majority of the samples, the activation energy associated with peaks α and β decreased. Table 7 contains the values of the maxima of TSDC peaks and their locations on the temperature scales before and after the ageing.

Table 6. The nonlinearity exponents and the characteristic voltages per 1 mm of as-recived and aged varistors

Al [ppm]	New sample		Aged sample	
	α	$V_{1\,mA}$ [V]	α	$V_{1\,mA}$ [V]
0	42	291	22	317
12	33	297	31	316
24	42	317	27	317
48	44	314	35	313
96	36	317	21	338
192	38	307	32	304

Table 7. Maxima in the TSDC spectra and the corresponding temperatures

Al [ppm]	I_{max} [A]			T_{max} [K]		
	α	β	γ	α	β	γ
0	4.7×10^{-11}	3.5×10^{-10}	1.1×10^{-7}	138	257	434
12	8.3×10^{-13}	1.3×10^{-10}	1.4×10^{-7}	135	245	462
24	4.5×10^{-11}	4.3×10^{-10}	1.5×10^{-7}	149	250	454
48	2.3×10^{-11}	1.5×10^{-10}	9.2×10^{-8}	140	243	435
96	–	4.2×10^{-10}	1.6×10^{-7}	–	245	425
192	–	1.9×10^{-10}	1.5×10^{-7}	–	244	464

The activation energies of the individual depolarization processes are listed in Table 8. All values were determined using the initial rise method.

Table 8. Activation energies E_a [eV] corresponding to the individual peaks of the TSDC spectra for as-recived and aged samples

Al ppm	As-received sample			Aged sample		
	α	β	γ	α	β	γ
0	0.14	0.12	0.4	0.09	0.06	0.2
12	0.04	0.06	0.57	–	0.09	0.31
24	0.08	0.12	0.26	0.1	0.09	0.14
48	0.15	0.1	0.11	0.13	0.7	0.31
96	–	0.05	0.14	–	0.02	0.1
192	–	0.06	0.15	–	0.02	0.09

5. Conclusions

Samples exposed exclusively to thermal ageing (115 °C, 24 h) experienced no degradation. Their *I–V* characteristics before and after ageing are identical. Only combined electrothermal ageing caused degradation of the samples. In this case, the temperature acted as an initiating and accelerating factor for the electrical ageing process.

Independent of the aluminium content, the ageing process had no effect on the characteristic voltage $V_{1\ \mathrm{mA}}$ of the investigated varistors. However, the aluminium impurities increased the current values. In the highly doped samples (192 ppm), the currents definitely have larger values.

The largest percentage drop of the nonlinearity exponent occurred in the undoped sample. Nevertheless, because of an increase in the leakage current and a drop in the nonlinearity coefficient, excessive doping levels are undesirable. High doping level also causes that the characteristic voltage $V_{1\ \mathrm{mA}}$ becomes lower.

Electro-thermal ageing lowers the position of the low-temperature TSDC peak on the temperature scale. Highly doped samples do not exhibit this peak at all.

Acknowledgements

This work was entirely supported by the Polish Ministry for Scientific Research MNSW under grant No. N N510 344534.

References

[1] KOSMAN M.S., PETCSOLD E.G., *O wozmoznosti izgotowlenija simietriczeskich varistorov iz okisi cinka c primiestju okosi bizmuta*, Uczonyje zapiski LGPT im. A.I. Gercena, 207 (1961), 191–196.
[2] *Harris Semiconductor Transient Voltage Suppression* Products Data book, Harris Corporation 1993.
[3] MATSUOKA M., Jpn. J. Appl. Phys., 10, (1971), 736.
[4] EDA K., IGA A., MATSUOKA M., J. Appl. Phys., 51 (1980), 2678.
[5] JAWORSKI M., WRÓBLEWSKI Z., Przegl. Elektrotechn., 76 (2000), 1.

[6] PHILIPP H.R., LEVINSON L.M., *Degradation phenomena in zinc oxide varistors – a review*, [In:] *Advances in electronic ceramics*, Vol. 7, *Additives and interfaces in electronic ceramics*, M.F. Yan, A.H. Hener, Columbus, Ohio, Am. Ceram. Soc., 1984, 1–21.
[7] HOZER L., *Semiconductor Ceramics: Grain Boundary Effects*, Ellis Horwood Ltd., 1994.
[8] GUBAŃSKI A., MACALIK B., Bull. Acad. Sci., 35 (1987), 537.
[9] EMTAGE P.R., J. Appl. Phys., 48,(1977), 4372.
[10] GARLICK G.F.J., GIBSON A.F., Proc. Phys. Soc., 60 (1948), 574.
[11] BUCCI C., FIESHI R., GUIDI G., Phys. Rev., 148, (1966), 816.

Received 26 April 2007
Revised 14 August 2007

Materials Science-Poland, *Vol. 27*, *No. 4/2*, *2009*

The influence of barium titanate as a filler in impregnating epoxy resin on chosen electrical parameters of obtained material

W. KASPRZAK[1], Z. NADOLNY[1*], K. WALCZAK[1], K. SIODŁA[1], W. SIKORSKI[1], K. JÓŹWIAK[1], G. PAŚCIAK[2], L. MOROŃ[2]

Poznan University of Technology

Wroclaw Division of Electrotechnical Institute

The paper describes the influence of barium titanate $BaTiO_3$ used as a filler in impregnating epoxy resin on electrical parameters of obtained material. The results of computer simulation of electric field intensity distribution in area of 220 kV ac composite insulator show that in order to reduce the maximum value of this field it is necessary to use the rod with the highest possible permittivity. It was assumed that the increase of rod permittivity is possible by doping the epoxy resin, being one of glass-epoxy rod components, with a filler having high permittivity. Barium titanate $BaTiO_3$ in micro- and nanograins was used as a filler. Presumably, such a change in material structure, may negatively influence other electrical parameters of the material, important in composite insulators construction. In order to check the filler dispersion in epoxy matrix, microscopic observations of fractions of the obtained materials were performed. In a wide range of frequencies, the permittivity and volume resistivity of the materials were determined. The inception voltage of partial discharges on surface of materials was determined by the electric, acoustic and antenna methods.

Key words: *nanofillers; $BaTiO_3$; epoxy resin; permittivity*

1. Introduction

Usually, a composite insulator is made of glass-epoxy resin rod with the relative permittivity 5 and covering material (silicone rubber) with the relative permittivity 3. The results of last years investigations show that a suitable modification of dielectrics with nanofillers will presumably make steering of material permittivity possible.

The modification of dielectrics relies on introduction of suitable nanofillers to material matrix. A nanofiller is a polycrystalline substance built-up of grains with

[*]Corresponding author, e-mail: zbigniew.nadolny@put.poznan.pl

a diameter of at most hundred nanometres. The popularity of use of nanofillers grows thanks to specific nanoscale phenomena and not present in materials with fillers of micrometric grains. Thus, the use of microfillers may lead to obtainment of materials with properties better or other than the properties of microfilled materials with the same chemical composition. The right choice of a nanofiller permits to improve, among others, electrical, mechanical or thermal properties of dielectrics. The best known nanofillers are alumina Al_2O_3, titania TiO_2, silica SiO_2, barium titanate $BaTiO_3$, zinc oxide ZnO and ferric oxide Fe_2O_3.

Electrical strength, resistance to partial discharges and appearance of conducting paths due to partial discharges, dielectric loss factor, resistivity or permittivity are the electrical properties which may be changed by nanofiller addition [1–12].

2. Objective and scope of investigations

The increase of permittivity, with preservation or improvement of other electrical parameters and remaining of impregnating properties of epoxy resin, was the goal of the researches. The increase of permittivity was realised by addition of barium titanate in form of micro- and nanograins as a filler. In this way, three materials were disposed: epoxy resin without filler, epoxy resin with micrograins of barium titanate and epoxy resin filled with nanograins of $BaTiO_3$.

A stress should be put on fact that the change of dielectrics permittivity in composed insulating systems ameliorates electric field distribution and improves work conditions of these systems. Still, it is important to remember that in the case of simple insulating systems, the conditions in triple junction (electrode–dielectric–air) may become worse. An increase of electric field intensity in triple junction should be expected. It consequences in partial discharges inception voltage and flashover voltage decrease. In order to carry out quantitative estimation of these effects, surface partial discharges and flashover voltage of investigated materials were determined.

The permittivity and resistivity of obtained materials were determined in a wide frequency range (from 0.001 up to 1000 Hz). On surfaces of obtained materials flashover voltage and partial discharges inception voltage were measured. The latter was measured with the use of classical electric, acoustic emission and ultra high frequency methods.

The observations of material fractures were performed with scanning electron microscope (SEM) in order to check the fillers dispersion uniformity in epoxy resin.

3. Investigation objects

The samples of impregnating epoxy resin without a filler, filled with micrograins of barium titanate (64 wt. %), and filled with nanograins of barium titanate (32 wt. %) were investigated. In order to measurably increase the permittivity epoxy resins, addition of the highest possible quantity of barium titanate was overtaken, at condition that impregnating properties of the resin were preserved. As a consequence, epoxy resin

samples with 64 wt. % of micrograins of barium titanate and with 32 wt. % of nanograins of barium titanate were obtained.

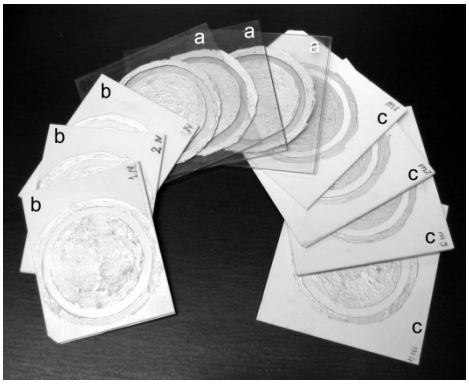

Fig. 1. Samples of impregnating epoxy resin: without filler (a), with nanograins (b) and micrograins (c) of barium titanate

At least three samples of each material were fabricated. They were 2 mm thick with the dimensions of 10×8 cm^2 or 10×10 cm^2 (Fig. 1).

4. Results

The main goal of researches was to obtain materials with increased permittivity at 50 Hz. However, the permittivity was determined with Programma IDA 200 device in much wider range of frequency (from 0.001 Hz up to 1000 Hz). Average values of the permittivities are shown in Fig. 2. As can be seen, they are steady in the whole range of frequencies. At 50 Hz, unfilled epoxy resin has the relative permittivity equal to 3.9. The addition of nanofiller to epoxy resin caused the increase of permittivity to 5.4, and the addition of microfiller increased the permittivity to 12.7.

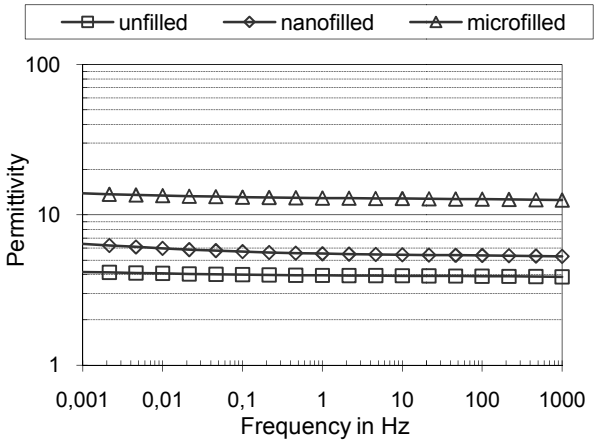

Fig. 2. Permittivity of investigated materials as a function of frequency

The results obtained for samples of epoxy resin with the nanofiller are surprising for two reasons. Firstly, expected growth of permittivity, usually caused by the use of nanofillers, was not observed. Secondly, the increase of permittivity was not comparable even to expected growth caused by use of the same amount of microfiller. Unexpected results of permittivity measurements inclined observations of the filler dispersion in the epoxy matrix. Inadequate dispersion of the filler in matrix influences the properties of the material. The simplest microscopical method, observation of fractures in SEM, was employed. A fracture of epoxy resin without a filler, being a basis for comparison of the filler distribution, is shown in Fig. 3.

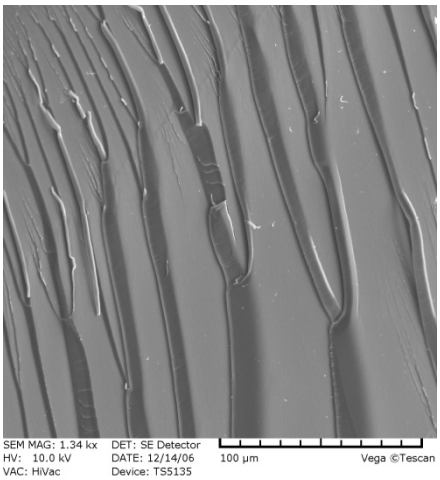

Fig. 3. Fracture of epoxy resin without fillers

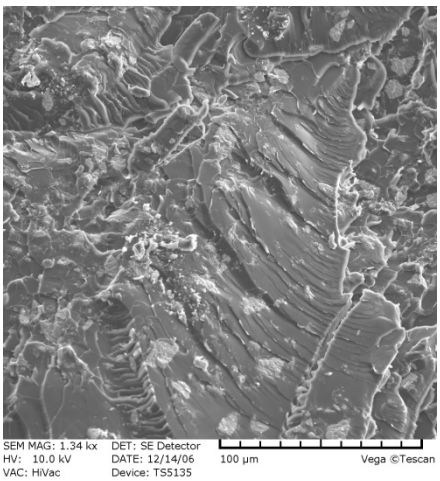

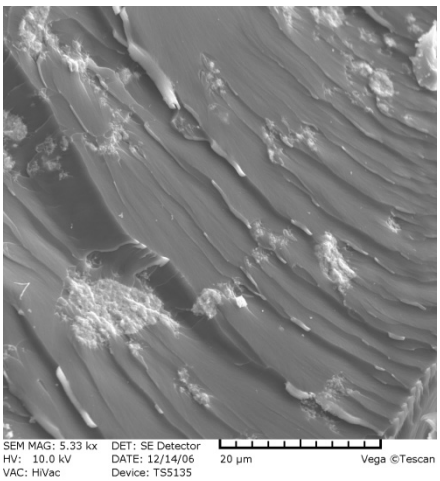

Fig. 4. Fracture of epoxy resin with barium titanate nanograins at two different magnifications

The fracture of the sample containing nanofiller grains is presented in Fig. 4. It is evident that the distribution of barium titanate is nonuniform and nanograins form

agglomerates of greater dimensions, up to more than ten microns. This phenomenon was probably caused by lack in equipment used for the sample preparation. It was not the case for epoxy resin with the microfiller, where distribution of grains is quite uniform as is shown in Fig. 5. Nonuniform distribution of filler nanograins has evidently caused the surprising results of the measurement of electric permittivity.

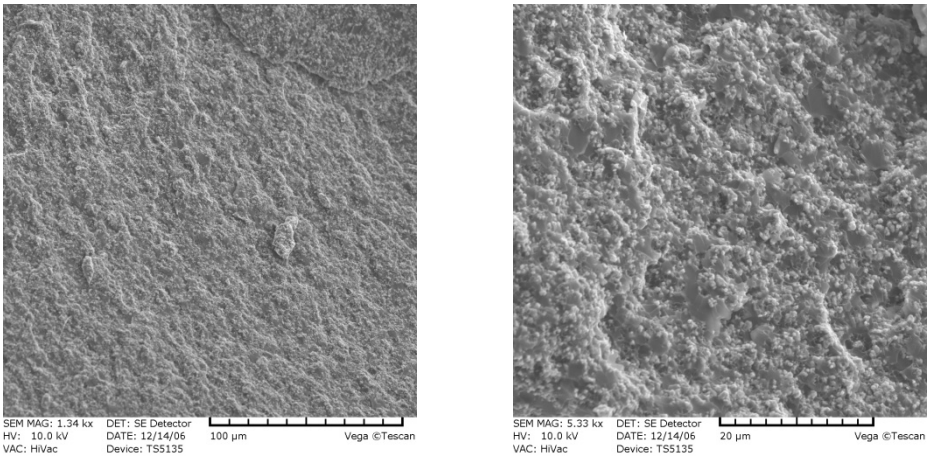

Fig. 5. Fracture of epoxy resin with barium titanate micrograins at different magnifications

The measurement of dielectric loss factor and volume resistivity was carried out with electrodes sputtered on surface of material as is shown in Fig. 1.

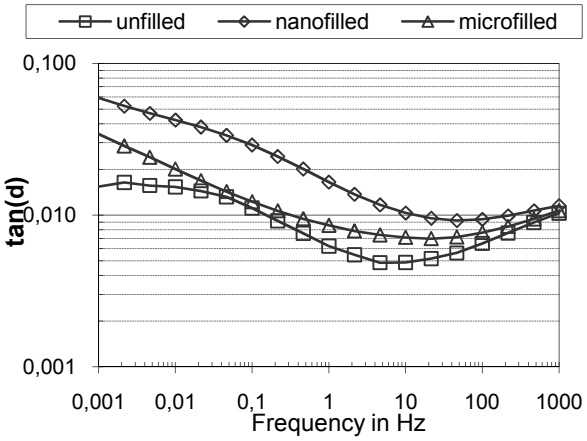

Fig. 6. Average tan(δ) of investigated materials as a function of frequency

The measured values of average tan(δ) of three analysed materials are shown in Fig. 6. At 50 Hz, the loss factor of unfilled resin was 60×10^{-4}. The addition of the microfiller caused a slight growth up to 70×10^{-4}, while the addition of the nanofiller

increased tan(δ) up to 90×10^{-4}. As can be seen, the addition of fillers caused only a small growth of the dielectric loss factor.

The results of measurements of the volume resistivity are shown in Fig. 7. As can be seen, irrespective of the filler grain size, their introduction to epoxy resin matrix caused the decrease of the volume resistivity at most of one order of magnitude.

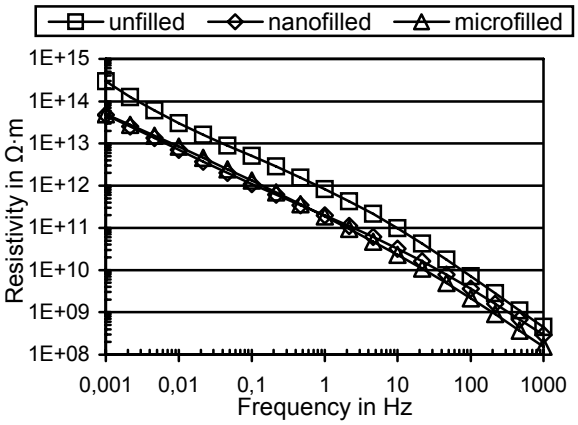

Fig. 7. Volume resistivity of investigated materials in function of frequency

In systems layered in series, permittivity influences distribution of the electric field. Basically, its intensity is higher in materials with lower permittivity. Thus, in simple systems, the increase of permittivity of epoxy resin should cause the raise of electric field intensity in air. Consequently, surface partial discharges inception voltage and flashover voltage should decrease. For these reasons, partial discharges inception voltage and flashover voltage were determined.

Both in the case of partial discharges inception voltage and flashover voltage, cylindrical electrodes were placed in the middle of the investigated sample, 20 mm one from another, as shown in Fig. 8.

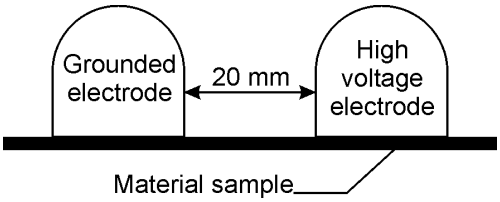

Fig. 8. Electrodes set-up for partial discharges measurement

Flashover voltage was equal to 19.5 ± 0.7 kV on samples of epoxy resin without a filler, 20.0 ± 0.8 kV for samples with the nanofiller and 16.3 ± 0.6 kV with the microfiller. As can be seen, the introduction of barium titanate nanograins did not cause changes of the flashover voltage, whereas the use of microfiller reduced it by ca. 15%.

In partial discharges inception voltage measurements, for the sake of security, the maximum voltage value was equal to 13 kV, which is 80% of the lowest flashover voltage on the surface of investigated materials.

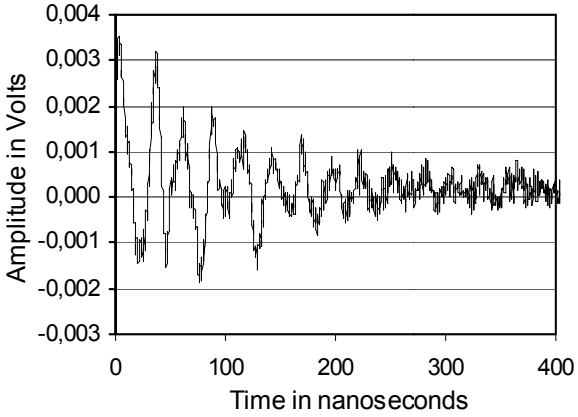

Fig. 9. Example of a partial discharge impulse on surface of epoxy resin with microfiller, registered with UHF probe

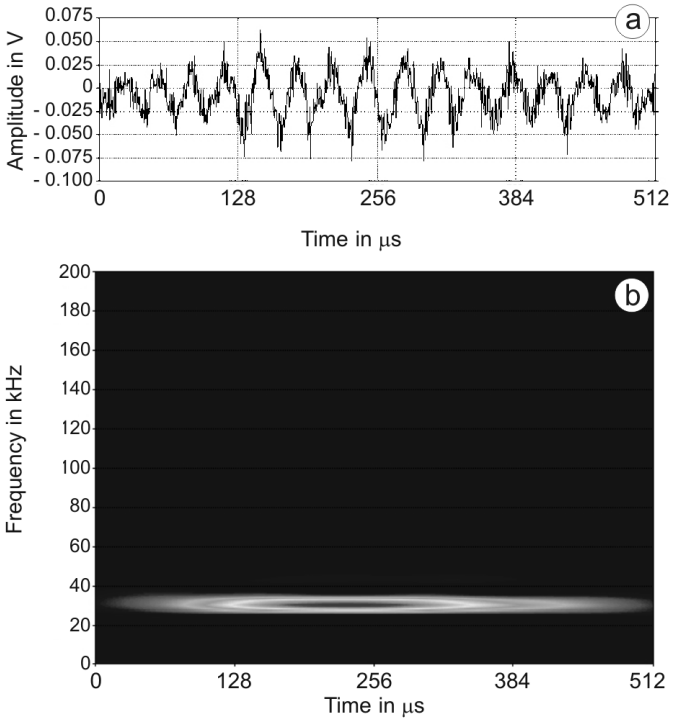

Fig. 10. Chosen partial discharge impulse recorded with an acoustic sensor (a) and its analysis by continuous wavelet transform (b)

The inception voltage of partial discharges developing on surfaces of investigated materials was determined by three independent methods: classical electric, acoustic emission and UHF. In the cases of epoxy resin without filler and filled with nanograins of barium titanate, up to 13 kV no partial discharges were observed. In the case of epoxy resin with a microfiller, some partial discharges were recorded. The inception voltage, measured by the applied method, was equal to 12.0 ± 0.9 kV. An example of a partial discharge impulse, recorded with a UHF probe is shown in Fig. 9. Evaluated time parameters of the impulses are typical of surface partial discharges [13].

A chosen impulse recorded with an acoustic sensor is shown in Fig. 10a, and its joint time-frequency analysis (continuous wavelet transform spectrogram) is shown in Fig. 10b. The frequency parameters of the signal confirm that it was generated by a surface partial discharge [14].

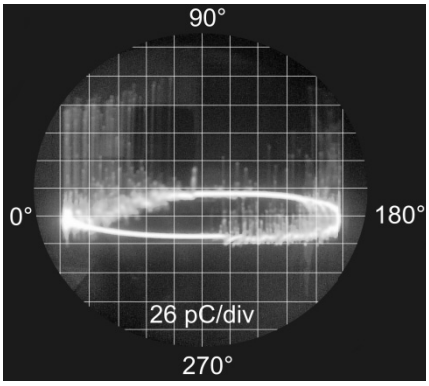

Fig. 11. Oscillogram of partial discharges obtained with classical electric method

An oscillogram of partial discharges obtained by the classical electric method is shown in Fig. 11. It can be seen that the current impulses were generated on leading edge of sinusoid positive and negative halves, which confirms that they were generated on material surface [14]. The biggest charges carried by a single discharge were up to 100 pC. The partial discharges inception voltage and flashover voltage were the lowest in the case of material with the highest measured permittivity (epoxy with 64 wt. % of the microfiller).

5. Conclusions

Doping of impregnating epoxy resin with barium titanate came out an efficient way of increasing the permittivity. Addition of 64 wt. % of micrograins of the filler caused growth of relative permittivity from less than 4 up to almost 13. Doping the epoxy resin with micrograins of barium titanate caused higher increase of permittivity than in the case of addition of nanograins. It was caused probably by the fact that micrograins were dispersed better than nanograins. An additional factor influencing the

permittivity of materials under investigation was a possibility of introducing a higher amount of micrograins (64 wt. %) than that of the nanograins (32 wt. %) of barium titanate to epoxy matrix with its impregnating properties preserved. However, the most important factor was probably the increase of the density of polymer–filler bonds in the nanocomposite, related to the growth of the matrix–filler interface. It could impede movements of chain segments and of lateral chain segments, causing the decrease of permittivity resulting in considerably higher increase of permittivity of obtained material when the microfiller was used.

The results of permittivity measurements were confirmed by the determined values of the partial discharges inception voltage and flashover voltage. In the case of microfilled epoxy resin, these two quantities measurably decreased. This means that the permittivity of this material was higher than the permittivity of remaining two ones. Basic electrical parameters, important in aspect of insulating techniques, were not considerably decreased.

Dielectric loss factor tan(δ) increased from 60×10^{-4} (epoxy without filler) to 70×10^{-4} (epoxy filled with barium titanate micrograins) or 90×10^{-4} (epoxy with barium titanate nanograins). Volume resistivity decreased by about half order of magnitude.

Acknowledgements

The researches were possible thanks to the program "Scholarship for Best PhD Students", in frames of 2.6 action of the Integrated Operational Program of Regional Development, financed in 75% from the European Union Social Fund and in 25% from the Polish National Budget.

References

[1] BROSSEAU C., TALBOT P., IEEE Trans. Diel. Electr. Ins., 11 (2004), 819.
[2] CAO Y., IRWIN P.C., YOUNSI K., IEEE Trans. Diel. Electr. Ins., 11 (2004), 797.
[3] DISSADO L.A., FOTHERGILL J.C., IEEE Trans. Diel. Electr. Ins., 11 (2004), 737.
[4] FRECHETTE M.F., TRUDEAU M.L., IEEE Trans. Diel. Electr. Ins., 11 (2004), 808.
[5] JURCZYK M., JAKUBOWICZ J., IEEE Trans. Diel. Electr. Ins., 11 (2004), 833.
[6] LEI L. and others, *Hydrophobicity of RTV Nanocomposites under Chemical Environment*, Proc. 14th International Symposium on High Voltage Engineering (ISH'2005), Beijing, China, D-22.
[7] LEWIS T.J., IEEE Trans. Diel. Electr. Ins., 11 (2004), 739.
[8] ORŁOWSKA S., BEROUAL A., FLESZYŃSKI J., J. Phys. D: Appl. Phys. 35 (2002), 2656.
[9] ORŁOWSKA S., BEROUAL A., FLESZYŃSKI J., J. Phys. D: Appl. Phys. 35 (2002), 3101.
[10] ORŁOWSKA S., *Dielectric Composite Materials Characterisation Using Boundary Integral Method*, XI Int. Workshop on High Voltage Engineering, Karpacz, 2002, 23.
[11] ROY M. and others, IEEE Trans. Diel. Electr. Ins., 12 (2005), 629.
[12] MORAŃDA H., SZTOLCMAN M., WALCZAK K., MOŚCICKA-GRZESIAK H., *Enlargement of Fingerprint in Procedure of Defects Recognition in Oil-Paper Insulation Using Time Parameters of PD*, Proc. 14th Int. Symp. High Voltage Engineering, ISH '05, Beijing, China, G-056, 2005.
[13] SIKORSKI W., SIODŁA K., *Identification of Partial Discharge Sources in High Voltage Insulating Systems Using Acoustic Emission Method*, Proc. 14th Int. Symp. High Voltage Engineering, ISH '05, Beijing, China, G-009, 2005.

Received 2 July 2007
Revised 22 August 2007

Materials Science-Poland, *Vol. 27*, *No. 4/2*, *2009*

Application of the FDS method for assessment of HV epoxy–mica–glass insulation

J. SUBOCZ*

West Pomeranian University of Technology, Szczecin

The mechanism of degradation of epoxy–mica–glass insulation has been investigated as well as its kinetics depending on service conditions. The most important factor there is production quality. Basics of dielectric spectroscopy in time and frequency domain and application of this method for estimation of HV insulation condition were described. Research conducted on insulation models showed that good indicators of insulation conditions are the value of charge and time of relaxation in low frequencies range. An example of application of FDS measurements was given for estimation the quality of technology in postproduction tests. The method is very accurate and allows identifying defective production technology and insulation aged in service.

Key words: *epoxy–mica–glass insulation; FDS; quality test*

1. Introduction

The most commonly applied insulation structure in HV machines is thermosetting composite epoxy–mica–glass. Depending on the technological advancement of a producer, this composite is manufactured in the processes of impregnating successive layers of mica and glass mat with epoxy resin or vacuum pressure impregnation (VPI). Most difficulties in achieving the appropriate quality of the final product are in processing technology. To the most frequent defects belong gas caverns in an insulation volume, insufficient adhesion of a resin to fibreglass and mica or improperly cross-linked resin.

Measurements of long-time dielectric strength of composite layer insulation show that even using materials of a very good quality cannot guarantee long period of insulation operation if proper processing methodology has not been applied [1]. The presented examples (Fig. 1) confirm observations that first inclusions appear during the production process. Their number and geometry depend on production technology and

*E-mail: jan.subocz@ps.pl

its quality [2]. In the first case (VPI – Fig. 1a) the most common defect is delamination of interface resin–glass or mica. On the other hand, in impregnation technology the usual defect is formation of inclusions (Fig. 1b). The other kinds of defects, also having a vital role, appear in the structure of resin reinforcement interface and result from physicochemical phenomena during cross-linking process.

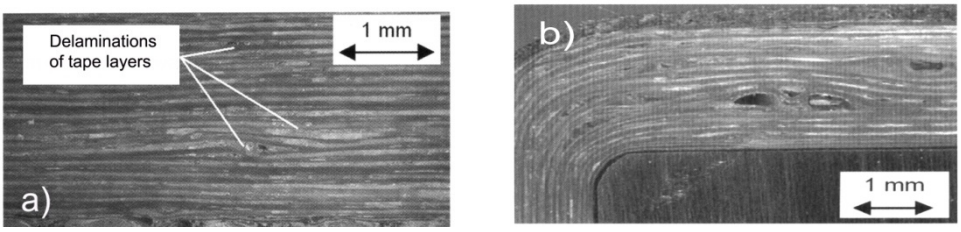

Fig. 1. Examples of improperly manufactured HV composite insulation [1]

Quite complicated process of fabrication of insulation (e.g., the VPI method) may lead to formation of "rubber" regions between the polymer liquid and completely polymerised area. These regions stop the resin from flowing into free spaces of reinforcement. This situation, characteristic of the first stage of polymerisation, is irreversible [3].

A typical property of all kinds of composite insulations are internal mechanical stresses. They can be formed during natural matrix shrinkage, during gelation but also due to differences in thermal expansion of the matrix, reinforcement or filler. For example, in fibreglass–resin structure, cutting tensions for 115 °C reach the value of ca. 20 MPa [4]. It was found [5] that during cooling down a composite from curing to room temperature, for ca. 1 μm distances between fibres, stretching stresses appear with the values up to 50 MPa, which are higher than the composite strength. Internal mechanical stresses are located mainly in the interface, which usually is the first place where cracking starts, even for small distances between fibres. According to many authors, the interface is the weakest point of the insulation structure, where environmental exposure is concentrated [6]. The influence of internal mechanical stresses on degradation of fibreglass based insulation was emphasized. Even small mechanical stresses, up to 10% of the permissible value, can lead to initiation of partial discharges (PD) [7].

2. Methods for production quality assessment

Understanding phenomena described above allows one to search for the best methods of identification of the interface condition and assessment of resin cross-linking level, both in the stage of production optimisation and quality control. Standard measurement techniques, used for many years, allow cavern detection (PD) or

completely wrong resin processing (measurements of tanδ, insulation resistance, voltage test). In the case of assessing resin cross-linking level, an unambiguous method is the differential calorimetric analysis (DSC). By this method, the thermal capacity ΔC_p and glass transition temperature of polymer matrix T_g may be determined. Both of these parameters are strictly connected to morphological structure of the resin and contain information on the hardener selection and the level of reaction between the hardener and resin. For instance, in properly manufactured epoxy insulation of the B class, the glass transition temperature T_g is in the range 145–155 °C. For classes F and H these values are 185–190 °C and 210–215 °C, respectively. The obvious disadvantage of DSC measurements is necessity to take material samples from final products. Recently a method of identification of viscoelastic phase and space charge in the interface of composite insulation, based on dielectric relaxation measurements in ultralow frequencies (FDS) or in very long times (PDC) [8]. The basis for these methods is modified equivalent circuit of insulation, which consists of one relaxation structure in the range of high frequencies and of two such structures in medium (C_{MF}) and low (C_{LF}) frequencies (Fig. 2).

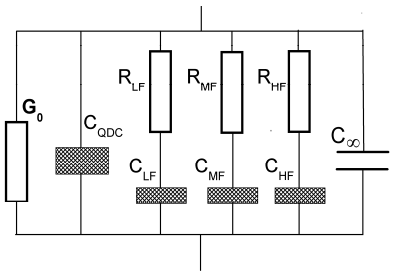

Fig. 2. The equivalent circuit of a composite insulation

In most cases, the dipole relaxation in composites of high molecular mass and apparent phase boundary proceeds at asymmetric or continuous distribution of time constants, in accordance with Jonscher's universal response or the Havriliak–Negami (H–N) laws [9, 10]. On the other hand, the measurements of PDC in those laminar materials have proved that the distribution, following the fractional exponent law $i(t) \propto t(-n, -m)$ [8], always accompanies relaxation processes. Thus, to reflect the nature of the processes, the equivalent insulation composite model (Fig. 2) should have capacitors CLF, CMF and CHF, which should satisfy the dipole relaxation requirements by Jonscher. Nonetheless, the loss capacity CQDC represents the DC response according to Jonscher.

In the frequency domain, the equivalent circuit in Fig. 2 can be described with the Havriliak–Negami function as follows [10]:

$$\varepsilon^*(\omega) = \sum_{k=1}^{3} \frac{\Delta\varepsilon_k}{\left(1+(\omega\tau_k)^{\alpha_k}\right)^{\beta_k}} + \varepsilon_\infty - j\left(\frac{\sigma}{\omega\varepsilon_0}\right)^N \tag{1}$$

where: $\varepsilon^*(\omega)$, ε_∞ are the complex and optical dielectric permittivity, $\Delta\varepsilon$ – polarizability, σ_0 – dc conductivity, τ – relaxation time, α, β, N – constants, ω – pulsation.

The theoretical grounds of the application possibility of the H–N equation to the analysis of relaxation processes in thermosetting composites in LF and MF range are given in [8]. Based on the model investigations, the criteria for the assessment of the epoxy–mica–glass insulation quality with use of FDS measurements have also been presented there. Values of times τ_{LF}, τ_{MF}, dispersion of relaxation times α_{LF}, α_{MF}, polarizability $\Delta\varepsilon_{LF}$, $\Delta\varepsilon_{MF}$ and conductivity σ_0 are basic coefficients characterizing insulation. The hardening level of a resin and the presence of the viscoelastic phase can be identified based on the coefficients τ_{LF}, α_{LF}, $\Delta\varepsilon_{LF}$. In the case of resin hardened improperly, when viscoelastic phase occurs, usually short times of the relaxation are obtained ($\tau_{LF} < 400$ s) with relatively large values of the coefficients α_{LF}, $\Delta\varepsilon_{LF}$ ($\alpha_{LF} \geq 0.6$). However, the aged resin is characterized with high polarizability $\Delta\varepsilon_{LF}$ and a wide dispersion of the relaxation times (α_{LF} between 0.1 and 0.3). Viscoelastic phase, large inhomogeneity and delamination are associated with the space charge which can be characterized by the relaxation times on the level of several tens of seconds and the dispersion coefficient α_{MF} in the range 0.5–0.9.

Application of Eq. (1) for assessment of composite insulation manufacturing quality needs measurements of capacitance C_{coil} and losses coefficient $\tan\delta$ of windings in the frequency range 0.1 mHz–100 Hz. Then, by the analysis of the characteristics of electric permittivity of the insulation ($\varepsilon' = C_{\text{coil}}/C_0$) and analysis of its losses ($\varepsilon'' = \varepsilon'\tan\delta$), dipoles and space charge relaxation time τ, polarizability $\Delta\varepsilon$, and conductance σ are determined.

3. Experiences in assessment of the epoxy–mica–glass insulation

3.1. Assessment of insulation of 6 kV motors stator coils

Application of FDS and PDC measurements for assessment of quality of final products may be presented on an example of epoxy–mica–glass insulation of 6 kV motor stator coils. It was the layer epoxy–mica–glass insulation and the coil had been delivered to recipient within the order on larger quantity. The analysis of the real and imaginary part of complex permittivity, based on Eq. (1), showed that in the range 10^{-1}–10^{3} Hz large relaxation structure can be found, which predominates high and low frequency relaxations. Calculated relaxation parameters ($\tau = 0.023$ s, $\alpha = 0.21$, $\beta = 0.79$, $\sigma = 1.2\times10^{-16}$ S/m) prove, that these are dipole processes of the H–M model with wide and asymmetrical dispersion. The value of time constant τ indicates that this relaxation structure is a large viscoelastic phase, as β relaxation of hardened resin is in the range 10^{-6}–10^{-8} Hz, while time constant of space charge polarization in the phase interface is ca. 10^{1}–10^{3} s.

In inappropriately cured thermosetting composites chemical reactions may occur. They are very slow and can last even for a few years. Taking above under consideration, the coil was tested again after 18 months of the seasoning at ca. 20 °C and rela-

tive humidity $RH \approx 70\%$. The analysis of losses ($\varepsilon'' = f(f)$) showed that in the insulation a space charge appeared, with the relaxation time $\tau \approx 27.5$ s (Fig. 3). Its value was so high, that it had prevailed over other relaxation processes.

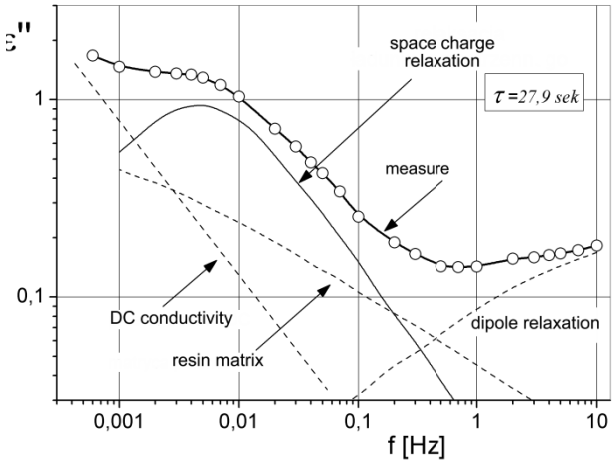

Fig. 3. Analysis of losses characteristic of
6 kV motor coil after 18 months of seasoning

Based on technological processes, discussed above, it can be assumed that this relaxation comes from heterocharge in the interface, generated due to delamination or chemical corrosion. The conclusion can be drawn that mounting this coil in a motor would lead to significant decreasing its lifetime. Service experiences show that a few hard starts of a motor connected with increase temperature of insulation up to 150 °C is enough for insulation failure.

3.2. Assessment of insulation of 15.75 kV generator stator bar

Epoxy–mica–glass insulation manufactured by the MICADUR method has been assessed, taken from stators bars of 230 MVA, 15.75 kV generator. The following samples were examined:

- sample A – a new winding bar ready to be installed in a generator,
- sample B – a bar with regenerated insulation. It had been operated for several years and had its antiarcing layer mechanically removed, insulation losses filled up with chemosetting epoxy composite and new antiarcing layer put on it,
- sample C – a bar from stator winding, operated for several years.

In a new insulation of a generator bar (Fig. 4, sample A) in VLF range the relaxation with time constant $\tau_{LF} = 3.4 \times 10^4$ s has been observed. The model research [8] and parameters α_{LF} 0.35, β_{LF} =1 derived from Eq. (1) show that this is VLF dielectric response resulting from current flow and ion mass transport. High value of time constant τ_{LF} and low

conductivity $\sigma = 1.1\times10^{-16}$ S/m indicate that in VLF range there is no space charge relaxation or free terminal groups of resin and hardener, which have not gone through reactions. The high value of polarizability ($\Delta\varepsilon_{LF} = 5.35$) usually occurs in disordered structures which is typical of a new epoxy–mica–glass insulation system in which no relaxation of physical structure takes place. This kind of relaxation consists in decreasing free spaces between molecules and improving polymer structure without chemical changes. All these parameters lead to conclusion that insulation from sample A has attributes of a new, properly manufactured composite insulation with correct structure of resin–reinforcement interface, without delamination and presence of unreacted terminal groups of the resin and hardener.

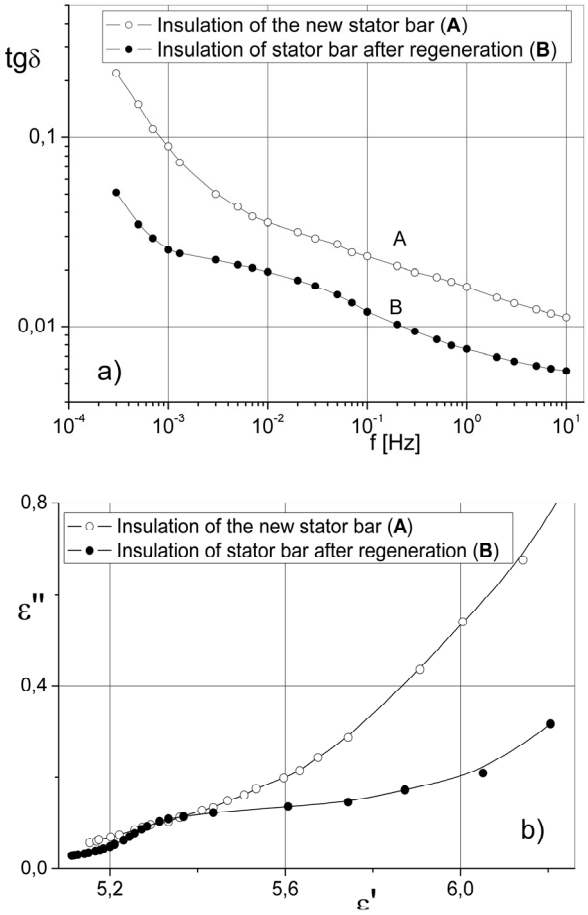

Fig. 4. Loss factor vs. frequency and the Cole–Cole relationships for the new stator bar (A) and the bar after regeneration (B)

In the case of regenerated insulation (Fig. 4, sample B) in the MF range relaxation was observed with the parameters $\tau_{MF} = 43$ s, $\alpha_{MF} = 0.64$, $\beta_{MF} = 1$, $\Delta\varepsilon_{MF} \approx 0.7$, which

comes from space charge. It is probably located in the interface between existing epoxy–mica–glass composite and the new layer of insulation, or it may be a result of improper hardening of the chemosetting resin during regeneration. In both cases, such a charge may lead to electrical treeing after long period of operation. Therefore, in this case it is recommended to control quality of insulation after next 1.5–2 years of operation with application of FDS or PD measurements.

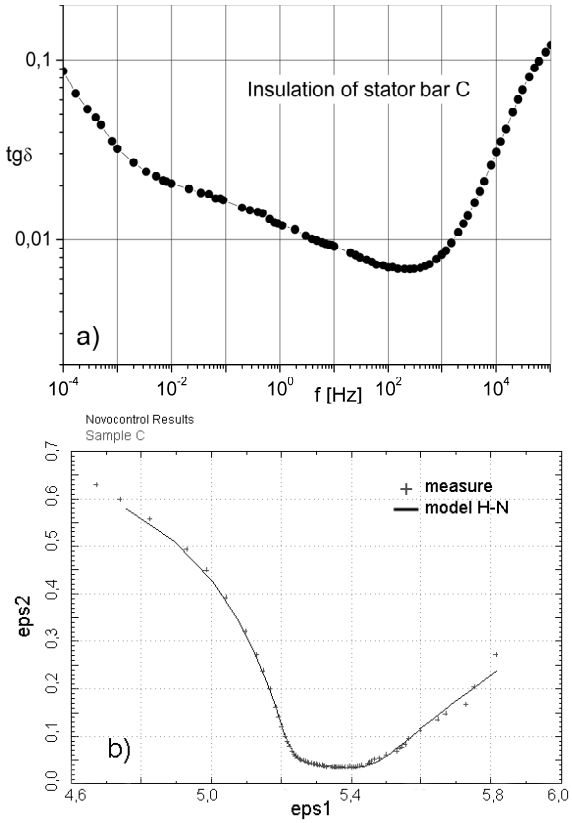

Fig. 5. Loss factor vs. frequency (a) and the Cole–Cole relationships (b) for the stator bar C

In FDS measurements for insulation from exploited generator bar (Fig. 5, sample C) taken in the frequency range 0.1 mHz–1 MHz, two main relaxation processes were found.

The former one occurs in the VLF range, with the parameters $\tau_{LF} = 5.3\times10^3$ s, $\alpha_{LF} = 0.47$, $\beta_{LF} \approx 1$, $\Delta\varepsilon_{LF} \approx 1.46$ similar to relaxation observed in sample A and in previously obtained results for generator bar insulation after four years of operation [11]. The analysis of these results leads to conclusion, that in sample C structure changes took place, typical of the early period of ageing, when resin structure is getting physi-

cally stabilized and mechanical parameters are improved without any chemical reactions.

The other process occurring in the HF range, linked with β relaxation of the resin, is influenced mainly with side groups, ion contaminations contained in unreacted resin and hardener. Very short relaxation times and relatively low polarizability ($\tau_{HF} = 3.9\times10^{7}$ s, $\alpha_{HF} == 0.7$, $\Delta\varepsilon_{HF} \approx 1.9$) suggest that in this case dominating compounds are side groups linked with resin without interaction from unreacted terminal groups of resin and hardener. It can be concluded that in sample C polymer matrix is properly hardened and in the insulation no space is present in resin–reinforcement interface or amorphous phase with high polarizability, typical of deteriorated resin. It should be pointed out that these conclusions have been verified with MDSC and DTMA tests.

Differences in relaxation processes in samples A and C result mainly from physical stabilization of insulation structure in sample C under vibrations and higher temperature of operation (ca. 50 °C).

References

[1] VOGELSANG R., WEIERS T., FRÖHLICH K., BRÜTSCH R., EEE Electr. Insul., 22 (2006), 5.
[2] KAUFHOLD M., SCHÄFER K., BAUER K., BETHGE A., RISSE J., *Interface Phenomena in Stator Winding Insulation – Challenges in design, Diagnosis, and Service Experience,* IEEE Electr. Insula. Mag., 18, (2002), 27.
[3] NAKAMURA Y., YAMAGUCHI M., KITAYAMA A., J. Appl. Polym. Sci., 39 (1990), 1045.
[4] OCH M., YAMASHITA K., SHIMBO M., J. Appl. Polym. Sci., 43 (1991), 2013.
[5] TROTIGNON J., VERDU J., *Comparative study of flexural fatigue properties of epoxy and PEE composites and matrices*, T. Chandra, D. Dhingra (Eds.), Advances Composites 93, The Minerals, Metals and Materials Society, 1993.
[6] TANAKA T., IEEE Trans. DEI, 9 (2002), 704.
[7] SCHRIJVER C., HERDEN A., KÄRNER H., *Fundamental Ageing Mechanisms of Fibre Reinforced Polymer (FRP) Insulators,* 10th ISH, Montreal, 1997.
[8] SUBOCZ J., *Wybrane zagadnienia przewodnictwa i relaksacji dielektrycznej w aspekcie diagnostyki izolacji kompozytowej*, Prace Naukowe Politechniki Szczecińskiej nr 580, Szczecin, 2003.
[9] JONSCHER A.K., IEEE Trans. El. Insul., 27 (1992), 407.
[10] HAVRILIAK S. Jr., HAVRILIAK S.J., *Dielectric and Mechanical Relaxation in Materials. Analysis, Interpretation, and Application to Polymers*, Hanser Publishers, Munich, 1997.
[11] SUBOCZ J., *Relaxation spectroscopy in generators winding insulation,* Przegl. Elektr., Special Issue, (2001), 314–317.

Received 2 July 2007
Revised 22 August 2007

Materials Science-Poland, *Vol. 27*, *No. 4/2*, *2009*

Method of assessment of varnishes modified with nanofillers

B. GÓRNICKA*, L. GÓRECKI

Electrotechnical Institute Division of Electrotechnology and Material Science, Wroclaw, Poland

The method of analysis and assessment of the results of investigations of nanofilled varnishes used for electrical insulation have been presented. The proposed method enabled consideration of an effect of the coating thickness. The investigation indicated that improving of the bond strength depends on loading and the size of nanoparticles. The method of fabrication of composites with nanoparticles has an influence on their properties. Composites with fumed silica showed improved dielectric properties. Absorption of water of all formulated varnishes with nanofillers decreases provided that some additives were incorporated.

Key words: *impregnating varnish; nanofiller; bond strength; pulse resistance; electrical strength; water absorption*

1. Introduction

Incorporation of a small quantities of nanoparticles into a polymer dielectric changes its properties. If the size of particles of the incorporated filler approaches that of the polymer chain length, the particle stop to behave like foreign inclusion; space charge densities are very small and the Maxwell–Wagner interfacial polarization is negligible [1–6].

The impregnating varnishes used for electrical insulation modified due to improving their properties with various kinds of nanofillers were investigated. When analysing the properties of varnishes modified with nanofillers it should be considered many affecting factors, e.g.: a stage of curing (if nanofilled varnishes which showed higher thermal endurance need to be cured in higher temperatures), an obtained thickness of coating (how adding of a nanofiller influences the thickness of coating and other properties connected with the thickness), methods of fabrication of nanoparticles and loading, methods of dispersing in varnish.

*Corresponding author, e-mail: gornicka@iel.wroc.pl

2. Experimental

Two kinds of impregnating electroinsulating varnishes based on polyester (PE) and polyesterimide (PES) resins were modified by incorporating 1–3% of two kinds of nanosilica – fumed nanosilica with average grain size 7 nm and nanospheres of silica with diameter ca 400 nm, zinc oxide, titanium dioxide, and montmoryllonite. The composites were formed utilizing various methods of dispersing. The properties of pure and nanoparticle filled varnishes were compared.

Three types of samples were used: steel panels coated by varnish (acc. to EN 60455-2) for determination dielectric properties, helical coils (according to EN 61033) for measurements of bond strength of impregnating varnish to an enamelled wire substrate and the cast pieces of varnish (according to EN 60455-2) for water absorption testing.

3. Results

3.1. Loading of the nanofillers

The bond strength at higher temperatures of base varnish PES and 1 to 1.5% fumed nanosilica loaded composite is shown in Fig. 1. Improving of its bond strength at higher temperatures is up to ca. 20% and 30%, respectively.

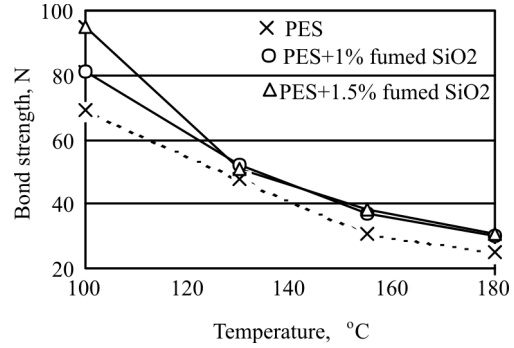

Fig. 1. Temperature dependence of the bond strengths in pure PES and PES filled with 1.0% and 1.5% of fumed nanosilica

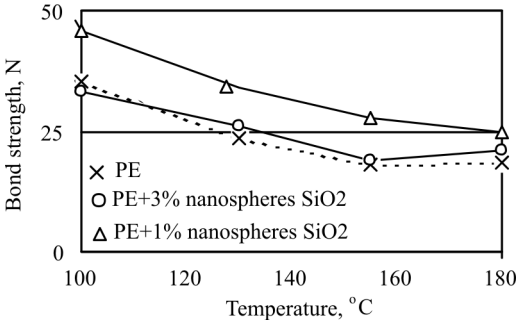

Fig. 2. Temperature dependence of the bond strengths in pure PE and PE filled with 1% and 3% of silica nanospheres

At 1% loading of nanospheres of nanosilica, the bond strength of nanofilled PE varnish is almost not changed while at 3% loading improving of this properties is significant, i.e. above 40% (Fig. 2). Thus the larger particles need higher loading (3%) to improve their properties.

3.2. Thickness of coating

Some of the properties of electroinsulating varnishes, e.g. a breakdown voltage, electrical strength or resistance to impulse voltage, strongly depend on the obtained thickness of coating. Therefore exceptions from these proportionalities could be considered as change of a feature of the material. An example of dependence of the time of life under pulse voltage on the insulation thickness for series of various composites of PE varnish with nanofillers is presented in Fig. 3. The same dependence for series of nanofilled PES varnishes but after rejecting of three composites with abnormal high endurance is shown in Fig. 4. These rejected composites, two with nanosilica and one with zinc oxide demonstrated improved impulse voltage endurance. For the three composites the "barrier effect" for partial discharges erosion was obtained and the pulse voltage endurance were from 10 to 100 times higher than those for a standard composite.

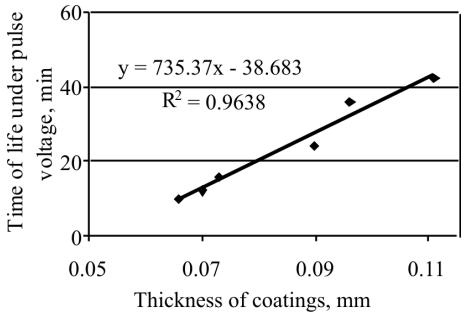

Fig. 3. Dependence of the time of life under pulse voltage on the thickness of coating for various nanofilled PE varnishes

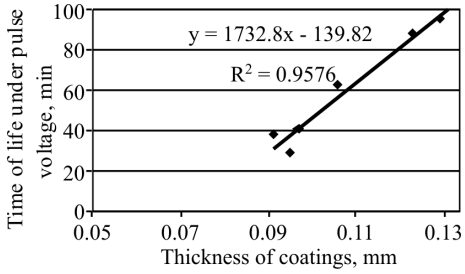

Fig. 4. Dependence of the time of life under pulse voltage on the thickness of coating for various nanofilled PES varnishes after excluding of 3 compositions

Due to difference thickness effect from nanofiller effect a similar analysing of the electrical strength was conducted. Linear coefficients of correlation between electrical strength and thickness of insulation have been calculated. The results of testing PE based varnishes with and without nanofillers are presented in Table 1.

Table 1. The results of testing of electrical strength of pure (No. 1) and nanofilled PE varnish

No.	Thickness of coating [mm]	Dielectric strength [kV/mm]		
		23 °C	155 °C	180 °C
4	0.054	109.4	78.8	69.6
11	0.057	103.7	99.5	93.1
1	0.061	104.3	90.9	67.1
5	0.062	96.2	68.5	65.3
12	0.064	105.3	70.3	67.5
7	0.066	104.1	96.3	75.3
3	0.066	108.9	71.9	64.0
2	0.077	89.9	66.9	64.7
14	0.083	92.2	35.5	23.9
13	0.094	84.8	44.5	30.9
Coefficient of correlation between dielectric strength and thickness	all composites	–0.86	–0.80	–0.84
	all except No. 5	–0.92	–0.82	–0.84
	all except No. 7	–0.87	–0.84	–0.85
	all except Nos. 5 and 7	–0.92	–0.86	–0.85

Table 2. The results of testing of electrical strength of pure and nanofilled PES varnish

No.	Thickness of coating [mm]	Dielectric strength [kV/mm]		
		23 °C	130 °C	180 °C
1	0.084	78.4	82.6	70.2
5	0.091	96.2	78.4	77.6
2	0.092	76.7	61.0	50.2
7	0.096	86.6	72.7	66.1
3	0.101	80.3	67.7	60.7
4	0.101	81.5	65.3	60.7
8	0.170	66.7	44.5	42.2
6	0.178	67.0	41.8	38.8
Coefficient of correlation between dielectric strength and thickness	all composites	–0.77	–0.92	–0.84
	all except No. 5	–0.87	–0.92	–0.87
	all except No. 2	–0.83	–0.97	–0.95
	all except No. 5 and 2	–0.91	–0.97	–0.99

In the presented results, sample No. 5 (with TiO_2nanoparticles) showed abnormal low electrical strength while sample No. 7 (one from the samples with fumed SiO_2) showed improving of this property. The same calculation for series of PES varnish is presented in Table 2. After excluding samples No. 2 (with ZnO nanoparticles) and

No. 7 (one from the samples with fumed SiO_2), the coefficient of correlation considerably increases.

3.3. Absorption of water

Incorporation of nanofillers to varnish should diminish its liquid and gas permeability due to the barrier effect. Our examination of water absorption of nanofilled electroinsulating varnishes demonstrated that the method of fabrication of a composite influences its properties. The composites were prepared using various methods of nanoparticle dispersing – with an ultrasonic homogeniser (h) and a disperser (d). In some experiments, the nanoparticles were prearranged by milling (m) as well some additives were added, an air releaser (b) among others. The composites containing the air releaser (b) showed lowered water absorption (Figs. 5 and 6).

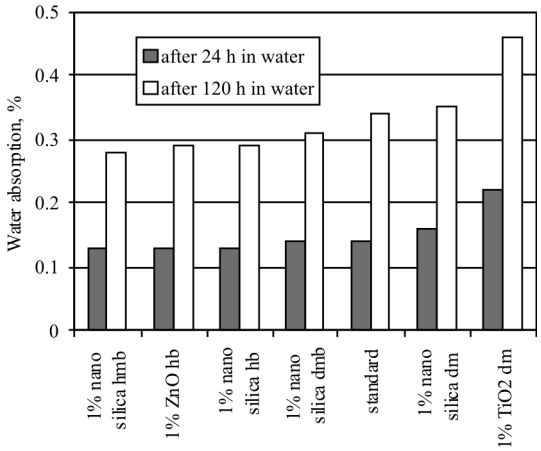

Fig. 5. Absorption of water for PE varnish with nanofillers

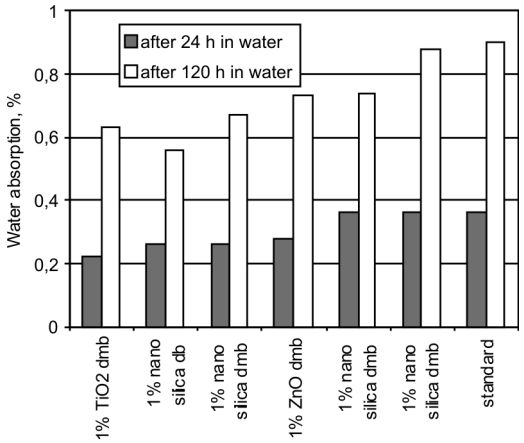

Fig. 6. Absorption of water for PES varnish with nanofillers

4. Conclusions

Impregnating electroinsulating varnishes based on polyester (PE) and polyesterimide (PES) resins have been invrestigated with various nanofillers (nanosilica, metal oxides and montmoryllonite), formed utilizing various methods of dispersing. Improving the bond strength depends on the size of nanoparticles and their contents; larger particles need higher loading. The method of analysis of the results enabled consideration of the thickness of the coating effect. Some composites with nanosilica showed much better resistance to pulse voltage and slight increasing in electric strength, especially at raised temperatures. The nanocomposites containing the air releaser showed lowered water absorption.

References

[1] FOTHERGILL J.C., DISSADO L.A., *Nanocomposite Materials for Dielectric Structures*, http://www.le.ac.uk/eg/research/groups/power/highvolt/Nelson/final%20report2.pdf.

[2] TANAKA T., KOZAKO M., FUSE N., OHKI Y., IEEE Trans. Diel. Electr. Insul., 12 (2005), 669.

[3] ROY M., NELSON J.K., MACCRONE, L.S. SCHADLER, REED C.W., KEEFE R., ZENGER W., IEEE Trans. Diel. Electr. Insul., 12 (2005), 629.

[4] TANAKA T., MONTANARI G.C., MÜLHAUPT R., IEEE Trans. Dielectr. Electr. Insul., Vol. 11 (2004), 763.

[5] NELSON K., UTRACKI L.A., MACCRONE R.K., REED C.W., *Role of Interface in Determining the Dielectric Properties of Nanocomposites*, http://www.rpi.edu/~nelsoj/ceidp04a.pdf.

[6] RÄTZKE S., KINDERSBERGER J., *Erosion Behaviour of Nano Filled Silicone Elastomers*, Proc. XIV Inte. Symp. High Voltage Engineering, Tsinghua University, Beijing, China, August 25–29, 2005, http://www.hsa.ei.tum.de/Publikationen/2005/05_rae_2. pdf.

Received 29 May 2007
Revised 13 March 2007

Materials Science-Poland, *Vol. 27*, *No. 4/2*, *2009*

Modification of the composition and technology of the processing of ceramic-polymer insulators

Z. ŚWIERZYNA[1*], G. PAŚCIAK[1], B. MAZUREK[1], J. OLEJNIK[2],

[1]Instytut Elektrotechniki, Oddział Technologii i Materiałoznawstwa Elektrotechnicznego, ul. M. Curie-Skłodowskiej 55–61, 50-369 Wrocław, Poland

[2]NTI-POMIARY Sp. z o. o. ul. Portowa 1, 67-200 Głogów

The nanosized filler influence on the physicochemical and electrical properties of the composite ceramic-polymer (CP) material to be applied in outdoor line HV insulators has been investigated. Also the results of the electrical and mechanical examinations of the CP insulators moulded with the use of the dies made of PET have been presented. As a standard, the moulds for flask – moulding are made of PP material what, because of its high adhesion causes some difficulties during forming of insulator and leads to deteriorating the quality of the insulator surface.

Key words: *electric insulation; composites; polymer materials; testing*

1. Introduction

Polymer concrete composites (ceramic-polymer, CP) were developed in 1960 –1970 in USA and Japan [1]. Since 1980 their insulating power is exploited in both indoor and outdoor high-voltage insulators to which they proved suitable equally to glass and ceramic [1, 2]. They are mounted on power lines in many countries. Up to now ceramic-polymer insulators are made in USA by ABB. In Poland, the original recipe of CP composite was developed and patented in 1996 and applied for processing of post-insulator cores by dust pressing method [3, 4, 5, 8]. The cores were suitable both with housings made of the same PC material and with silicon elastomer housings. In turn, the NTI-Pomiary Sp. z o.o. from Głogów applied this polymer concrete material for processing post- and pull- (line and station class) indoor and outdoor insulators [9] (Figs. 1–3). CP insulators are characterized by good mechanical durability and resistance to mechanical hazard during transportation, mounting and exploitation. The surface of insulator housing is hydrophobic and does not need any covering with glaze and clamps directly bonded to the insulator body. As they provide uniform dielectric on HV terminations at the reduced costs, they can be successfully and safely used to replace the porcelain.

*Corresponding author, e-mail: swierzyna@iel.wroc.pl

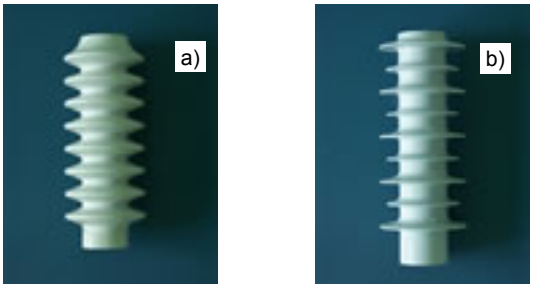

Fig. 1. Ceramic-polymer composite station class post insulators: a) H6-125-II-CP; b) H6-125-II-CP with silicone rubber covering, inner clamps galvanized, M12

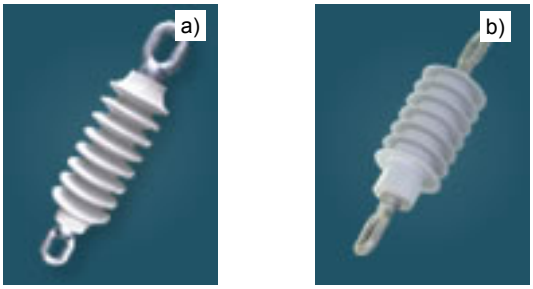

Fig. 2. Ceramic-polymer composite line strain insulators: a) L-CP-60, b) L-CP-60 with silicone rubber covering; inner clamps: steel, twisted-in handle M16

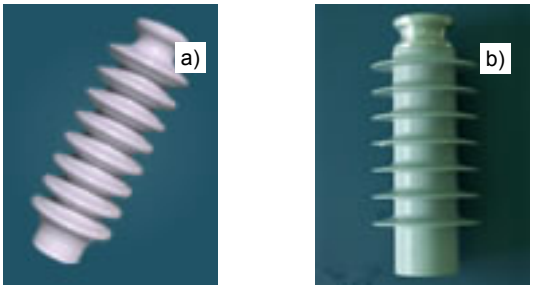

Fig. 3. Ceramic-polymer composite line post insulators: a) LW-CP 8/24, b) LW-CP 12/24; inner clamps: galvanized, M16

2. Ceramic-polymer composite

Ceramic-polymer composite constitute binder (5–30%) and mineral fillers (70–95%). Binder is composed of organic resin (monomeric or polymer), some amount of improves and promoters of resin curing. Typically polyester, polymethacry-

late or epoxy resins are used. As a filler, usually quartz powder with strictly selected sizes of grains is applied. Chemical merit of these polymer composites constitute esters of acrylic and methacrylic acids. The key component of these acids is methyl methacrylate. The process of composite curing starts after addition of curing agent which initiates polymerization at room temperature, without the necessity of heating the mixture. The end product has reproducible parameters. Owing to long C–C–C carbon chains formed during resin curing, the composite is resistant to weather and other ageing agents, which makes it attractive alternative to porcelain in application for outdoor insulators [6]. Electrical and mechanical properties of the developed composite were tested. The testing was carried out on both material specimens and products, i.e. on models of insulators.

3. Moulds for ceramic-polymer insulators

Corrosivity of methacrylate compositions, oxygen inhibition and 6% volume shrinkage, all of them are against using traditional metal moulds for moulding composite insulators. That is why those insulators or their cores were fabricated with the use of expendable moulds made of polypropylene (PP) foil (Fig. 4). Insulators made with those moulds have dull, lustreless surface, thus installing them outdoor in hostile, contaminated environment requires covering them with thin silicone films. This work was focused on developing the method of fabrication of CP insulators suitable for installation in hostile environments (II and III contamination zones) without covering with additional protective films. Polyethylene terephthalate (PET) foil was used for fabrication of moulds. Comparing to PP foil, the PET foil is characterized by better wettability and during exothermal process of curing the composite closely contacts with its walls, producing smooth, lustre surface of insulators. IEL OTiME was in position of applied of PET foil for fabricating moulds (Fig. 5) only because its employees managed to master the difficult technology of processing characteristic shapes of insulator shed.

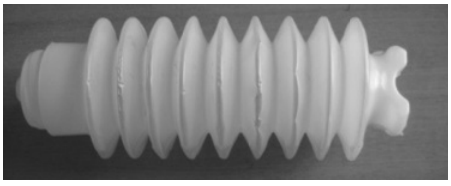

Fig. 4. PP mould for CP insulator

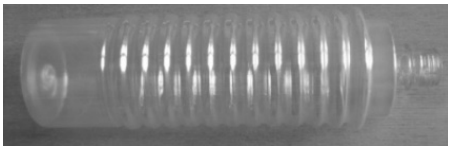

Fig. 5. PET mould for CP insulator

4. Examination of ceramic-polymer composites

4.1. Test specimens

Two polymer-concrete composites based on methacrylate resins were developed to execute specimens and models of insulators (Table 1). The composites differed in mineral filler improving physical properties of insulators. Composite 2 contained a filler with nonosized grains (aerosil 150).

Table 1. Compositions of polymer concretes based on methacrylate resins

No.	Constituent	Composite 1 [g]	Composite 2 [g]
1	binder: methyl methacrylate	500.0	500.0
2	promoters of resin curing	5.0	5.0
3	mineral filler 1– SiO_2	2500.0	2497.0
4	nanofiller – aerosil 150	–	3.0
5	UV stabilizer: TiO_2 and other additives	42.8	42.8
6	adhesive agent	3.5	7.6

4.2. Methacrylate based CP composites resistant to electric arc

Methacrylate based CP composites were tested for resistance to electric arc according to PN-74/E-04441 [10]. The testing was performed on a test stand which enabled one to apply to dielectric, insulating material the 12.5 kV test voltage. The moments ignition and extinction of arc were observed as well as the specimen appearance. The times of arc duration are given in Table 2. The specimens after testing are shown in Fig. 4.

Table 2. Resistance to electric arc of methacrylate-polymer concretes; mean time between the arc ignition and intensive erosion of electrical insulating material of 10-point specimen [s];

Composition with a standard filler	Composition with a nanosized filler
258	260

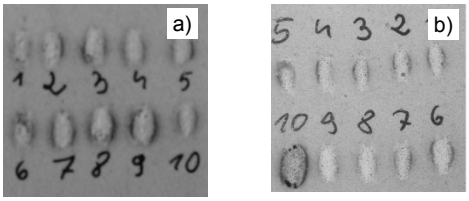

Fig. 6. Methacrylate based CP specimen after testing for resistance to electric arc: a) compound 1, b) compound 2

As can be seen in Fig. 6, the specimen material experienced extensive erosion due to formation of an electric path and increase of electric current in transformer secondary circuit.

4.3. Resistance of methacrylate resin based CP composites to tracking current

For comparison, both methacrylate based CP compositions were subject to testing for resistance to tracking as per PN-89/E-04442 [12]. The test was performed on flat inclined specimen under high voltage as specified in aforementioned standard. According to this standard, the class of material is determined by the highest voltage withstood by specimen for 6 h. To perform the test, the specimen (Fig. 7) was placed in testing chamber and then the highest allowed 6 kV test voltage was applied and maintained constant for 6 h. During testing, the bottom of the specimen was wetted with 0.1% NH_4Cl contaminant (resistivity of 370–400 Ω·cm). The contaminant was fed at a uniform rate of 0.6 cm^3/min. The test results and the mean value of the current flowing in the high voltage circuit are given in Table 3. As during that time no breaks of electric circuit occurred, the composites were evaluated as tested positive for resistance to tracking. The specimens after testing are shown in Figs. 8 and 9.

Fig. 7. Electrodised specimen during testing for resistance to tracking currents

Fig. 8. The methacrylate CP specimen after testing for resistance to tracking at 6 kV

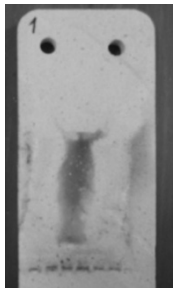

Fig. 9. The specimen of methacrylate CP with nanofiller, after testing for resistance to tracking at 6 kV

Table 3. Resistance of methacrylate CP composites to tracking performed at inclined specimen and high voltage

Material No.	Test voltage [kV]	Test duration [h]	Mean current [A]	Evaluation
1	6	6.0	0.017	positive
2	6	6.0	0.015	positive

4.4. Testing of methacrylate resin based CP composites for water diffusion

Both CP composites were subject to testing for water diffusion as per PN-IEC 61109:1999 [12]. The samples were drawn in groups of six by cutting out 6 specimens from each material. Then they were immersed in a 0.1% NaCl water solution for 100 h. Then the specimens were subject to testing for 12 kV withstand voltage for 1 min. No breakdown or flashover was allowed during the testing and the leakage current was to be lower than 1 mA. Results of testing for water diffusion are presented in Table 4.

Table 4. Results of testing for water diffusion

Tested material	Leakage current [mA]	Evaluation
Composition 1	< 0.1	Positive
Composition 2	< 0.1	Positive

4.5. Testing of methacrylate resin based CP composites for liquid absorption

Both CP composites were subject to testing for liquid absorption as per PN-IEC 383-1:1997 [13]. The fragments of insulator body were immersed in a 1% solution of fuchsine in alcohol. The solution was maintained at the pressure of 15 MPa for 12 h. Then the fragments were taken from the solution, washed in water, dried and broken. No signs of penetration of the dyestuff were visible on freshly fractured surfaces (Fig. 10).

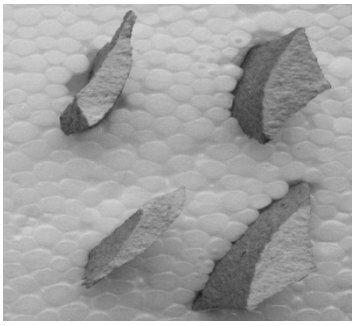

Fig. 10. Fragments of insulator after testing for liquid absorption

5. Testing of ceramic-polymer composite insulator units to PN-EN tests specifications

Methacrylate resin based ceramic-polymer composite composed of filler with ordinary (not nanosized) grains was used to execute insulators with the 500 mm creepage distance (Fig. 1). The insulators were moulded using newly developed PET moulds and subject to mechanical and electrical tests.

5.1. Testing for resistance to tracking and erosion

Insulators being under constant potential at power-frequency adequate to creepage distance of 20 mm/kV [12] were subject to the 1000 h action of salt mist. The rate of salt mist application was 0.4 ± 0.1 l/m^3·h, the size of drops 5–10 μm, salt mist concentration: 10 ± 0.5 kg/m^3. The applied high voltage system was so as under effective current of 250 mA, the drop of voltage in high voltage circuit was lower than 5%. The testing was performed in such a manner that between consecutive applications of voltage the time intervals were sufficient to minimize effects from the previous application. The most intensive discharges occurred during wetting of an insulator, i.e. during the first 2 h of 8 h application of voltage after 16 h time interval. No conducting paths or extensive erosion of electrical insulating material were produced during the test.

5.2. Electrical tests

The insulator units were tested as per PN-EN 60071-1:1999 [15] (wet power-frequency voltage test). The 50 kV [13, 14] alternating voltages were applied to insulators and maintained for 1 min. As no flashovers occurred, the test was evaluated as passed. The examined polymer concrete insulator units passed successfully also the lightning impulse voltage withstand tests as during application of 125 kV high voltage no disruptive discharge occurred.

5.3. Mechanical failing load test

The tested insulators were mounted horizontally to test machine and a mechanical bending load was applied (PN-EN 60168: 1999 P. 5.2.4 [16, 17]). The load which moved perpendicularly to the axis of the examined unit was increased smoothly until fail of insulator. The failing loads of the tested units were in the range of 5.4–5.9 kN and were higher than the nominal flexural strength of that class insulators (4 kN).

6. Test results and discussion

Methacrylate resin based CP compositions both with conventional and nanosize filler proved to have arc and tracking current handling capacities suitable for electroinsulating applications.

Methacrylate resin based CP insulators meet the insulator test specifications for mechanical strength and current handling. Owing to their high electric permittivities and fastness to exposure to hostile, excessive contaminated atmospheres, they can be successfully and safely used in outdoor applications without covering with additional protective film of silicone elastomer.

Mastering the PET foil technology of fabricating moulds for CP insulators will enable replacing the porcelain insulators by CP ones in the most onerous climatic conditions of II and III zones of contamination provided that CP insulators will meet environment test specifications.

References

[1] FOWLER D.W., *Current Status of Polymers in Concrete*. *Production, Performance and Potential of Polymers in Concrete*, Conference of the Fifth International Congress on Polymers in Concrete, September, 1987, 3–8.

[2] *Napowietrzna izolacja wysokonapięciowa w elektroenergetyce*, Z. Pohl (red.), Oficyna Wydawnicza Politechniki Wrocławskiej, Wrocław, 2003.

[3] GASPEROWICZ A., J. STANKIEWICZ, ADAMOWSKA M., *Optymalizacja silanowych środków sprzęgających do elektroizolacyjnego betonu polimerowego*, Dokumentacja Techniczna IEl-OTiME, 1994.

[4] GASPEROWICZ A., STANKIEWICZ J., JERZMAŃSKI D., MIELCAREK W., *Optymalizacja lepiszcza organicznego do elektroizolacyjnego betonu polimerowego*, Dokumentacja Techniczna IEl-OTiME, 1995.

[5] GASPEROWICZ A., STANKIEWICZ J., BŁAŻEJEWSKI W., *Próby technologiczne otrzymywania izolatorów z betonu polimerowego*, Dokumentacja Techniczna IEl-OTiME, 1996.

[6] STANKIEWICZ J., ŚWIERZYNA Z., MIERNIK H., *Niskolepkie żywice metakrylanowe jako materiał na izolatory z polimerobetonu*, 6. Konferencja naukowa „Postępy w Elektrotechnologii", Jamrozowa Polana, 20–22 września 2006.

[7] GASPEROWICZ A., TRACZEWSKI A., *Właściwości mechaniczne prototypów izolatorów napowietrznych z nowego, energooszczędnego materiału kompozytowego*; V Seminarium techniczne „Materiały i układy elektroizolacyjne w przemyśle", 26–28 kwietnia 2000.

[8] Patent RP nr 190300 *Dielektryczna kompozycja konstrukcyjna*, Gasperowicz A., Traczewski A., Stankiewicz J., Mundzia B., Karatowicz J., 9 listopada 2005.

[9] Prospekt firmy NTI-Pomiary w Głogowie.

[10] PN-74/E-04441 *Materiały elektroizolacyjne stałe. Badanie odporności na łuk elektryczny o małym natężeniu prądu przy wysokim napięciu*.

[11] PN-89/E-04442 *Materiały elektroizolacyjne stałe. Badanie odporności na prądy pełzające przy wysokim napięciu i pochyłej próbce*.

[12] PN-IEC 61109:1999 *Izolatory kompozytowe do linii napowietrznych prądu przemiennego o znamionowym napięciu powyżej 1000 V. Definicje, metody badań i kryteria odbioru*.

[13] PN-IEC 383-1:1997 *Izolatory do linii napowietrznych o znamionowym napięciu powyżej 1000 V. Izolatory ceramiczne lub szklane do sieci prądu przemiennego. Definicje, metody badań i kryteria odbioru*.

[14] PN-92/E-04060 *Wysokonapięciowa technika probiercza. Ogólne określenia i wymagania probiercze*.

[15] PN-EN 60071-1:1999 *Koordynacja izolacji. Definicje, zasady i reguły*.

[16] PN-IEC 60273:2003 *Właściwości wnętrzowych i napowietrznych izolatorów wsporczych do sieci o znamionowym napięciu powyżej 1000 V*.

[17] PN-EN 60168: 1999 *Badania izolatorów wsporczych wnętrzowych i napowietrznych ceramicznych lub szklanych do sieci o znamionowym napięciu powyżej 1000 V*.

Received 4 July 2007
Revised 23 August 2007

Materials Science-Poland, *Vol. 27*, *No. 4/2*, *2009*

BIMEVOX materials for application in SOFCS

J. CHMIELOWIEC*, G. PAŚCIAK, P. BUJŁO

Electrotechnical Institute Division of Electrotechnology and Materials Science,
M. Curie-Skłodowskiej 55/61, 50-369 Wrocław, Poland

Presented work concerns BIMEVOX (bismuth metal vanadium oxide) based solid electrolytes doped with rare earth elements (lanthanum). Investigations of melting point and compositions of elaborated materials were performed with the DTA and X-ray measurements. For determination of conductivities, the impedance spectroscopy method was applied. The influence of the material composition ($Bi_4V_2O_{11}$ doped with La), sintering time and gas atmosphere (air, reducing) on the conductivity was examined.

Key words: *fuel cell; solid electrolyte; BIVOX; SOFC*

1. Introduction

The element of a solid oxide fuel cell (SOFC) having the greatest impact on the fuel cell efficiency, production costs and stable operation, is the electrolyte. The most suitable electrolyte should possess high ionic conductivity (at minimum 0.01 S/cm) at relatively low temperature, impermeability for gases, good resistance to thermal shocks as well as good thermodynamic stability, especially in reducing atmosphere.

Nowadays, stabilized ZrO_2 (zirconium oxide) is the most often used and known type of the electrolyte for SOFC [1]. This material has suitable electrical parameters and mechanical strength but its main disadvantage is very high working temperature (800–1000 °C) limiting commercial application of this material. A real challenge for scientists is to develop new materials with high conductivities (comparable to ZrO_2) and operating below 600 °C. Suitable candidates seem to be doped Bi_2O_3 or CeO_2 but those materials exhibit increase of departure from stoichiometric composition in oxygen sublattice at low oxygen pressure. As a result, in CeO_2 based electrolytes the unwanted component of electronic conductivity appears and in the case of Bi_2O_3 based electrolytes this yields to decomposition to metallic bismuth [3–5]. Both electrolytes are the subject of research in order to obtain the materials with properties which enable application in fuel cells. Numerous papers have been published on the properties

*Corresponding author, e-mail: chmielowiec@iel.wroc.pl

of $Bi_4V_2O_{11}$ doped with Cu, Co, Y, Mg, Ti, Zr, Sc [6–11]. Products synthesized in this way belong to BIMEVOX family with stabilized high temperature γ-phase of $Bi_4V_2O_{11}$. The goal of research presented in the paper are investigations of BIMEVOX doped with lanthanum and determination if La dopant influences the phase composition and conductivity of this material.

2. Experimental

The electrolyte materials $Bi_4V_2O_{11}$ (molar fraction of Bi_2O_3 – 68.5%) and those doped with La (mass fraction of La – 1, 2, 3, 6, 8 and 10%) were fabricated by solid-state reaction from stoichiometric amounts of chemically pure oxides: Bi_2O_3 (Aldrich 99.9%), V_2O_5 (Riedel de Hahn 99.5%) and La_2O_3 (Aldrich 99.9%). The initial composition was mixed and milled in a ball mill for 24 h in dry condition. Obtained mixture was dried at 400 °C for 1 h to completely remove remaining humidity and break up any large agglomerates. The electrolyte samples had form of tablets which were pressed at room temperature under 600 kG/cm^2. Next multi step sintering process took place and the samples were sintered for 1, 5 and 10 h at temperatures below melting point of the materials. The melting points were determined by the differential thermal analysis (DTA) [12]. The compositions were characterized by X-ray powder diffraction (Siemens D5000 goniometer).

Conductivities were determined by the impedance spectroscopy method at a wide frequency range (20 Hz–1 MHz) with the HP 4284A LCR meter, 20 mV_{rms} test signal was applied [13, 14]. Measurements were taken on round shaped samples (1.3 mm thick) in air and pure nitrogen atmosphere ($O_2 \leq$ 30 ppm) as well as in vacuum (10^{-3} Tr). Conductivity measurements were also performed during a short test (2 h/650 °C) in pure reducing atmosphere. Propane–butane was used as a reducing gas. The platinum current electrodes were applied directly on the sample.

3. Results and discussion

Melting points of synthesised compositions are listed in Table 1. It was observed that the greater content of La dopant is, the higher melting point is measured. The results of X-ray measurements show significant influence of La addition (0–10%) on the phase composition of samples (Fig. 1). The X-ray spectra recorded for undoped samples and for those doped up to 3% are very similar.

Differences seen after detailed analysis (Fig. 2) are probably caused by a phase change $\alpha \rightarrow \gamma$ which occurs for polymorphic modification $Bi_4V_2O_{11}$. In Figure 2A (angle range 32–34.5°), the shift of the maximal reflection of $Bi_4V_2O_{11}$ phase is shown towards smaller 2Θ angles together with increasing amount of dopant. Figure 2B presents disappearing of one of reflection and sharpening of the other one which shifts towards smaller angles. Similar effect is observed for the angel range 56–57.4 (Fig. 2C). One of the reflections disappears and the other one occurs for smaller angles 2Θ.

Table 1. Melting points of synthesized ceramics

Sample composition	Melting point [°C]
$Bi_4V_2O_{11}$	870
$Bi_4V_2O_{11}$ + 1% La	885
$Bi_4V_2O_{11}$ + 2% La	890
$Bi_4V_2O_{11}$ + 3% La	890
$Bi_4V_2O_{11}$ + 6% La	908
$Bi_4V_2O_{11}$ + 8% La	920
$Bi_4V_2O_{11}$ + 10% La	935

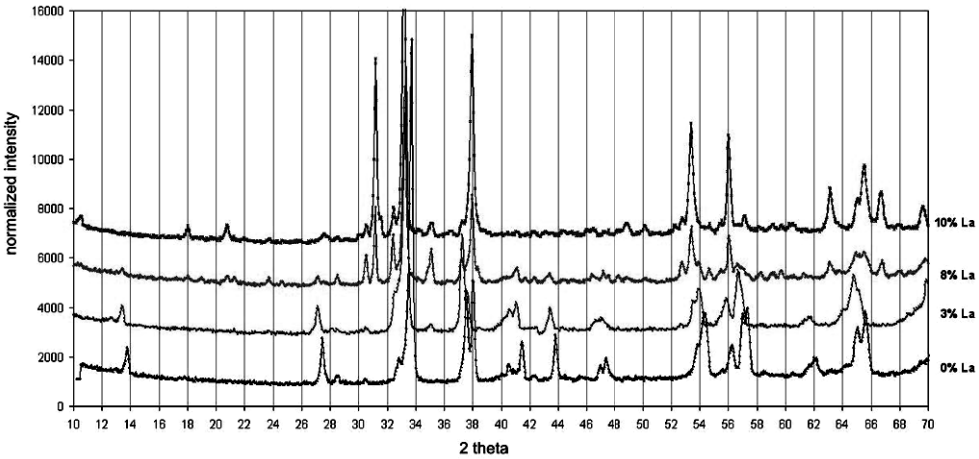

Fig. 1. X-ray spectra of the samples made of undoped mass $Bi_4V_2O_{11}$ (0% La) and $Bi_4V_2O_{11}$ doped with 3%, 8%, 10% La

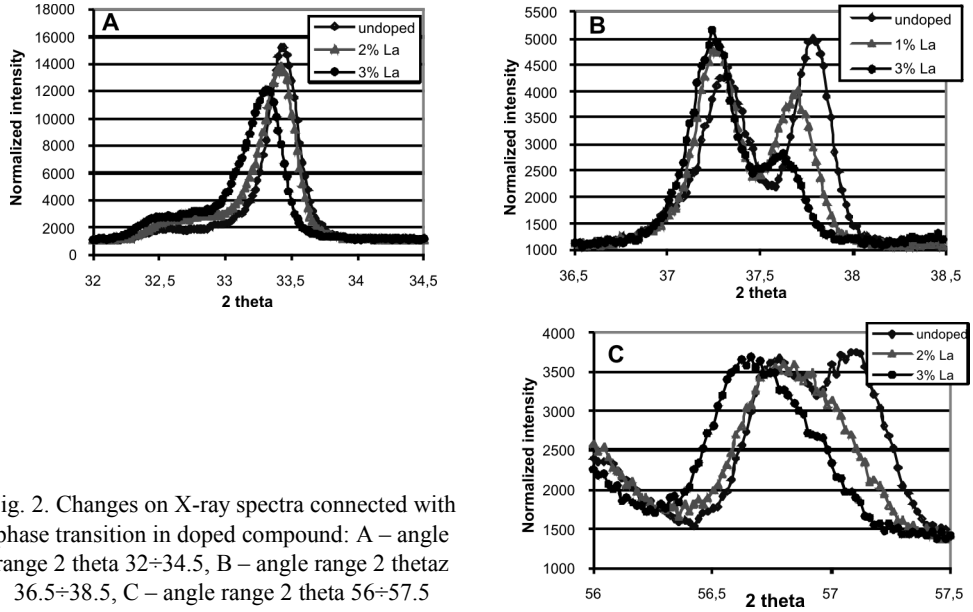

Fig. 2. Changes on X-ray spectra connected with phase transition in doped compound: A – angle range 2 theta 32÷34.5, B – angle range 2 thetaz 36.5÷38.5, C – angle range 2 theta 56÷57.5

According to expectations, the grain growth of the initial material ($Bi_4V_2O_{11}$) connected with longer and longer sintering was observed (from 3 μm for 1 h to 17 μm for 20 h, Fig. 3). Described changes, seen in the spectra of investigated samples, result from doping (1, 2 and 3% La) and prove that α phase in undoped sample exists. It can be also stated that high-temperature γ phase was stabilized as the amount of La dopant was increased. It seems that 3% dopant content is optimum because further increase of La fraction (6–10%) did not cause formation of new chemical compounds.

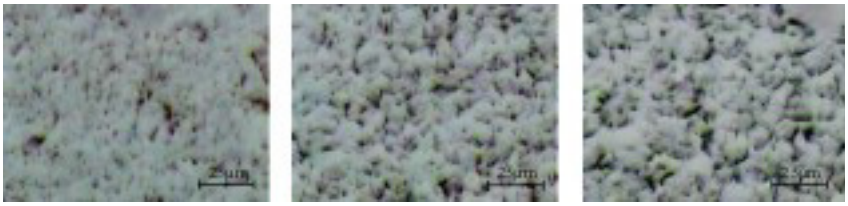

Fig. 3. Microstructure of undoped $Bi_4V_2O_{11}$ sample (sintering time – from left to right 1 h, 5 h, 10 h)

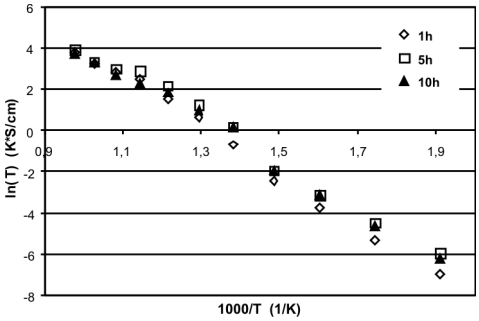

Fig. 4. Arrhenius characteristics of undoped $Bi_4V_2O_{11}$ in dependence on sintering time

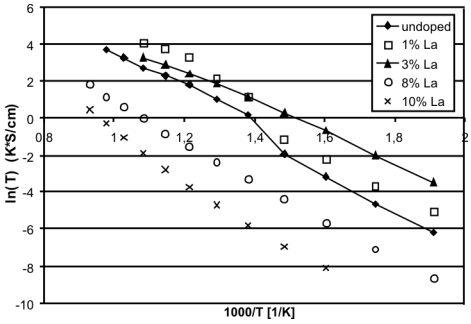

Fig. 5. Arrhenius characteristics of undoped and La doped $Bi_4V_2O_{11}$ measured in air atmosphere

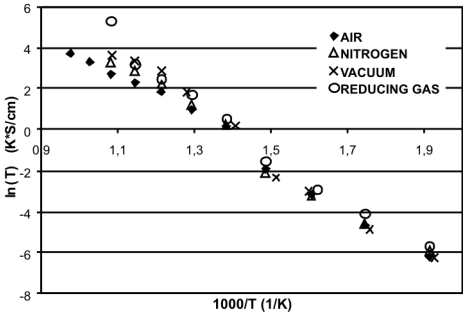

Fig. 6. Arrhenius characteristics of undoped $Bi_4V_2O_{11}$ in dependence on atmosphere

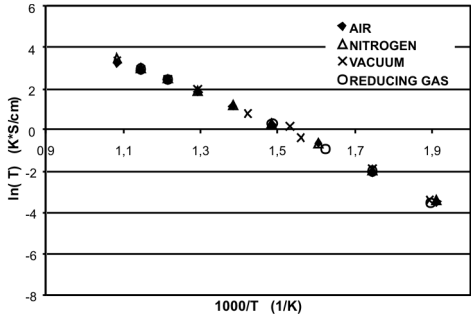

Fig. 7. Arrhenius characteristics of $Bi_4V_2O_{11}$ doped with 3% La in dependence on atmosphere

The measurements of conductivity were performed by use of impedance spectroscopy method in the temperature range 250–650 °C. Arrhenius plots obtained from

calculation performed by taking into account conductivity measurements are presented in Figs. 4–7. A significant influence of sintering time (grain size) on the conductivity of samples was not observed (Fig. 4). The addition of La causes increase of conductivity of the initial material in the full range of temperature. For the compositions with 2% and 3% of La, typical changes of the characteristic slope on the Arrhenius plot were not observed (different slopes for 0% La are responsible for phase changes α–β and β–γ). That could be the proof of the stability of the high temperature γ-$Bi_4V_2O_{11}$ phase with ionic conduction (Fig. 5). Although higher amounts of dopant (6, 8 and 10% La) stabilize γ phase, they also cause significant decrease of electrolyte conductivity. Probably reason are new chemical compounds which block charge transfer. For the further investigations of thermodynamical stability, materials with La content up to 3% were selected.

Based on measurements of the impedance of the initial material, which were made in various atmospheres (air, nitrogen, vacuum, reducing gas – propane–butane), an insignificant increase of conductivity of material in oxygen-free atmospheres for higher temperatures was confirmed (Figs. 6 and 7). This could be caused by increased amount of oxygen vacancies. Significant increase of conductivity in reducing gas atmosphere was observed at 650 °C and was caused by carbon deposition on the sample surface (Fig. 8).

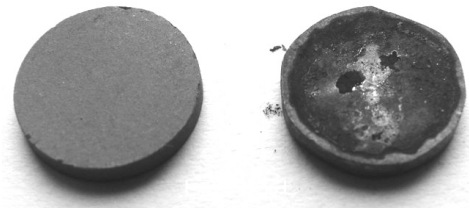

Fig. 8. BIMEVOX before (left) and after measurement in reducing atmosphere (right)

Table 2. Conductivities of BIMEVOX at 400 °C and 650 °C

Sample composition	$\sigma_{400}\times10^{-3}$ [1/Ωcm]	$\sigma_{650}\times10^{-2}$ [1/Ωcm]
$Bi_4V_2O_{11}$	0.22E-3	1.63
$Bi_4V_2O_{11}$ + 1% La	0.46	6.50
$Bi_4V_2O_{11}$ + 2% La	1.41	2.94
$Bi_4V_2O_{11}$ + 3% La	1.94	2.83
$Bi_4V_2O_{11}$ + 6% La	4.63-6	7.60-4
$Bi_4V_2O_{11}$ + 8% La	1.87-5	1.05-3
$Bi_4V_2O_{11}$ + 10% La	1.40-6	1.66-4

Carbon originated from decomposition gas fuel in the absence of humidification. However, the influence of atmosphere on composition and conductivity of samples

doped with La was not observed. in Table 2, the conductivities measured at 400 °C and 650 °C for: initial $Bi_4V_2O_{11}$ and doped with 1–10% La are presented.

4. Conclusion

Addition of La_2O_3 increases melting point and conductivity of $Bi_4V_2O_{11}$ by stabilization of high-temperature, good ionic O^{2-} conductive γ-$Bi_4V_2O_{11}$ phase. The type of conductivity (ionic or electronic) will be determined in the future works. For materials with La content higher than 3%, the decrease of conductivity was observed.

New electrolytes (up to 3% La content) are thermodynamically stable when placed in pure nitrogen and vacuum (10^{-3} Tr) and during short test (2 h) in pure reducing atmosphere (propane–butane, 650 °C).

The electrical and stability measurements allowed estimating the possibility of applications of elaborated materials in SOFC.

Acknowledgements

Presented work was realized in the frame of the grant No. 3 T10A 042 28 and was financially supported by the Polish Ministry of Science and Higher Education. Research were also a part of the national project (COST/261/2006) realised in the frame of COST Action 542.

References

[1] MIZUTANI Y., HISADA K., UKAI K., SUMI H., J. Alloy Comp., 408–412 (2006), 518.
[2] MOLENDA J., Zrównoważone systemy energetyczne, Zakopane 2005, 46–55.
[3] YAREMCHENKO A., KHARTON V.V., NAUMOVICH E.N., TONOYAN A., Mat. Res. Bull., 35 (2000), 515.
[4] VERKERK M.J., BURGGRAAF A.J., J. Electrochem. Soc., 128 (1981), 75.
[5] TAKAHASHI T., ESAKA T., IWAHARA H., J. Appl. Electrochem., 7 (1977), 299.
[6] CHO H.S., SAKAI G., SHIMANOE K., YAMAZOE N., Sensors Act. B, 109 (2005), 307.
[7] ABRAHAMS I., KROK F., MALYS M., WROBEL W., Solid State Ionic, 176 (2005), 2053.
[8] ZHEN Q., KALE G.M., SHI G., LI R., HE W., LIU J., Solid State Ionic, 176 (2005), 2727.
[9] LOFBERG A., PIROVANO C., STEIL M.C., VANNIER R.N., BORDES-RICHARD E., Catalysis Today 112 (2006), 8.
[10] ZYRYANOV V.V., J. Struct. Chem., 45 (2004), S133.
[11] PAŚCIAK G., CHMIELOWIEC J., BUJŁO P., Mater. Sci.-Poland, 23 (2005), 209.
[12] YANG J., ROY C., Thermochim. Acta. 333 (1999), 131.
[13] MACDONALD J.R., *Impedance Spectroscopy*, Wiley, New York, 1987.
[14] ZAJT T., Metody woltamperometryczne i elektrochemiczna spektroskopia impedancyjna, Wyd. Gdańskie Sp. z o.o., Gdańsk, 2001.

Received 1 August 2007
Revised 23 August 2007

Materials Science-Poland, *Vol. 27*, *No. 4/2*, *2009*

The influence of electric field on HFC-245fa condensation

A. BRYSZEWSKA-MAZUREK[1*], W. MAZUREK[1, 2]

[1]Wroclaw University of Technology, W7/K1

[2]Electrotechnical Institute Division of Electrotechnology and Materials Science, Wrocław, Poland

Condensation of HFC-245fa on a vertical cylindrical surface of a heat pipe has been studied experimentally. The temperature of the heat pipe evaporator decreased under the electric field (ac and dc). Heat transfer enhancement was observed when the electrode placed in a condenser section of the pipe was under a high voltage. The heat pipe thermal conductivity increased about 6–8% dependently of a magnitude and kind of high voltage. The best results were obtained for the straight polarity of the electrode.

Key words: *heat pipe; condensation; EHD heat transfer enhancement*

1. Introduction

The mechanism of electrohydrodynamic (EHD) enhancement, one of methods of active heat transfer enhancement, is widely used to improve heat transfer and fluid flow [1]. The electric field can enhance the heat transfer in single and two-phase systems.

In the investigations, an electric field was used to improve and control a heat pipe performance. In a heat pipe, the heat transfer depends of condensation and evaporation processes on the pipe surfaces. These processes occur in an inner surface of the pipe. A thermosyphon was used – a heat pipe with the condensing working fluid flowing to the evaporation area under the gravitational force. In previous studies of the authors, heat pipes were tested with other working fluids such as deionized water, R-141b [2] and R-365/227 [3]. The condensation section of the pipe was under the electric field operation and the evaporator was grounded. The enhancement of heat transfer during condensation has been expected for the heat pipe working with HFC-245fa.

Many examples are known of utilizing the electric field to enhance the condensation [1] but most of reports concerned external condensation on flat and cylindrical

*Corresponding author, e-mail: wojciech.mazurek@pwr.wroc.pl

surfaces. According to Didkovsky and Bologa [4], Yabe et al. [5], Sunada et al. [6] and Yamashita and Yabe [7], condensation heat transfer was significantly improved by EHD for a variety of working fluids such as R-113, R-123 and other organic substances. A prototype EHD condenser was successfully built and tested by Yamashita et al. [8]. The EHD-assisted external condensation of R-134a on smooth horizontal and vertical tubs was investigated by Cheung et al. [9]. Butrymowicz et al. [10] described a novel EHD method of condensate drainage from horizontal finned tubs (experiments with R-123).

The heat transfer mechanism involves an effective removal process of liquid condensate from the heat transfer surface, minimizing the film thickness by utilizing the EHD-induced forces. However, this requires a careful design of the electrode to yield a maximum enhancement at minimum power consumption.

2. Experimental

A dielectric heat pipe (DHP) has been constructed, where the condensation section was separated from the evaporation section by a high voltage insulator. Measurements of DHP characteristics and testing of DHP performance were conducted within the system presented in Fig. 1.

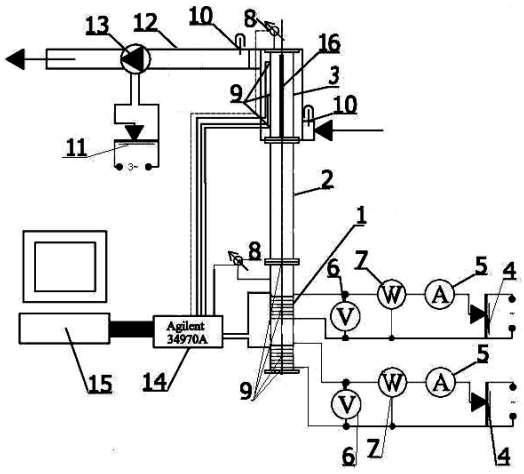

Fig. 1. Schematic of experimental arrangement for the DHP testing

Dielectric heat pipe consists of an evaporator (1) being a segment of a copper pipe with the dimension 22×1 mm and 2×30 cm long, an electric insulator (2) composed of two parts of a teflon-epoxy pipe 30 cm long, with the dimension 40×10 mm and a condenser (3) made of a bronze pipe with the dimension 26×3 mm 93 cm long. Six copper fins was put on the external surface of the condenser. The whole condenser was placed in a steel pipe with the dimension 125 mm, where flows cooling air. The

tested pipe was placed in a vertical position to enable the gravitational flow of condensate from the condenser to the evaporator.

Heat was delivered to the evaporation section (1) by means of an electric heater which was placed on the outer surface of the evaporator. Electric power of the heater was controlled by an autotransformer (4). Power measurement was made by means of a wattmeter (7). Additionally, the power supply system was connected with a voltmeter (6) and an ammeter (5). Heat flux transferred from the working fluid to the DHP condenser (3) was taken out to the surroundings by forced convection. Copper fins were placed along the outer surface of the condenser for increasing the cooling area. The condenser was put into the duct (12) where the cooling air flows. The ventilating fun (13) sucks air in the room and then after heating up, it is exhausted through the wall outside the building. The fun flow was controlled by an autotransformer (11).

Two air temperature sensors Pt 100 (10) were mounted into the air duct (12). The pipe surface temperatures were measured by means of K-type thermocouples (9). The pressure sensors (8) were installed in a condenser and an evaporator. The measuring data was recorded using a data acquisition system Agilent HP 34970A type (14) and PC (15).

A high voltage source for DHP was the high voltage transformer in the case of ac or electric feeder in the case of dc+ and dc– polarity. High voltage was applied to a copper rod introduced axially into the condensation section. The rod (16) (bar electrode) had the diameter of 8 mm.

3. Results of experiment

In order to check how electric field affects the performance of DHP operating with HFC-245fa, the measurements of thermal characteristics for the pipe model have been made. After applying a high voltage to the bar electrode inside the condenser, the radial component of electric field (perpendicular to the liquid–gas interface) was forced. In this way, an electric field can effect vapour and liquid of working fluid in DHP condensation section.

The DHP working with HFC-245fa was tested for transferred heat in the range of 300–500 W. The following measurements were done: the temperature distribution on the pipe surface, heat transferred through the pipe, pressure inside the pipe, voltage applied to the electrode. Experiments were taken for a fixed value of heat transfer and various voltages: ac and dc (for both polarities) in the range of 0–20 kV. For voltages higher than 25 kV, the breakdown was observed.

Under the electric field (ac and dc), the temperature on the evaporator decreased and the difference between temperatures of the evaporator and condenser decreased as well. The strongest effect of electric field was observed for dc+. Decreasing temperature in the evaporator can be connected with enhancement of condensation heat transfer in presence of electric field. The augmentation of condensation flow let to intensive evaporation and consequently a decrease of temperature of electric heaters was observed.

Decreasing of the difference of temperatures between the evaporator and condenser for fixed heat transfer causes that the DHP thermal conductivity (1) increases. The DHP thermal conductivity is the ability of the pipe (with a given length and dimension) to transport heat for a given difference of temperatures between the evaporator and condenser sections:

$$\lambda = \frac{QL}{\Delta TF} \tag{1}$$

where: λ is the DHP thermal conductivity, W/(m·K), Q – heat transported through DHP, W, F – cross-section area of DHP, m^2, L – DHP length, m, ΔT– difference of temperatures between the evaporator and condenser sections, K.

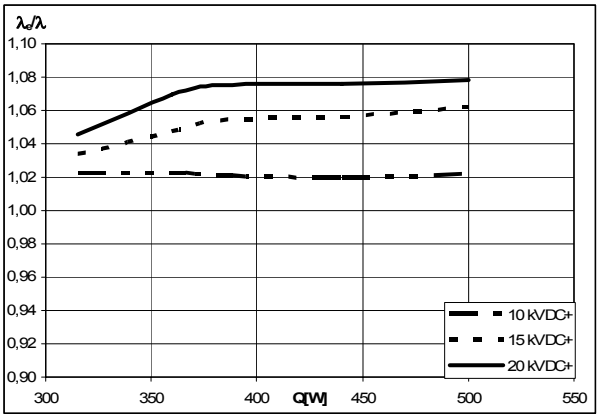

Fig. 2. The relative thermal conductivity of DHP versus the heat transfer (dc+)

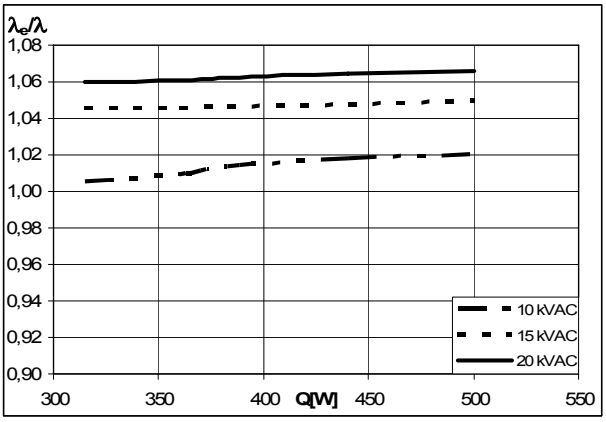

Fig. 3. The relative thermal conductivity of DHP versus the heat transfer (ac)

Figures 2 and 3 show a relative thermal conductivity of DHP; the thermal conductivity for the pipe under high voltage was compared to the thermal conductivity with-

out voltage. By increasing the electric strength (i.e. the applied voltage), the thermal conductivity of DHP could be increased. Analyzing results of the experiments, we can find that the heat pipe performance could be enhanced by dc+ electric field. Maximum augmentation of the thermal conductivity was about 8% and it was observed for voltages exceeding 15 kV (which corresponds to the electric field strength 1600 kV/m on the condenser surface).

Enhancement of heat transfer was observed also for ac electric field and the maximum augmentation of the thermal conductivity was about 6%. Similarly as for dc+, the effect of electric field was observed for voltages exceeding 15 kV (for the electric field strength 1600 kV/m on the condenser surface).

4. Conclusions

The effect of electric field on condensation of HFC-245fa on a vertical, cylindrical surface has been studied experimentally. The condensation was observed on the inner surface of the heat pipe. Electric field influenced not only condensation of HFC-245fa (working fluid in the heat pipe) but the performance of the whole heat pipe. After applying high voltages (ac and dc) to the bar electrode inside the condenser, decreasing of temperature in the evaporation region was observed. It caused that the thermal conductivity of the heat pipe increased maximally about 6–8%, depending on the kind and magnitude of electric field. The highest augmentations were observed for dc+ electric field. The effect of electric field could be connected with the destabilization of liquid-vapour interface in a condensation region of the heat pipe.

References

[1] ALLEN P., KARAYIANNIS T., Heat Recovery Syst. CHP, 15 (1995), 389.
[2] MAZUREK W., Dielektryczna rura cieplna (*Dielectric Heat Pipe*), PHD thesis (in Polish), Wroclaw University of Technology, Wrocław, 2000.
[3] BRYSZEWSKA-MAZUREK A., MAZUREK W., RUTKOWSKI J., *Electric field influence on the condensation process in dielectric heat pipe operating with R365/227*, Proc. 2nd Int. Conf. Advances in Processing, Testing and Application of Dielectric Materials, Wroclaw, Poland, 2004, 262–266.
[4] DIDKOVSKY A., BOLOGA M., Int. J. Heat Mass Transfer, 24 (1981), 811.
[5] YABE A., TAKETANI T., KIKUCHI K., MORI Y., HIJIKATA K Int. Heat Transfer Sci. Techn., 7 (1987), 812.
[6] SUNADA K., KAZUMI K., YABE A., TAKATANI T., YOSHIZAWA Y., *Experimental study of EHD pseudo-dropwise condensation*, Proc. 3rd ASME/JSME Thermal Engineering, 1991, 47–53.
[7] YAMASHITA K., YABE A., J. Heat Transfer, 19 (1997), 339.
[8] YAMASHITA K., KUMAGAI M., SEKITA S., *Heat transfer characteristics on an EHD condenser*, Proc. 3rd ASME/JSME Thermal Engineering, 1991, 61–67.
[9] CHEUNG K., OHADI M., DESSIATOUN S., Int. J. Heat Mass Transfer, 42 (1999), 1747.
[10] BUTRYMOWICZ D., TRELA M., KARWACKI J., Int. Jo. Refr., 26 (2003), 473.

Received 13 July 2007
Revised 12 August 2007

Materials Science-Poland, *Vol. 27*, *No. 4/2*, *2009*

Novel method of charge mobility assignation in liquid dielectrics by streaming electrification

S. WOLNY*, J. KĘDZIA, M. ZDANOWSKI

Opole University of Technology, ul. Prószkowska 76, 45-758 Opole, Poland

The mobility of charge carriers is the parameter used for describing conductivity caused by the electrification activity. It is studied for substances of various states of aggregation, in the range including gases, liquids and solid bodies, for conductors, semi-conductors and dielectrics. The knowledge of this value is of great significance for the research work on insulation liquids. Transformer insulation oils, where due to the range of interest this issue is especially significant, serve as a good example. The paper presents a new method of the research on the mobility of charge carriers in insulation liquids, based on the application of the streaming electrification measurements of such liquids.

Key words: *mobility; streaming electrification; oil insulation*

1. Introduction

In insulation liquids, despite the fact that they are dielectrics, an infinite number of charge carriers exist. Their behaviour in the electric field is of significance in the description of the mechanisms of conductivity, loss, breakdown, charge injection from the electrodes, currents limited by a spatial charge and electroconvection phenomena. The parameter used for describing the behaviour of charge carriers is their mobility. In practice, a lot of methods are used for investigating the charge carrier mobility in conductors, semi-conductors and insulators. Their application results from the usefulness of the particular methods. In insulation liquids, the research work in this scope was developed by Adamczewski [1]. The research was based on examining the phenomenon of conductivity induced by an external ionizing factor. An observation of the phenomenon of the currents limited by the spatial charge was carried out as well. Also the research work on the charge injections from the electrodes was of great significance. The methods based on the measurements of the Hall phenomenon, so widely used in the research on carrier mobility in semi-conductors, did not find their application in

*Corresponding author, e-mail: s.wolny@po.opole.pl

the research on charge mobility in dielectric liquids. However, the mobility measurement method, based on the observation of the electrokinetic phenomena, the so-called electrophoresis phenomenon, was found useful. The method is based on the measurement of electrokinetic potential ζ. It may be determined through the observation of movement of solid particles in liquid affected by the electric field applied [2, 3].

The paper presents the suggestion of determining the charge carrier mobility in liquid using for measurements a different electrokinetic phenomenon – the so-called flow potential.

2. Streaming electrification

The flow potential occurs when, on the border of the solid and liquid phases, their mutual relocation takes place causing the disruption of the charge double layer on their border. The electrostatic charge that is generated may be of a high value and constitute hazard to the apparatus in which it occurs. Such hazard was observed in power transformers with a forced insulation oil flow. Due to a considerable hazard to the insulation caused by the static electricity generated, thus also economic aspects, these issues have been investigated in a wide range of the occurring phenomena [4, 5]. They can be presented on the example of the research tests carried out in a model laboratory system with a spinning disk [6, 7] (Fig. 1).

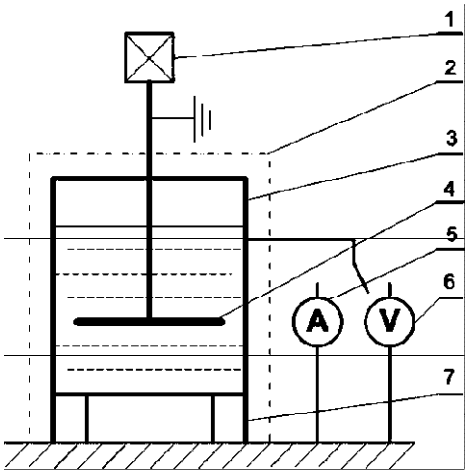

Fig. 1. Diagram of the measuring system with a spinning disk: 1 – motor, 2 – shield, 3 – measuring container, 4 – spinning disk, 5 – electrometer, 6 – electrostatic voltmeter, 7 – insulators

On the interfacial surface (the solid phase of the disk and the liquid under study), a double layer of charges is formed due to a selective adsorption of ions. The activity of centrifugal forces at the disk rotation causes its disruption. The charge generated can be the source of the current measured with an electrometer or charge the capacity of the disk–measuring container and be measured with an electrostatic voltmeter. Hydrodynamic conditions, at which the electrostatic charge generation takes place, depend on the disk size, its rotations and on the properties of the liquid under study. Fig-

ures 2–5 show selected characteristics that determine them. They were calculated for insulation oil the properties of which are shown in Table 1.

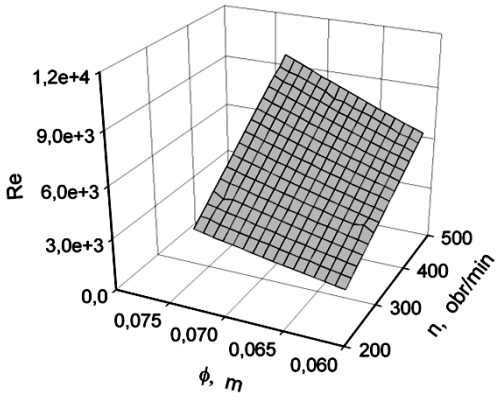

Fig. 2. Dependence of the Reynolds number on the rotational speed and the disk diameter

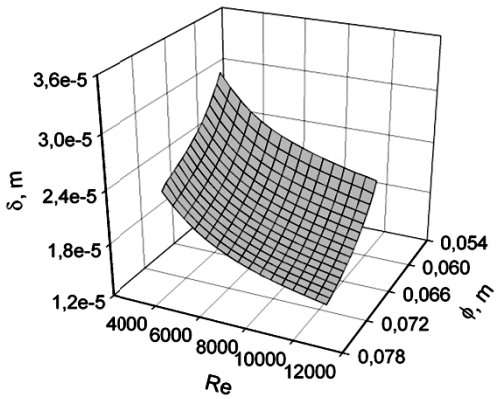

Fig. 3. Dependence of the laminar layer thickness on the Reynolds number and the spinning disk diameter

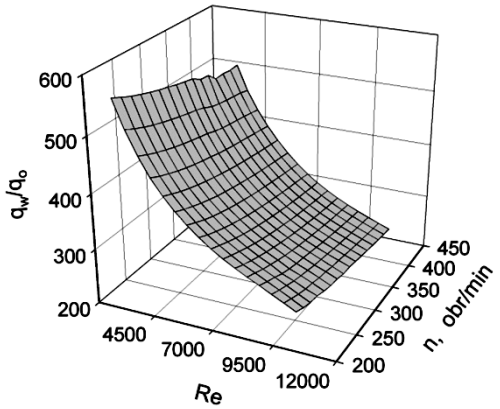

Fig. 4. Dependence of q_w/q_0 on the Reynolds number and rotational speed of the disk

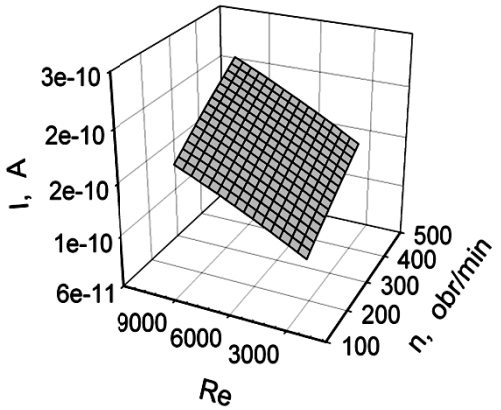

Fig. 5. Dependence of the electrification current on the Reynolds number and rotational speed of the disk

The dependence of the Reynolds number on rotational speed and the disk diameter is shown in Fig. 2. The range of the presented values *Re* refers to turbulent flows. Then, on the border of the solid and liquid phases, it is possible to distinguish a laminar sublayer, which, further on, moves into the turbulent area. Its thickness, depending on the hydrodynamic conditions, is shown in Fig. 3. It decides, among others, on the change of volume charge density, which in the laminar sublayer is of value q_w and lowers to value q_0 in the turbulent flow area. The dependence of these changes is shown in Fig. 4, and the electrification current value measured in the external circuit is shown in Fig. 5.

3. Liquid electrification in the disk system

A lot of models have been published which try to present quantitatively the electrification process of the liquid under study [8]. One of the most common models is the Abedian–Sonin model, which for the disk system can be presented in the form [9]:

$$I = \frac{\sigma q_0 V}{\varepsilon_0 \varepsilon_w} + \frac{D_m q_0 S_t}{\delta} - \frac{D_m q_w S_t}{\delta} \tag{1}$$

where: σ is the liquid conductivity, V – liquid volume in the measuring container, ε_w – relative permittivity of the liquid under study, ε_0 – vacuum permittivity, D_m – *the* molecular diffusion coefficient in liquid, S_t – disk surface, δ – average thickness of the laminar sublayer on the disk surface.

The calculation of the electrification current from the Abedian–Sonin model requires the knowledge of the definite parameters characterizing the liquid under study, such as density (ρ), conductivity (σ), viscosity (ν), permittivity (ε_w), molecular diffusion coefficient (D_m), volume charge density (q_w and q_0). Also the knowledge of the parameters characterizing hydrodynamic conditions such as the Reynolds number, laminar sublayer thickness (δ), shearing stresses (τ_w) is necessary. The measurement of such values as ρ, σ, ν, ε_w does not cause a metrological problem. However, the molecular diffusion coefficient (D_m) is usually calculated from Adamczewski's dependence [1], and the knowledge of charge density q_w requires, first of all, the measurement of the charge q_0 volume density. It can be determined from the measurement of voltage generated on the patulous outlet of the disk system:

$$U = \frac{V q_0}{C} \tag{2}$$

where: V – volume of the liquid under study, q_0 – volume charge density in the liquid under study, C – electric capacity of the disk system.

A mutual relationship between charges q_w and q_0 is described by the dependence:

$$\frac{q_w}{q_0} = 1 + \frac{\delta V}{S\lambda^2} \tag{3}$$

where: λ – Debye's length ($\lambda = (D_m \varepsilon_0 \varepsilon_w)/\sigma)^{1/2}$), S – contact surface of the disk and the container with the liquid under study, δ – thickness of the laminar sublayer on the disk surface.

Therefore, determining the density of the volume charge q_w on the border of solid and liquid phases requires only the calculation of the thickness of the laminar sublayer δ.

$$\delta = \frac{11.7\nu}{\left(\frac{\nu}{D_m}\right)^{0.33}\left(\frac{\tau_w}{\rho}\right)^{0.50}} \tag{4}$$

where: ν – kinematic viscosity of the liquid, D_m – molecular diffusion coefficient, ρ – liquid density, τ_w – shearing stresses

$$\tau_w \approx 0.1 Re^{-0,5} \rho(\varpi R)^2$$

Using these data and dependences in the Abedian–Sonin model makes it possible to calculate the current generated in the disk system.

4. Measurement of the charge carrier mobility

Electrostatic charge generation in the disk system can be also verified by the measurement of the current on the system outlet. Combining the results obtained in the voltage and current systems makes it possible to calculate one of the parameters from the Abedian–Sonin model. When this parameter is the molecular diffusion coefficient (D_m), then by using Einsten's dependence:

$$\frac{D_m}{\mu} = \frac{kT}{e} \tag{5}$$

we obtain the possibility of determining the charge carrier mobility in the liquid under study. The measurements of the electrification current and the voltage generated were taken for fresh transformer oil. Table 1 shows the properties of the oil under study and the parameters of the measuring system.

Table 1. Properties of the oil under study
and the parameters of the measuring system

Property, parameter	Unit	Value
Density (ρ)	kg/m^3	874
Viscosity (ν)	m^2/s	$2.38 \cdot 10^{-5}$
Permittivity (ε_w)	–	2.239
Conductivity (σ)	$\Omega^{-1} \cdot m^{-1}$	4.2×10^{-13}
Disk radius (R_1)	m	0.0675
Container radius (R_2)	m	0.075

The dependences of the electrification voltage on the disk rotational speed is shown in Fig. 6, and the dependence of the electrification current on the disk rotational speed is shown in Fig. 7.

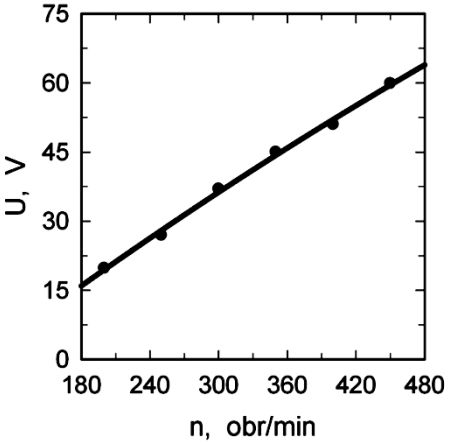

Fig. 6. The dependence of the electrification voltage on the disk rotational speed

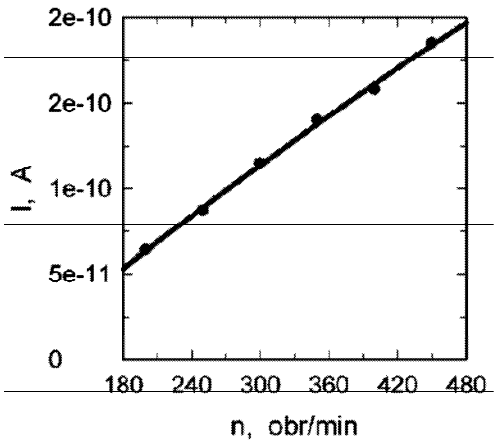

Fig. 7. The dependence of the electrification current on the disk rotational speed

Combining the dependence for the electrification current (1) with the dependence for the electrification voltage (2), through Einstein's dependence (5), the charge carrier mobility in insulation oil was calculated. The results are shown in Fig. 8.

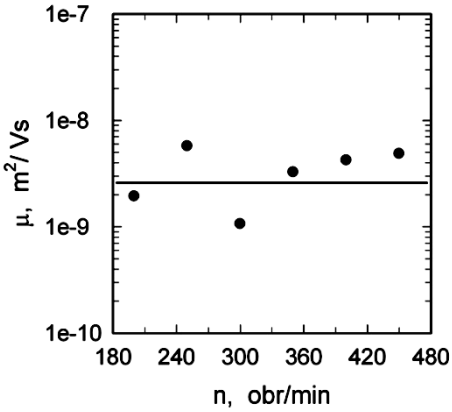

Fig. 8. Charge carrier mobility at various rotational speeds of the disk

The average value of the carrier mobility, obtained at various rotational speeds of the disk, is marked with a horizontal line. A considerable correspondence, of the value occurring in literature, of about (1×10^{-9} m^2/Vs) was obtained.

5. Summing-up

The obtained results of the charge carrier mobility in insulation oil prove that the research on the streaming electrification can be found useful for the evaluation of the conductivity phenomenon in such liquids. However, the method suggested still re-

quires verification, first of all with the application of pure hydrocarbons. Insulation oils are liquids of a very complex chemical constitution, which makes it difficult to compare the research results obtained.

References

[1] ADAMCZEWSKI I., *Ionization and Electric Conduction Dielectrics Liquids*, PWN, Warszawa, 1965, (in Polish).

[2] ZBOROMIRSKA-WNUKIEWICZ B., SOKOŁOWSKI A., GRYZŁO K., *ZETA Potential of Ceramic Materials*, Prace Nauk. Inst. PEiE Politechniki Wrocławskiej nr 38, ser. Konferencje nr 13, (2003), 317, (in Polish).

[3] ZDANOWSKI M., KĘDZIA J., *The Use of Potential Zeta (ζ) for Research on Streaming Electrification*, Prace Nauk. Inst. PEiE Politechniki Wrocławskiej nr 44, seria Konferencje nr 18, (2006), 81, (in Polish).

[4] MELCHER J., LYON D., ZAHN M., *Flow electrification in transformer oil cellulose systems*, Annual Report Conference on Electrical Insulation and Dielectric Phenomena, Claymont, Delaware (1986), 257.

[5] KĘDZIA J., *Menace for Power Transformers Insulations Cause Static Electrification*, Oficyna Wydawnicza Politechniki Opolskiej, Opole 1999, (in Polish).

[6] KĘDZIA J., IEEE Trans Electr. Insul., 24 (1989), 59.

[7] KĘDZIA J., WILLNER B., IEEE Trans. Dielectr. Electr. Insul., 1 (1994), 58.

[8] WOLNY S., KĘDZIA J., ZDANOWSKI M., *The Analysis of Streaming Electrification from a Perspective of Laminar and Turbulent Flow Models*, Przegląd Elektrotechniczny, Konferencje, 4 (2006), 276, (in Polish).

[9] ABEDIAN B., SONIN A.A., J. Fluid Mech., 120 (1981), 199.

Received 23 March 2007
Revised 13 March 2008

Materials Science-Poland, *Vol. 27*, *No. 4/2*, *2009*

Polyaniline–multi-walled carbon nanotube shell-core composite as an electrode material in supercapacitors

E. ZAWADZKA, R. KULIŃSKI, B. SZUBZDA*, B. MAZUREK

Electrotechnical Institute, Division of Electrotechnology and Materials Science, Wroclaw, Poland

Polyaniline–multi-walled carbon nanotubes (PANI/MWCNTs) composite has been synthesized by *in situ* oxidizing polymerization of aniline in water dispersion of MWCNTs and has been tested as a supercapacitor electrode material. Supercapacitive behaviour of the shell core composite has been investigated by a cyclic voltammetry and galvanostatic charge-discharge tests. In order to obtain information about the composite composition additional thermoanalytical tests have been carried out including mass decrement and heat stream in function of temperature. The research is aimed at utilization of the specific structure of the shell core composite type for designing new materials with promising properties which could find application as supercapacitor electrode materials.

Key words: *supercapacitor; carbon nanotubes; polyaniline; shell core composite*

1. Introduction

The storage of electric energy is a crucial problem which has to be dealt with in the nearest future. Solutions are sought which should permit for a prolonged storage of energy gained from unconventional, renewable energy sources (solar energy, wind power). There is also need for transit stores capable of quick, short-term storage of excess energy and its quick return. In the present paper, we deal with the second type of store-houses. An example of such solution can be emergency power supplies of UPS type, as well as systems used in electric vehicles which are designed to regain and store the energy of braking [1–3]. For this task supercapacitors are perfectly suited because they have a relatively high power and can provide much energy in a short time. There are two basic types of supercapacitors which differ in mechanisms of collecting charges. The first type capacitors use an electrical double layer which is created mainly on activated carbon materials. The other type are the so-called pseudocapacitors in which the collecting of charges is related with a transport of electric charge in metal oxides [4] and conducting polymers [4, 5].

*Corresponding author, e-mail: szubzda@iel.wroc.pl

From a simple notation of the energy W:

$$W = \frac{1}{2}CU^2 = \frac{1}{2}\frac{\varepsilon S}{d}E^2d^2 = \frac{1}{2}\varepsilon E^2 V$$

where: $\varepsilon = \varepsilon_r\varepsilon_0$ – electric permittivity [F/m], E – electric field strength [V/m], $V = Sd$ – dielectric volume in which energy is contained [m^3] it results that the amount of the collected energy is limited by the spatial energy density $(1/2)\varepsilon E^2$ and the volume between electrodes. This leads to the idea, tested and applied in practice, to produce electrodes of a materials with high porosity and high value of physical area, even up to several thousand of m^2/g, such as e.g. activated carbons. In this case, a dependence is fulfilled that the bigger the physical area of carbon electrode, the higher is its capacity and energy. It turned out, however, that oxides and conducting polymers, having relatively small physical area (several dozen to one hundred m^2/g) have also high values of capacity and energy. This phenomenon is not fully clarified yet, despite a constantly growing number of papers concerning this issue [7]. Material for electrodes should also possess high mechanical strength as well as high thermal and electrical conductivity. Such properties are characteristic of carbon nanotubes, hence the concept of producing composite electrodes such as conducting polymers reinforced with nanotubes [6–11].

It is proved that addition of carbon nanotubes (CNTs) to polymer matrix diminishes the main disadvantage of electroconducting polymer (ECP), which is poor stability during cycling [12, 13]. CNTs. Since they have been discovered by Iijima et al. [14], play a significant role in nanoscience. Their unique mechanical, electrical and chemical properties made them useful in many fields of science. They are used, among others, as field emmiters [15], nanoelectronic devices [16], nanotube-based composites [17], and else.

Ajayan et al. were first to prepare composite of CNTs and conducting polymer [11]. Such composites were made by mechanical mixing MWCNTs in epoxy resin. CNTs were used as components of many composites: with PPy (polypyrolle)/CNT, PEDOT/CNT (poly(3,4-ethyledioxythiopene)) used as organic light emitting diodes [18], poly(3-octylthionene)/CNT, PPV/CNT (poly(phenylenevenylene)) used in highly efficient photovoltaic cells [19, 20], and PAN (polyacrylonitrile)/CNT, PANI (polyaniline)/CNT used as capacitor electrode materials [21–23].

In this paper, we described synthesis of "shell-core" PANI/MWCNTs composite, fabricated by in-situ oxidizing polymerization and its application as an electrode in a supercapacitor. In such a composite, a semiconducting nanostructure is enclosed in a conductor casing. Such spatial connection of a filler and a polymer matrix gives considerably more possibilities of extrapolating their mutual interaction and controlling the properties of an output composite [24]. The product quality is less influenced by the dispergation degree of cylindrical tubes in comparison to the spherical and lamellar fillers, since dispersion depends mainly on the orientation of the filler particles, and secondly on the separation degree of the particles. In the case of investigated sys-

tem, the most of nanotubes have the orientation along their structure what can be used as an advantage for the composite. The multi-walled nanotubes used in the experiment were chosen with regard to their higher thermal and chemical resistivity in comparison to uni-walled ones [24, 27].

Polyaniline (PANI) is a very stable conducting polymer with good damping and antistatic properties, resistant to most of organic solvents. However, its mechanical strength is low and its processing is difficult, because the use of too strong cutting forces or too high temperatures may lead to the loss of conductive properties. The conductivity of polyaniline depends on its oxidation degree. This can be improved by choosing an appropriate method and conditions of synthesis (oxidizing polymerization, electrochemical polymerization, synthesis of conducting salt PANI-HCl) or modification of the ready polymer (doping with sulfonic acid) [10].

Conductivity in polyaniline takes place along the main chain, statistically placed perpendicularly to nanotubes (by the "shell core" structure), which may give interesting results due to the spatial orientation of CNTs. The polyaniline conductivity can be controlled in the phase of polymerization or processing. Polyaniline in a glassy state can be easily pulverized and combined with other polymers as dry blendes for easier processing or plastics refining [9, 25].

The total covering of a nanotube with a polymer is a difficult task. Polyaniline is a good material for such purpose due to its environmental stability and due to the fact that its conductivity can be controlled by doping. In the process of nanocomposite creation it is helpful to make use of a compatibilizer which increases the efficiency of covering the nanotube surface with a polymer. The role of such an agent can be played by non-ionic surfactants of co-polymerizing monomers. Non-ionic surfactants additionally raise the degree of nanotube dispersion, thus helping to break up their aggregations [10, 24, 25, 28].

2. Experimental

The *in situ* method of polymerization was used in which anilines are oxidized in water dispersion of multi-walled nanotubes. The initial amounts of all components were calculated to give a composite with of the weight composition 0.75 PANI/0.25 MWCNT. MWCNT was introduced into an aqueous solution of a block co-polymer of ethylene oxide and propylene oxide (PEO-PPO, non-ionic surfactant) and exposed to ultrasound action. A non-sedimenting dispersion was obtained which was then cooled down to ca. 0 °C. Further, cooled down aniline (ANI) was instilled and the solution was stirred with mechanical mixer at this temperature. A polymerizing agent (oxidant – ammonium persulfate) was introduced into the cold solution which was then left to enable the reaction to proceed. The raw product was transferred onto a soft quantitative drain and washed several times with distilled water and ethanol to remove residues of the compatibilizer and excessive amount of polymerizing agent. The composite purified in this way was dried 8 h at 60 °C in vacuum and next 12 h in the ambient air. The ready composite had a form of a black, compact but brittle sediment.

The following materials have been used: multi-walled nanotubes, MWCNT 90%, Aldrich, block co-polymer PEO-PPO, Pluronic F-68, Sigma, aniline, ACS reagent ≥99.5%, Sigma-Aldrich and ammonium persulfate, APS reagent grade 98%, Sigma-Aldrich. Electrochemical tests were carried out in a model supercapacitor cell in which electrodes have been formed of the described composite, comminuted to the fraction <100 μm. The electrolyte was 1 M solution of H_2SO_4, and cellulose served as the separator. The measurements were made using a device ATLAS 0531 Electrochemical Unit & Impedance Analiser.

3. Results and discussion

3.1 Characterization of the PANI/MWCNT composite

The data on the composite structure and degree of MWCNT dispersion in aniline was obtained based on photographs made with electron scanning microscope VEGAII from TESCAN. Figure 1 shows a disordered, porous surface of the composite, with visible longitudinal structures of maximum length of 6 μm and the diameter >100 nm. These structures are single carbon nanotubes, some of which are not fully covered with a polymer. Spherical aggregates of various sizes, with diameters ranging from 0.5 μm to 2 μm are other visible elements of the composite. These are polyaniline particles which cover nanotubes to various degrees or appear in concentrations independent of MWCNT.

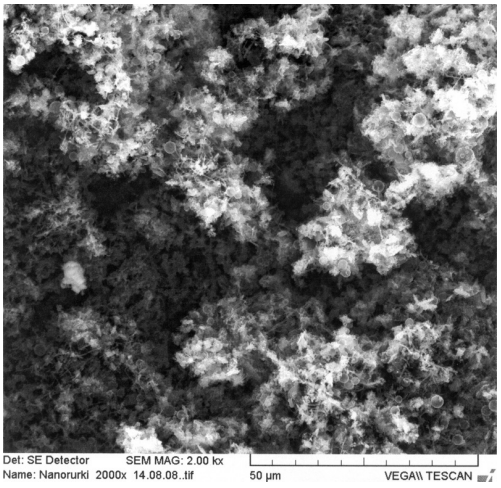

Fig. 1. SEM images of PANI/MWCNT composite (1:2000)

Thermoanalytical investigations provide information on mass alterations (TG) and energy variation during processes (DSC) taking place while heating up the sample. The results are particularly helpful for the improvement of the technology of fabrication of composites, showing a real proportion of components and degree of contami-

nation. They also provide practical data (for example thermoresistivity). The measurements were made with use of a thermoanalyzer DCS/TGA1 from the Mettler Toledo, with the air flow of 50 cm^3/min and the rate of increasing the temperature of 10 °C/min.

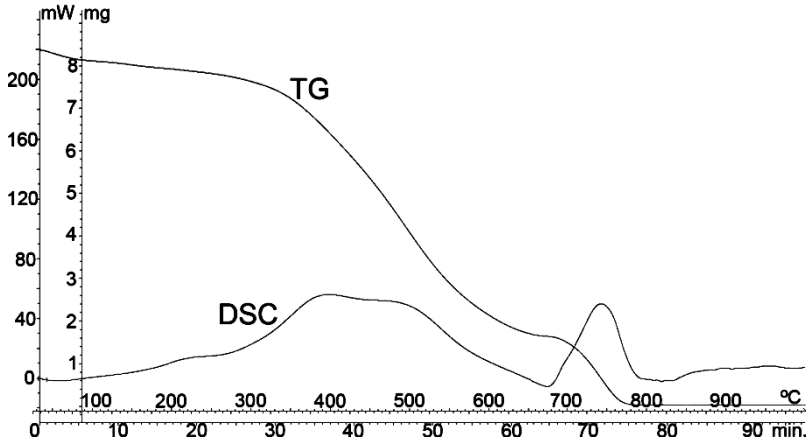

Fig. 2. Thermogram PANI/MWCNT

In the curve of mass diminution (TG) for the composite PANI –MWCNT (Fig. 2) two inflexions are visible. The first one at ca. 325 °C corresponds to decomposition of polyaniline, and the other one, narrower, above 700 °C, to decomposition of nanotubes. Temperature 325 °C is a limit of thermal stability of the composite (thermoresistivity). From the TG curve, the composition of the composite PANI:CNT = 0.7:0.2 was determined. Hence, the remaining 10% of the composite mass are contaminations removed during matrix degradation. The presence of PANI does not influence the resistivity of nanotubes, and neither brings about side effects. This is confirmed by the course of comparative curves for pure nanotubes. Based on those curves, it is possible to determine the purity of MWNTs (98%) as well as to learn that degradation occurs as a result of carbon oxidization to CO and CO_2, because almost 100% of the substance vanishes.

3.2. Capacitative properties of PANI/MWCNT

Cyclic voltammetry test was carried out at the rate of potential increase 1 mV/s to the value of 1.1 V. From the shape of the voltammetric curve (CV) it results that the capacity of a condenser is composed of the capacitance of a double electrical layer and the so called pseudocapacitance, related with the transfer of electric charge – expected for ECP. In experimental conditions, the Faraday process shows the largest exchange of charges for the cell potential 500 mV and is practically closed for the potential 600 mV (Fig. 3a).

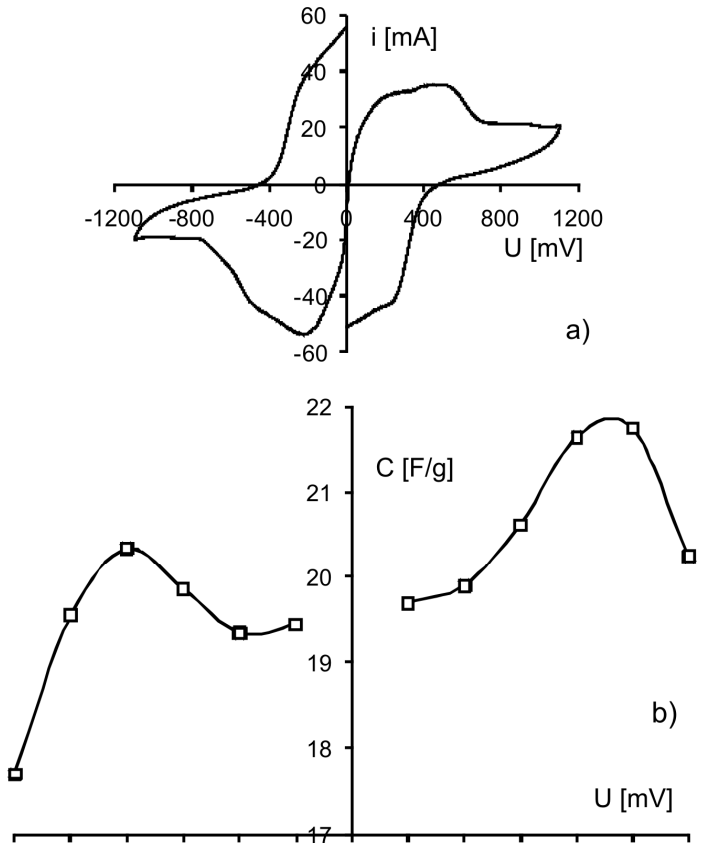

Fig. 3. Diagrams of: a) cyclic voltammetry, scan rate 1 mV/s, b) capacity in the function of electrode potential for the composite PANI/MWCNT in 1M H_2SO_4 electrolyte

This result is confirmed by galvanostatic measurements of the capacitor capacity. In Figure 3b, it can be seen that the capacitor reached its highest capacity when the potential difference was 500 mV. In the experimental conditions, the capacitance value during discharge was then 22 F/g in conversion to the mass of both electrodes. The measurements were taken for the constant value of current intensity for charging and discharging at the capacitor voltage amounting 100–600 mV. The assumed value in this investigation of the current intensity for charging and discharging was different for each voltage, and its value in amperes amounted 1/5 of the voltage value. The characteristics of the capacitor operation obtained in this way were used to calculate its capacitance (Fig. 3b) and to check the repeatability of its properties in sequential cycles (Fig. 4).

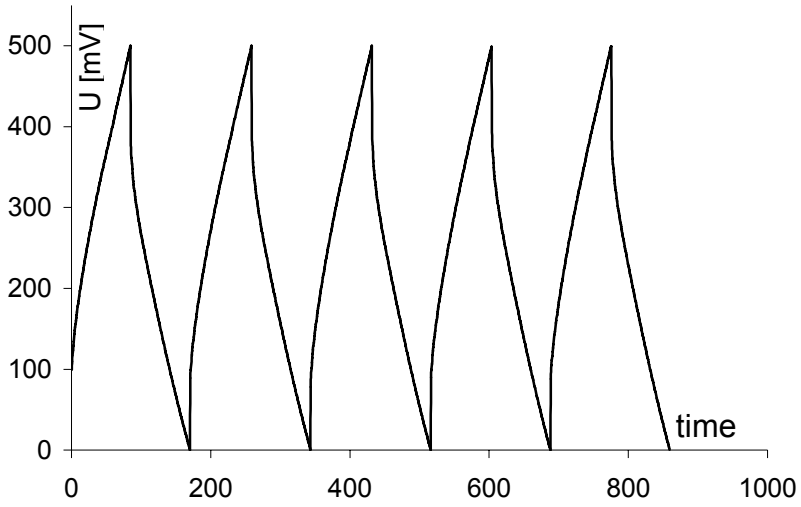

Fig. 4. Diagram of the galvanostatic measurements of the condenser charging and discharging for the composite PANI/MWCNT in 1 M H_2SO_4, i = 100 mA

Resistivity of pure PANI, pure MWCNT and PANI–MWCNT composite was measured with a Keithley electrometer 6517A and HP multimeter 34401A under similar conditions at room temperature. For PANI it equals 2.0×10^8 Ω·cm, for MWCNTs it is 0.9 Ω·cm, and for PANI/MWCNT composite – 5.0 Ω·cm.

4. Conclusions

Based on the TG/DSC measurements, it was concluded that the presence of nanotubes in the composite does not reduce the thermoresistivity of polyaniline. The polymerization of aniline in the presence of carbon nanotubes proceeds with the same efficiency as in the case of a pure monomer.

The degree of covering of nanotubes with polymere matrix, visible in SEM pictures, can be improved in the phase of synthesis of the composite by means of a stronger compatibilization of components. The structure imperfections negatively influence the properties of the composite as far as its supercapacitor applications are concerned by decreasing the participation of capacitance constituent which results from the separation of charges on the electrode/electrolyte boundary.

The capacitor capacitance amounted during the experiment ca. 20 F/g in conversion to the mass of both electrodes, what can be regarded as a very promising value for further investigations. Similarly promising are: stability of properties during consecutive cycles of charging and discharging and low resistivity.

It is shown, as expected, that addition of MWCNTs to PANI increases conductivity of the composite.

References

[1] CONWAY B.E., *Electrochemical Supercapacitors*, Kluwer Academic, New York, 1999.
[2] FRACKOWIAK E., BÉGUIN F., Carbon, 40 (2002), 1775.
[3] KOETZ R., CARLEN M., Electrochim. Acta, 45 (2000), 2483.
[4] SARANGAPANI S., TILAK B.V., CHEN C.P., J. Electrochem. Soc., 143 (1996), 3791.
[5] FENG W., BAI X.D., LIAN Y.Q., LIANG J., WANG X.G., YOSHINO K., Carbon, 41 (2003), 1551.
[6] FRACKOWIAK E., JUREWICZ K., DELPEUX S., BÉGUIN F., J. Power Sources, 97–98 (2001), 822.
[7] BÉGUIN F., SZOSTAK K., LILLO-RODENAS M., FRACKOWIAK E., *Carbon Nanotubes as Backbones for Composite Electrodes of Supercapacitors,* AIP Conf. Proc., 723 (2004), 460.
[8] RUDGE A., RAISTRICK I., GOTTESFELD S., FERRARIS J.P., Electrochim. Acta, 39 (1994), 273.
[9] MORGAN H., FOOT P.J.S., BROOKS N.W., J. Mater. Sci., 36 (2001), 5369.
[10] NISHIO K., FUJIMOTO M., YOSHINAGA N., J. Power Sources, 56 (1995), 189.
[11] AJAYAN P.M., STEPHAN O., COLLIEX C., TRAUTH D., Science, 265 (1994), 1212.
[12] SCHADLER L.S., GIANNARIS S.C., AJAYAN P.M., Appl. Phys. Lett., 73 (1998), 3842.
[13] WAGNER H.D., LOURIE O., FELDMAN Y., TENNE R., Appl. Phys. Lett., 72 (1998), 188.
[14] IIJIMA S., Nature, 354 (1991), 56.
[15] FAN S., CHAPLINE M.G., FRANKLIN N.R., TOMBLER T.W., Science, 283 (1999), 512.
[16] TANS S.J., VERSCHUEREN A.R.M., DEKKER C., Nature, 393 (1998), 49.
[17] WONG E.W., SHEEHAN P.E., LIEBER C.M., Science, 277 (1997), 1971.
[18] WOO H.S., CZERW R., WEBSTER S., CARROLL D.L., Synth. Met., 116 (2001), 369.
[19] KYMAKIS E., AMARATUNGA G.A., J. Appl. Phys. Lett., 80 (2002), 112.
[20] AGO H., PETRITSCH K., SHAFFER M.S.P., WINDLE A.H., FRIEND R.H., Adv. Mater., 11 (1999), 1281.
[21] YU Y., CHE B., SI Z., LI L., CHEN W., XUE G., Synth. Met., 150 (2005), 271.
[22] FRACKOWIAK E., KHOMENKO V., JUREWICZ K., LOTA K., BÉGUIN F., J. Power Sources, 153 (2006), 413.
[23] ZHOU Y., HE B., ZHOU W., HUANG J., LI X., WU B., LI H., Electrochim. Acta, 49 (2004), 257.
[24] CHENG Q., PAVLINEK V., HE Y., Eur. Polym. J., 43 (2007), 3780.
[25] RYABENKO G., FOKEEVA L.S., DOROFEEVA T.V., Russian Chem. Bull, Int. Ed., Vol. 53 (2004), 2695.
[26] BERNHOLC J., ROLAND C., YAKOBSKON B., *Nanotubes*, Science, 2 (1997), 706.
[27] RAMAMUTYHY P.C., MALSHE A.M., HARREL W.R., *Polyaniline / Single-walled Carbon Nanotube Composite Electronic Device,* Student paper.
[28] ZHANG X., ZHANG J., LIU Z., Carbon 43 (2005), 2186.

Received 15 June 2007
Revised 7 October 2009

Contents

GUIDELINES FOR AUTHORS

Manuscripts can be sent by conventional mail or by e-mail. Submission of a manuscript to *Materials Science-Poland* implies that it is not being considered for the publication elsewhere, and the authors have a necessary authorization to publish the material contained in the paper. **The manuscripts should conform to the formal standards of the Journal which may be found in the first issue of each volume and on the web page.**

Authors are encouraged to submit electronic versions of the manuscript by e-mail, to the address of the Journal. A single PDF file should be sent, containing text, references, figures, tables etc. Alternatively, the authors can submit the manuscript by conventional mail, sending a CD with the PDF file mentioned above, to the Editor-in-Chief at his address given below.

Each submitted manuscript will be reviewed, the final decision concerning its acceptance resting with the editors. Upon acceptance, the corresponding author will be requested to submit the following material (via e-mail or by conventional mail, on CD)

- A DOC or RTF file containing the final version of the text, references, tables and figure captions. The content of the file should be identical with that of the hard copy, and should exactly match the version seen and accepted be the referee(s).
- File(s) in appropriate formats containing figures. The required formats of the drawings (plots, schemes of technological processes) must be vector files such as XLS, OPJ, cdr (Excel, Origin, CorelDraw) which may also be exported as EPS, EMF or WMF files. Drawings submitted in tiff or jpg formats (bitmaps, raster graphics), even if exported as EPS, EMF or WMF files, will not be accepted. **Bitmaps are acceptable only in the case of photographs**. The photographs (only in grayscale) should have the resolution not lower than 300 dpi (estimated for the size in which they are expected to be reproduced).
- A PDF file containing the complete manuscript (text, literature, tables, figures, etc). The file should be carefully checked as it will serve as a hard copy in case of doubts. **The contents of the PDF file should exactly match the material in other files.**

Irrespective of whether the final version is submitted by e-mail or by conventional mail, the authors should also send **via conventional mail** a signed copy of the Copyright Transfer Agreement (available on the web page of the Journal).

For detailed information consult the first issue of each volume or the web page of the Journal.

The mail should be addressed to:

Professor Juliusz Sworakowski
Editor-in-Chief, Materials Science-Poland
Politechnika Wrocławska, W-3
Wybrzeże Wyspiańskiego 27
50-370 Wrocław, Poland

Electronic correspondence should be sent to: MatSci@pwr.wroc.pl
Web page of Materials Science-Poland: www.MaterialsScience.pwr.wroc.pl

The Publisher reserves the right to make necessary alterations to the text. Each corresponding author will be supplied with one free copy of the journal. Orders for additional offprints can be placed with the Publisher.